

NSF Career Award Program Final Report

Title: New Device Opportunities Enabled by Polar Dielectric and
Semiconductor Heteroepitaxy

Termination Date: 3/31/2009

William Alan Doolittle and Kyoung-Keun Lee

Georgia Institute of Technology
School of Electrical and Computer Engineering

SUMMARY

The objective of this research is to develop techniques that enable the use of lithium niobate (LN) or lithium tantalate (LT) as a new substrate for producing high-quality III-nitrides and implementing III-nitride-based optoelectronic devices. To achieve this goal, the material properties of LN will be studied in depth from the viewpoint of a new substrate for III-nitride epitaxial growth. It has been found that gallium nitride (GaN) epitaxial layers have a crystalline relationship with LN (LT) as follows: $(0001)\text{GaN} \parallel (0001)\text{LN (LT)}$ with $[10\text{-}10]\text{GaN} \parallel [11\text{-}20]\text{LN (LT)}$. The electrostatic properties at the interface between the LN (LT) substrates and the III-nitride materials dominated the electrical performance of HEMT structures and were controlled by a thin defect layer that can form during pre-growth furnace anneals or *in-situ* during anneals in vacuum. III-nitride growth on LN has been performed after high temperature (1000 °C) furnace anneals in a dry air environment, resulting in an atomically flat surface on LN (LT). However, while this furnace anneal improved surface smoothness and III-nitride film adhesion, it also caused the repolarization on the congruent LN (48.39 mole % of Li_2O) samples. However, the repolarization was not developed in the stoichiometric LN (49.9 mole % of Li_2O) samples during the identical thermal treatment. The surface stability of LN and LT substrates was monitored by *in-situ* spectroscopic ellipsometry in the vacuum chamber. The congruent LN showed a bigger variation of the pseudo-refractive index and pseudo-extinction coefficient during annealing at various temperatures in the range of 100 °C ~ 800 °C. The annealed congruent LN showed a Li-deficient lithium tri-niobate (LiNb_3O_8) phase, indicating surface modification at these temperatures. The stoichiometric LN showed little change in these indexes, implying better surface stability

than that of the congruent LN at elevated temperatures. On the other hand, LT showed only surface degassing in the same temperature range and better crystalline stability than that of LN at those temperatures, with no additional phase development. The structural quality of GaN epitaxial layers showed slight improvement when grown on LT substrates over LN substrates, confirmed by x-ray diffraction.

Conventional epitaxial growth technologies were adapted and modified to implement a successful AlGaIn/GaN heterostructure on LN (LT). The heterostructure were analyzed to verify the electrical and material properties using several characterization techniques: atomic force microscopy (AFM), Kelvin probe microscopy (KPM), spectroscopic ellipsometry (SE), Hall measurement, C-V measurement, x-ray diffraction, wet etching, and transmission electron microscopy (TEM). Furthermore, the grown heterostructure were fabricated into devices, and the devices were electrically characterized using several fabrication related facilities.

In conclusion, this report shows the properties of lithium niobate and lithium tantalate as a promising substrate for III-nitrides, addresses several problems of integrating compound semiconductor materials on LN and LT. It also suggests some solutions of the addressed problems, resulting in the successful growth of III-nitrides on ferroelectric materials. Finally, it demonstrates AlGaIn/GaN-based HEMT devices on ferroelectric materials that will allow the future development of the multifunctional electrical and optical applications.

CHAPTER 1: INTRODUCTION

The integration of III-nitride compound semiconductors and ferroelectric materials has been highlighted to implement multifunctional electrical, optical, and acoustic devices [1,2]. In particular, lithium niobate (LN) and lithium tantalate (LT) have been the most widely used ferroelectric materials selected for optoelectronic-acoustic-electronic applications, including nonlinear optics, optical modulators in fiber optical systems, and for various types of acoustic filters [1,2,3,4,5,6,7,8]. The integration of aluminum gallium nitride/gallium nitride (AlGaN/GaN) electronic drivers with the ferroelectric materials, LN and LT, provides the possibility of implementing compact optoelectronic-electronic chips, leading to increased cost savings and added functionality.

This work explores the material aspects of LN and LT as a promised substrate for III-nitrides, addresses several problems of integrating the compound semiconductor materials on LN and LT, suggests solutions to the problems, and shows a plan for further improvement of the integration. Finally, it demonstrates AlGaN/GaN heterostructure devices on ferroelectric materials. Chapter 2 introduces the basic material properties and historical review of III-nitride and ferroelectric materials. III-nitride materials are polar materials and have polarization directions: Ga-polar and N-polar, which affect the material properties. In this work, III-nitride materials were grown on the ferroelectric materials using plasma assist molecular beam epitaxy (MBE). Ferroelectric materials have spontaneous polarization and several material properties with different stoichiometry: congruent lithium niobate (CLN) and stoichiometric lithium niobate (SLN). Chapter 3 explains the fundamental device physics of high electron mobility

transistor (HEMT) devices. The HEMT devices are popular because of their high speed operation, which is possible because of existence of a two dimensional electron gases (2DEG) at the interface between AlGa_N and GaN layers. The 2DEG can be affected by several physical factors: polarization direction, the thickness and composition of AlGa_N layers, and interface smoothness. To make better epitaxial growth on foreign substrates, several aspects need to be pointed out: lattice mismatch between the films and substrates, electrostatic boundary condition, crystalline stability, practical difficulties, and surface chemistry. These aspects are discussed in following chapters. Chapter 4 investigates the lattice mismatch, electrostatic boundary condition, and crystalline stability. LN and LT have smaller lattice mismatches to GaN films than sapphire, with an expectation for lower dislocation density in the GaN films. Since LN and LT are polar materials, the electrostatic boundary condition at the substrate-film interface needs to be considered because the polarization direction of LN and LT can control the polarization direction of epitaxial films. Also, the crystalline stability of ferroelectric materials is critical to improve the crystal quality of GaN films. The crystalline stability is investigated using spectroscopic ellipsometry (SE) measurements with the substrate temperature varied under a vacuum condition. Chapter 5 addresses practical difficulties of III-nitrides growth on ferroelectric materials. There are substrate cracking problems and poor GaN film adhesion problems. The substrate cracking problem occurs during the cooling-down step because of huge differences in the thermal expansion coefficients of LN and LT compared to GaN. This problem is solved by developing a special designed mounting technique, which minimizes mechanical stress on samples. The poor adhesion of GaN films on ferroelectric materials is improved using a furnace anneal step. Surface

chemistry at the interface between GaN films and ferroelectric materials is investigated to improve the electrical properties of the GaN films as shown in Chapter 6. The surface chemistry is investigated by x-ray photoemission spectroscopy (XPS) and Auger electron spectroscopy (AES). X-ray diffraction (XRD) analysis also provides the relationship between dislocation density and GaN film conductivity. Chapter 7 presents the optimized method of growing III-nitrides on ferroelectric materials using plasma assist molecular beam epitaxy (PAMBE). AlN layers are used as buffer layers between GaN films and ferroelectric materials. The smoothness of AlN layers can be improved by a new shutter modulation technique, resulting in improved GaN crystal quality. However, the presence of a second phase, LiNb_3O_8 , after GaN growth, degrades the crystal quality of GaN films. *In-situ* reflected high-energy electron diffraction (RHEED) shows the phase variation and surface roughness of lithium niobate samples. Transmission electron microscopy (TEM) analysis shows the cross-sectional view of 18 nm thick intermixed-region between III-nitrides and LN substrates. The intermixed-region indicates the in- and out-diffusion of materials at the interface. The TEM images under two-beam condition show pure screw and mixed dislocations. After investigating the interfacial properties, HEMT structures are grown on CLN and SLN samples. As a result, HEMTs on SLN has two times higher mobility than that of HEMTs on CLN with less inversion domains on the surface observed by Kelvin probe force microscope (KPFM). The out-diffused impurities from the substrates make the GaN bulk layers conductive, providing a leakage current path for devices. Chapter 8 introduces several buffer schemes to minimize the out-diffusion: low temperature buffer layers, ZnO buffer layers, SiN_x and SiO_2 buffer layers, lithium-aluminum alloy buffer layers, MgO buffer layers, Y_2O_3 -stabilized ZrO_2 (YSZ) buffer,

and annealed AlN capping layers. The effects of these buffer schemes are investigated by Hall measurement for conductivity check, x-ray diffraction analysis for crystal quality, and atomic force microscope (AFM) for surface smoothness. Chapter 9 presents the fabrication procedure of HEMT devices on ferroelectric materials. After making alignment marks, MESA isolation is patterned to isolate each transistor in the same wafer. Then, source-drain definition and gate patterning are followed. The fabricated HEMT devices are characterized by capacitance-voltage and current-voltage analysis. The capacitance-voltage analysis gives a depth profile of the electron concentration in GaN films and confirms the existence of 2 DEG at the channel. The current-voltage analysis is performed using an Agilent network analyzer. Chapter 10 includes a final conclusion.

CHAPTER 2: BACKGROUND OF III-NITRIDE AND FERROELECTRIC MATERIALS

Even though the integration of III-nitrides on ferroelectric materials has been studied in the past decade, only a few publications are available because of the lack of material knowledge. My previous work has demonstrated, for the first time, LN (LT) as a promising material for multifunctional applications by implementing high-power AlGaN/GaN transistors epitaxially integrated on LN (LT) [3,4,5]. This section introduces the basic properties and various historical backgrounds of III-nitrides, ferroelectric materials (LN or LT), and the integration of the two materials. It is claimed that rf plasma assisted MBE (PAMBE) is suitable for III-nitride growths on LN and LT because of the capability of high-quality material growths at lower temperatures and the use of *in situ* analysis techniques. Finally, the effect of stoichiometry in the ferroelectric materials is discussed.

2.1 Basic properties of III-nitrides and heterostructure

III-nitrides, in particular, aluminum nitride (AlN), gallium nitride (GaN), and indium nitride (InN), have energy bandgaps of 6.2 eV, 3.4 eV, and 0.65 eV, respectively. AlN and GaN have a large conduction band offset, leading to the confinement of a high electron concentration at the interface of an AlGaN/GaN heterojunction [9]. During the growth of GaN layers normal to a (0001) basal plane, Ga and N atoms are arranged in bilayers with two closely spaced hexagonal layers, one with cations and the other with anions [10]. Thus, a basal GaN surface should be Ga-polar or N-polar, shown in Figure 1 [10].

The electrical properties of GaN-based heterostructures are suitable for high-power and high-voltage operation in microwave frequency applications. In general, the performance of power amplifiers made from field effect transistors (FETs) relies upon high breakdown fields. The electrical properties of GaN materials were summarized by Gelmont et al [11] using Monte-Carlo simulation. GaN possesses high breakdown fields of 3×10^6 V/cm, compared to Si and GaAs with 2×10^5 and 4×10^5 V/cm, respectively. GaN has a very high electron saturation velocity of 1.5×10^5 m/s and peak velocity of 2.7×10^5 m/s [11,12]. GaN-based HFETs have maximum drain current density approaching 2 A/mm [13]. The HFETs have very good small-signal performance with current-gain bandwidths on the order of up to $f_T \sim 110$ GHz [14]. And, the HFETs have a radio frequency (RF) power density of 6.3 W/mm at 10 GHz with power-added efficiency (PAE) of 38% for 1 mm gate-width devices [15].

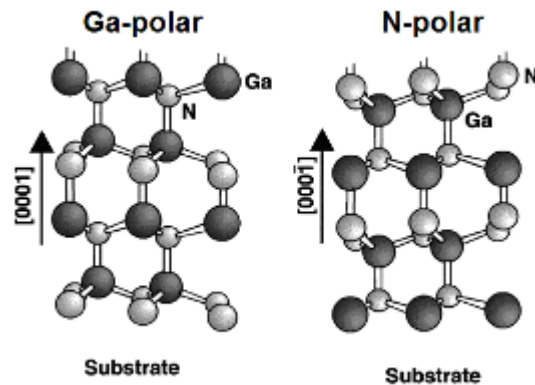


Figure 1: Wurtzite crystal structure: Ga-polar and N-polar of GaN [10].

2.2 Historical Review of Epitaxial III-nitrides Growth Techniques

Since the earliest investigations of III-nitrides (in particular, GaN, AlN, and InN) in 1932 [16], many growth techniques have been developed to improve the quality of III-nitrides [17]. One of the more popular earlier III-nitride growth techniques was reactive sputtering, which produced polycrystalline or even amorphous crystal structures [17]. Among the growth techniques, a chemical vapor deposition (CVD) method has produced the first single-crystal GaN thin films with flowing HCl vapor over metallic Ga, which reacted downstream at a substrate with NH₃, resulting in very high background n-type carrier concentration [18]. This technique has been extended to grow high-quality AlN layers [19]. The high background electron concentration in GaN and AlN has commonly been attributed to nitrogen vacancies. Reactive molecular-beam epitaxy (RMBE) might increase the incorporation of nitrogen species to reduce the background electron concentration and grow abrupt nitride heterojunctions [17]. However, this approach has shown a limitation of producing high-quality materials below the substrate temperature of 600°C because of a low reaction rate of ammonia at low temperatures, resulting in a high background carrier concentration [20]. The growth temperature limitation has been overcome using the plasma excitation of nitrogen with MBE, resulting in increasing the reactivity of nitrogen and having very good quality materials [21]. In contrast to MBE, the use of plasma excitation for efficient CVD growth has not yet been proven, which has usually used metal-organic gases and NH₃ to grow high quality III-nitrides at the substrate temperatures of near 1000-1100°C [17].

MBE is well suited to heterostructure growths because of its operational condition at relatively low temperatures. In MBE, group III elements (Ga, Al, or In) and dopants

(Si or Mg) are heated in Knudsen cells, and their atomic or molecular beams are directly condensed onto a heated substrate where they react with nitrogen molecules [22]. The nitrogen molecule sources are available from cracking ammonia gas at high temperatures, cracking nitrogen gas directly using ECR plasma or rf plasma at relatively lower temperatures [20]. Unlike CVD growth, which proceeds at conditions nearer thermodynamic equilibrium of the crystallizing phase, MBE growth is carried out under conditions far from thermodynamic equilibrium and is governed mainly by the kinetics of surface processes occurring when impinging beams react with the outermost atomic layers of substrate crystals [23]. Another benefit of using MBE is the utilization of a wide range of surface analysis techniques, such as reflection high energy electron diffraction (RHEED), mass spectrometry for gas analysis, and Auger electron spectroscopy (AES). Therefore, this research claims that rf plasma assisted MBE (PAMBE) is suitable for III-nitride growths on LN and LT because of the capability of high-quality material growths at lower temperatures and the use of *in situ* analysis techniques.

2.3 Historical Review of ferroelectric materials

Since the first polycrystalline lithium niobate (LN) or lithium tantalate (LT) was grown from a melt solution in 1949 [24], many studies have been conducted to achieve a perfect single-crystal LN (LT), which has been a promising material for quantum electronics [25]. The crystallographic structure of LN and LT crystals is in space group $R3c$ at low temperatures (below the Curie temperature), while the structure of LN changes into space group $R\bar{3}c$ above the Curie temperature [26]. High-quality single-crystal LN (LT) has been grown by the Czochralski growth method in an air environment

in induction furnaces [27,28]. More recently, high-quality single-crystal LN and LT samples, which have a maximum dimension of 6 inches, have been commercially available from Crystal Technology, Inc. and Red Optronics, respectively. [29,30].

2.4 Stoichiometry of lithium niobate and lithium tantalate

LN and LT have spontaneous polarization, P_s , the orientation of which can be prescribed in ferroelectric materials. For LN (LT), the spontaneous polarization, P_s , is 0.71 C/m^2 (0.55 C/m^2), resulting from the placement of cations of Li^+ and Nb^{5+} (Ta^{5+}) in LN (LT) structure [31,32,33], as shown in Figure 2. A LN (LT) structure has the stacking sequence of Li-Vacancy-Nb (Ta)-Li at room temperature. By electrically driving the Li^+ ion through the oxygen plane into the vacancy occupied octahedra, the spontaneous polarization of LN (LT) can be changed.

LN has a wide solid solution range, from around stoichiometric composition to lithium-lean composition as low as about 45 mol% of lithium oxide (Li_2O), as shown in Figure 3 [34,35]. Almost all commercially produced LN samples have been grown by the Czochralski technique and have 48.4 mol% of Li_2O composition at the congruent melting point of 1250°C [35], which is referred to as congruent lithium niobate (CLN). The commercial LN samples have had difficulty achieving specified off-congruent composition by the Czochralski method because of segregation effects [36]. However, this difficulty has been overcome using a vapor transport equilibration (VTE) method, which anneals LN samples in the powder mixture of Li_2CO_3 and Nb_2O_5 at 1100°C for 60 ~ 400 hours [36]. The VTE technique provides near-stoichiometric composition (50mol% of Li_2O) of LN, which is called stoichiometric lithium niobate (SLN). The composition is monitored by measuring the Curie temperature changes from 1080°C to 1180°C [37].

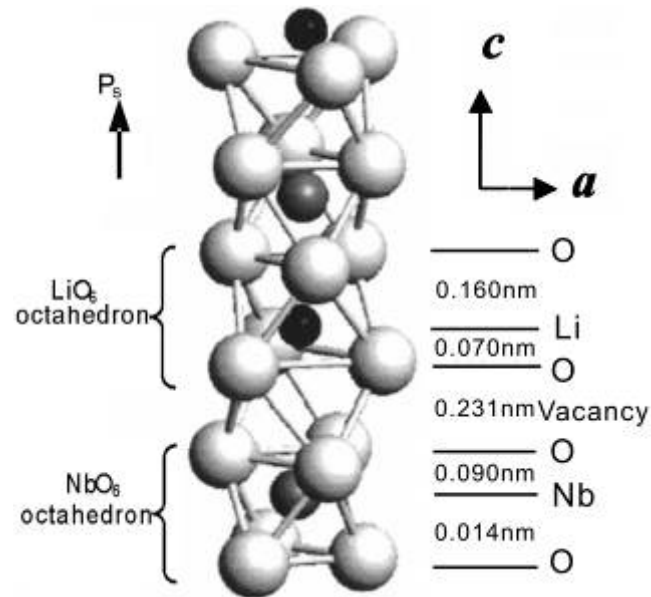


Figure 2: Structure of lithium niobate: Oxygen triangular planes with Li, Nb, and vacancy site along *c*-axis with LiO₆ and NbO₆ octahedron structure and the indication of polarization orientation and bond lengths. Light gray balls: oxygen, dark gray balls: niobium, and black balls: lithium [31,45].

Although lithium tantalate (LT) is iso-structural to LN, it has a higher melting point of 1650 °C [35] and a lower ferroelectric Curie temperature, T_c , sensitively depends on lithium composition. Earlier reported T_c values of LT are in the 600 ~ 660 °C range [38], 660 ± 10 °C [39], 618 °C [40], and so on. LT has the phase relations of Li₂O-Ta₂O₅ system, analyzed by measuring the Curie temperature, as shown in Figure 4 [41]. Normally, LT is grown from starting mixture materials of Li₂CO₃ and Ta₂O₅ at 1250 °C for 5 hours, resulting in various compositions from Ta₂O₅/(Li₂O + Ta₂O₅) = 49.0 to 54.25 mol%. Congruent LT has 52.23 mol% of Ta₂O₅ (or 47.77 mol% of Li₂O) at the congruent melting temperature [41], 49.0 mol% [42], or 47.70 mol% of Li₂O, produced by a vapor transport equilibration (VTE) method [43].

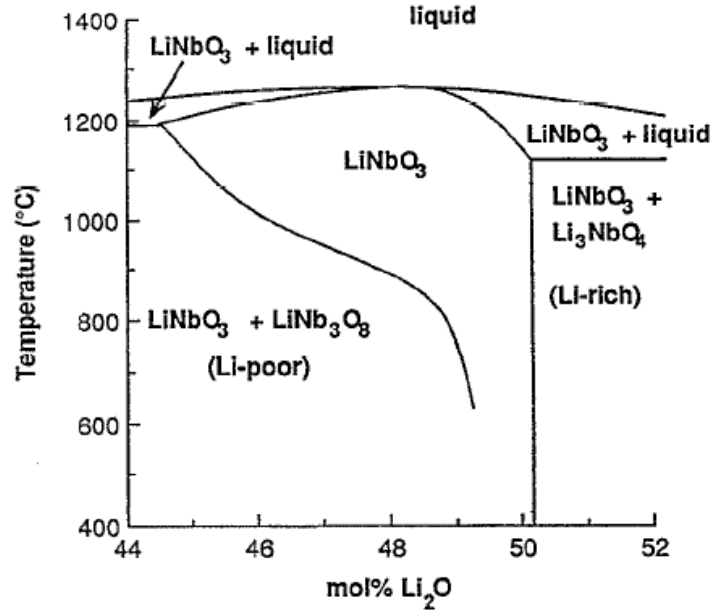


Figure 3: Approximate phase diagram for lithium niobate [36].

The stoichiometry of LN and LT affects several crystal properties. The Curie temperature of congruent LN (LT) is lower than that of stoichiometric LN (LT), which is affected by Nb^{5+} (Ta^{5+}) cations movement along the $+c$ direction. The Curie temperature may be expressed in terms of displacement Δz of certain atoms by $T_c = (2.00 \pm 0.09) \times 10^4 (\Delta z)^2$ °K [44]. The cation–anion distances (i.e., bond lengths) in congruent LN (LT) are shorter than in stoichiometric LN (LT). The distances are varied with Li^+ movement along the c direction by temperature variation [45]. The coercive field of congruent LN (LT) is higher than of stoichiometric LN (LT) [83], which is explained in the next section.

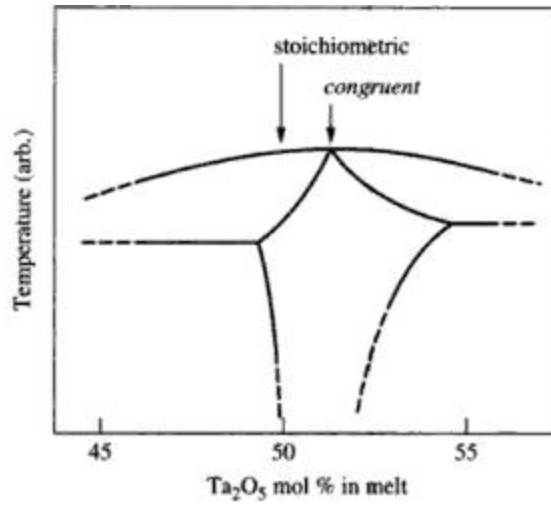


Figure 4: A tentative phase relation in $\text{Li}_2\text{O}-\text{Ta}_2\text{O}_5$ system in the vicinity of LiTaO_3 [41].

CHAPTER 3: FUNDAMENTAL HEMT DEVICE PHYSICS

The characterization of high electron mobility transistor (HEMT) devices is determined by the electrical properties of bulk materials, heterostructural behaviors, and the physical nature of metal contacts to the materials. This section addresses the fundamental device physics and operation of GaN-based HEMT devices, which have high-voltage, high-power, and high-speed properties.

3.1 Basic Material properties of GaN-based devices

Golio [46] described that, in semiconductor materials, the electrical current is dominated by the rate of flow of electrical charge. When an electric field is applied to the materials, the electrons are accelerated in the opposite direction of the field. The carriers continue to move until they suffer from collision, called scattering, with ionized doping impurity or defects in the materials [46]. The drift current density (neglecting diffusion current - added later) can be expressed [46] as

$$J_{\text{drift}} = qnv$$

where q is the electronic charge, n is the density of free electrons in the conduction band, and v is the average velocity of the carriers in the materials. The average velocity of the carriers is proportional to the applied electric field strength as

$$v = \mu E$$

where E is the electric field strength and μ is the low-field electron mobility [46]. Mobility is a measure of how fast a charge moves within the semiconductor structure and is affected by doping density in a low electric field. According to the study of Chin et al [47], the low-field mobility of GaN is calculated as a function of carrier concentration at 300K with compensation ratio, N_A/N_D as shown in Figure 5 [47]. The mobility does not degrade in the case of extremely low doping density levels, but does degrade rapidly when the doping density is increased [47].

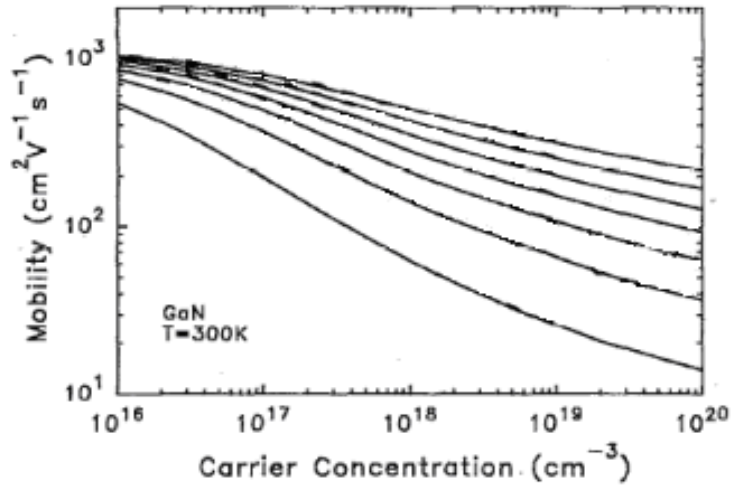


Figure 5: Mobility of GaN calculated as a function of carrier concentration with compensation ratios of 0.00, 0.15, 0.30, 0.45, 0.60, 0.75, and 0.90 at 300K [47].

Ko et al [48] showed the relationship between the mobility and carrier concentration as a function of film thickness based on experimental data as shown in Figure 6. In the experiment, all of the GaN films were grown on a sapphire substrate by a lower pressure organometallic vapor phase epitaxy (OMVPE) system. The data shows that the mobility increases rapidly and the carrier concentration decreases as the film

thickness increases. This result indicates that the GaN crystal quality is poor at the initial layer of growth and significantly improved for thick GaN layers [48].

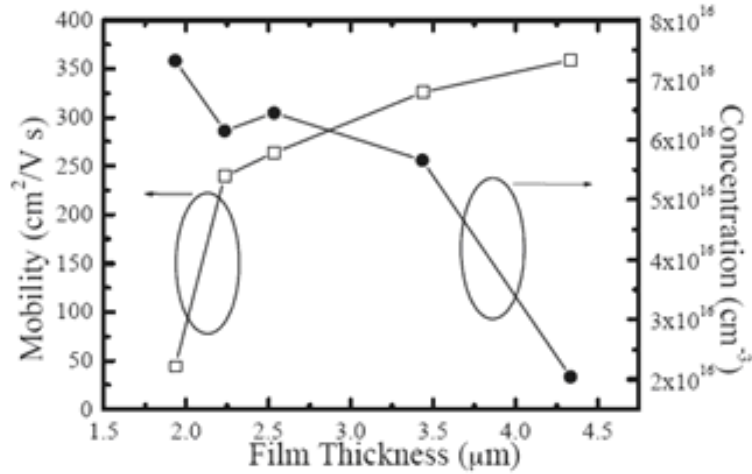


Figure 6: Dependence of the mobility and carrier concentration on the GaN epitaxial layer thickness measured [48].

Kolnik et al [49] showed that the electron velocity becomes limited and saturates when a high electric field is applied. The dependence between the velocity and electric field is calculated along the (100) direction of wurtzite GaN films as shown in Figure 7 [49]. The calculation assumes that free electron and ionized impurity concentration are in the range of 10^{17}cm^{-3} . Note that the maximum steady-state velocity is approximately $2.5 \times 10^7 \text{ cm/s}$, and a region of negative differential resistance is observed. The negative differential resistance region gives the basic principle of the Gunn diode effect, which occurs in direct bandgap materials with more than one valley in the conduction band [49].

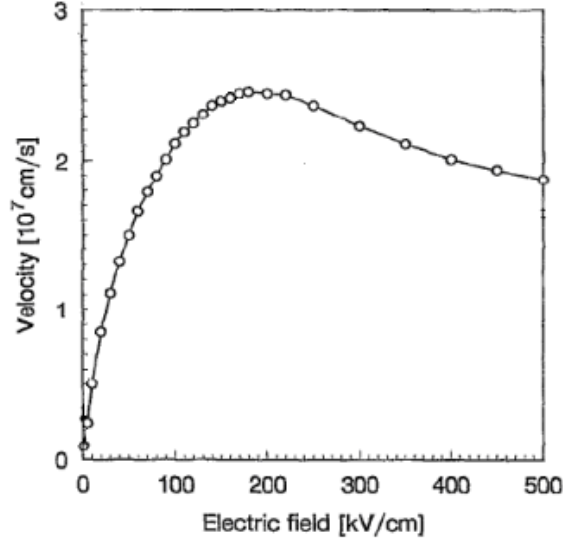


Figure 7: Ensemble Monte Carlo calculation of steady state electron drift velocity in GaN films as a function of electric field [49].

According to the summary of Golio [46], the current could be generated by not only the applied electric field, but also carrier density gradients. The current density generated by the carrier density gradients, diffusion current density, in electron dominated materials can be written as [46]

$$J_{diff} = qD_n \nabla n$$

where D_n is the electron diffusion coefficient, which is related to the mobility and thermal energy in non-degenerate semiconductors: $D_n = (kT/q)\mu_n$. Therefore, the total electron current density is expressed by [46]

$$J_n = q\mu_n n + qD_n \nabla n$$

In the AlGaN/GaN HEMT heterostructure, the electron mobility is dramatically improved because of the existence of a two-dimensional electron gas (2DEG) at the

heterojunction. According to the study of Gaska et al [50], the electron Hall mobility and sheet concentration of the HEMT structure on 6H-SiC are measured as the function of temperatures as shown in Figure 8. The Hall measurements using the Van der Pauw contact setup gave the electron sheet concentrations and mobilities $n_s = 1.3 \times 10^{13} \text{ cm}^{-2}$, $\mu = 2019 \text{ cm}^2/\text{Vs}$, and $n_s = 10^{13} \text{ cm}^{-2}$, $\mu = 8583 \text{ cm}^2/\text{V s}$ at $T = 300 \text{ K}$ and $T = 77 \text{ K}$, respectively [50]. The electron sheet concentration decreases by about 25% as the sample temperature decreases and remains approximately constant at lower temperatures. The Hall mobility also increases as the temperature decreases until about 10K. The Hall mobility becomes steady with $\mu_H = 10250 \pm 100 \text{ cm}^2/\text{V s}$ at lower temperatures [50].

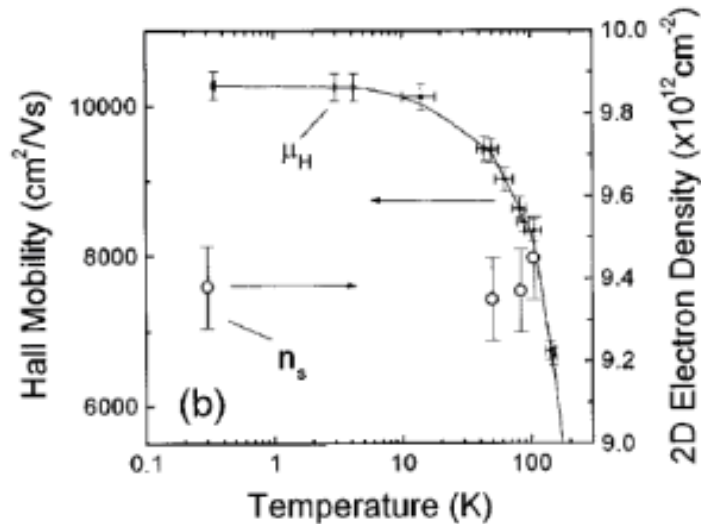


Figure 8: Electron Hall mobility and sheet concentration as the function of temperatures measured with magnetic field intensity $H = 1 \text{ Tesla}$ [50].

3.2 Contact properties

According to the summary of Golio [46], the semiconductor metal contact plays a very critical role in connecting semiconductors and other electrical components. The

choice of contact material provides two types of contact properties: rectifying and ohmic contact. The metal contact becomes the rectifying contact when there is a large mismatch between the Fermi energy of the metal contact and semiconductors. A reduced fermi-energy mismatch to a heavily doped semiconductor leads to an ohmic contact. Most metal-semiconductor contacts are annealed or alloyed after the initial deposition of metals to reduce the contact resistance [46].

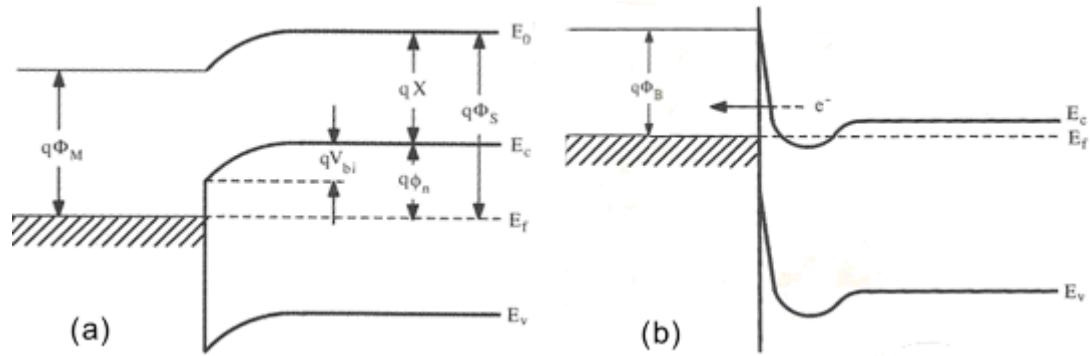


Figure 9: Band diagram for (a) an idealized ohmic contact in n-type semiconductor, (b) Ohmic contact band diagram illustrating the tunneling process [46].

Theoretically, the ohmic contact is formed when an n-type semiconductor with a work function ϕ_S is connected to metal layers with a smaller work function ϕ_M , i.e., $\phi_S > \phi_M$. as shown in Figure 9 (a) [46]. In the case of a p-type semiconductor, the ohmic contact is formed when the work function of the metal must be close to or smaller than the electron affinity of the semiconductor. The Fermi levels are aligned by the electron transfer from the metal to the semiconductor. Therefore, the barrier-to-electron flow is minimized by allowing electrons to flow across the barrier with minimal resistance. Thus,

the ohmic contact can be described as a contact with voltage-independent resistance in a metal and semiconductor junction [46]. A more practical contact is a tunneling contact. If there is sufficiently heavy doping at the semiconductor region with thickness on the order of tens of angstroms adjacent to the metal contact, then electrons can tunnel through the barrier rather than having to surmount it [46]. This process is shown in Figure 9 (b). In HEMT devices, the source and drain contacts are ohmic contacts and are combined with parasitic resistances, which are modeled as a contact ohmic loss and the losses in the semiconductor [46].

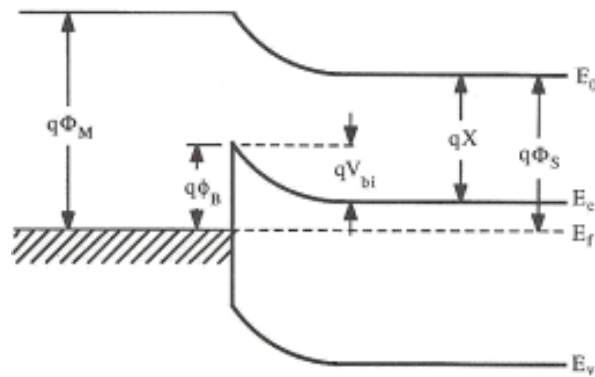


Figure 10: Ideal metal-semiconductor (n-type) band diagram [46].

While the ohmic contacts need to have minimal resistance, the rectifying contacts, Schottky barriers, in the solid-state HEMT devices are required to have various functions (e.g., rectification, amplification, etc) [46]. The band diagram of the Schottky barriers is shown in Figure 10 [46]. In this case, the work function of an n-type semiconductor is lower than the metal work function, $\phi_S < \phi_M$. The work function difference makes the electron flow from the semiconductor to the metal surface. If the metal is biased positively relative to the semiconductor, the barrier ϕ_B is lower and electrons move to the

metal exponentially with increasing bias. With reverse bias, the barrier is higher and the electron movement is decreased by the same exponential factor [46].

3.3 High electron mobility transistor devices

A high electron mobility transistor (HEMT) is a heterostructure field-effect device. It has several different names including modulation-doped field effect transistor (MODFET), two-dimensional electron gas field-effect transistor (TEGFET), selectively doped heterostructure transistor (SDHT), and heterojunction field-effect transistor (HFET) [51].

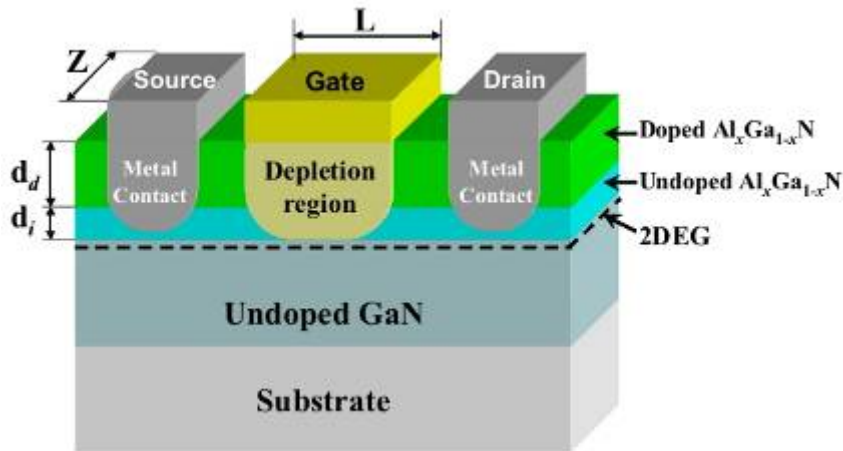


Figure 11: Schematic view of modulated doped GaN based HEMTs structure [52].

According to the summary of Golio [46], in GaN-based HEMTs, the carriers in doped AlGaIn materials diffuse to the undoped narrower bandgap materials, GaN, where they combine with polarization discontinuity induced carriers to form the channel. The carriers collected in the undoped heterointerface are spatially separated from the doped

region and have extremely high mobility because there is no impurity scattering in bulk layers [46]. Figure 11 shows a schematic of a modulated doped GaN-based HEMT structure, in which AlGa_N layers are doped except for an undoped narrow region, d_i [52]. Carriers in AlGa_N layers will diffuse to the undoped GaN and are collected at the conduction channel as two-dimensional electron gases (2DEG) [52]. Since III-nitrides are polar materials, GaN-based HEMTs have induced polarization, which significantly increases the sheet concentration at the heterointerface. The induced polarization consists of two different polarizations: spontaneous and piezoelectric polarization [10]. According to the study of Ambacher [9], the spontaneous polarization leads the electric field of up to 3MV/cm and the piezoelectric polarization caused by strains at the heterointerface makes an electric field of 2MV/cm. These induced high electric fields produce high sheet charge density and form a quantum well structure, which leads the spatial separation of the hole and electron wave functions [10].

Smorchkova et al [53] summarized that the total polarization \mathbf{P} of the AlGa_N/GaN heterojunction is the sum of the spontaneous polarization \mathbf{P}_{SP} and piezoelectric polarization \mathbf{P}_{PZ} without any external electric field. \mathbf{P}_{SP} is opposite the growth direction and increases in magnitude by the increase of Al composition in AlGa_N [53]:

$$\mathbf{P}_{SP}(x) = (-0.052x - 0.029) \text{ C/m}^2$$

where x is the Al mole fraction in the Al _{x} Ga _{$1-x$} N alloy. The piezoelectric polarization is related to the strain from the lattice constant difference (2.4% of lattice mismatch) between GaN and AlGa_N layers [53]:

$$\mathbf{P}_{\text{PZ}}(x) = 2 \frac{a(x) - a(0)}{a(0)} \left[e_{31}(x) - e_{33}(x) \frac{C_{13}(x)}{C_{33}(x)} \right]$$

where $a(x)$ and $a(0)$ are the lattice constants of $\text{Al}_x\text{Ga}_{1-x}\text{N}$ and GaN , respectively, e_{31} and e_{33} are piezoelectric constants, and C_{13} and C_{33} are elastic constants. Therefore, the polarization-induced charge density at the interface between AlGaN and GaN is described as [53]

$$\sigma(x) = \mathbf{P}(\text{Al}_x\text{Ga}_{1-x}\text{N}) - \mathbf{P}(\text{GaN}) = \mathbf{P}_{\text{SP}}(\text{Al}_x\text{Ga}_{1-x}\text{N}) + \mathbf{P}_{\text{PZ}}(\text{Al}_x\text{Ga}_{1-x}\text{N}) - \mathbf{P}_{\text{SP}}(\text{GaN})$$

According to the survey of Rashmi [52], the 2DEG sheet carrier concentration (n_s) is the most important parameter for governing the performance of AlGaN/GaN HEMTs. To make a model for the 2DEG sheet carrier concentration, it is necessary to assume that the 2DEG lies in an asymmetric triangular potential well with only the first two quantum states (ground state: E_0 and first excited state E_1) occupied as shown in Figure 12. Then the total charge accumulated in the quantum well is derived by solving the Schrodinger and Poisson equations as follows [52]:

$$n_s = D k_B T \ln \left(\left(1 + \exp \left(\frac{E_F - E_0}{k_B T} \right) \right) \times \left(1 + \exp \left(\frac{E_F - E_1}{k_B T} \right) \right) \right)$$

where $D = 4\pi m^*/h^2$ is the conduction band density of states of a 2D system, k_B is the Boltzmann's constant, m^* is the electron effective mass ($m^* = 0.22m_e$), m_e is the electron rest mass, h is the Planck's constant, T is the temperature, E_F is the Fermi energy, and the

allowed energy levels in the well are $E_i = \gamma_i n_s^{2/3}$ (eV) for $i=0, 1$ with $\gamma_0 = 2.123 \times 10^{-12}$ and $\gamma_1 = 3.734 \times 10^{-12}$ [52].

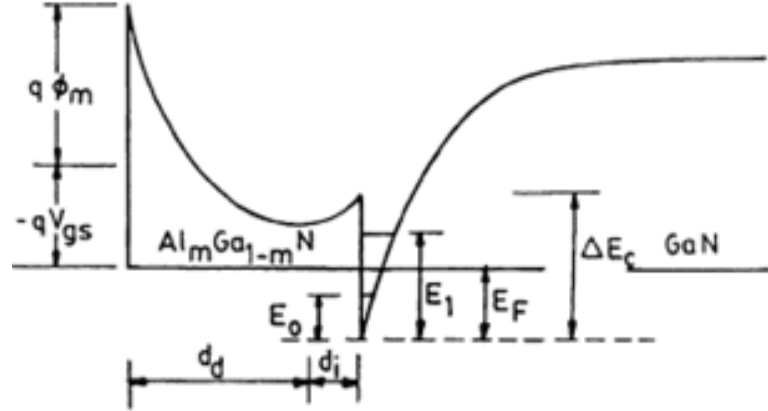


Figure 12: Energy band profile of heterojunction of AlGaIn and GaN [52]

The gate depletion and junction depletion regions overlap under the total depletion approximation. Then the total charge in the depleted region of the AlGaIn layer is calculated by solving the Poisson's equation given as [52]

$$n_s(x) = \frac{\varepsilon(x)}{q(d_d + d_i)} \left(V_{gs} - V_{th}(x) - \frac{E_F}{q} \right)$$

where $\varepsilon(x)$ is the dielectric constant of $\text{Al}_x\text{Ga}_{1-x}\text{N}$, d_d is the doped AlGaIn layer thickness, d_i is the undoped AlGaIn spacer layer thickness, V_{gs} is the applied gate bias, and $V_{th}(x)$ is the polarization-dependent threshold voltage. The polarization-dependent threshold voltage is obtained as [52]

$$V_{th}(x) = \phi_m(x) - \Delta E_c(x) - \frac{qN_D d_d^2}{2\varepsilon(x)} - \frac{\sigma(x)}{\varepsilon(x)} (d_d + d_i)$$

where $\phi_m(x)$ is the Schottky barrier height, $\Delta E_c(x)$ is the conduction band discontinuity between AlGaIn and GaN layers, and N_D is the doping density of the doped AlGaIn layer. Also, the drain current in the 2DEG channel can be derived from the current density equation as [52]

$$I_{ds} = Zq\mu(y) \left(n_s(y) \frac{dV_c(y)}{dy} + \frac{k_B T}{q} \frac{dn_s(y)}{dy} \right)$$

where Z is the gate width, $V_c(y)$ is the channel potential at position y , and $\mu(y)$ is the field dependent mobility as [52]

$$\mu(y) = \frac{\mu_0}{\left(1 + \frac{1}{E_1} \frac{dV_c(y)}{dy} \right)}$$

where $E_1 = E_c v_{sat} / (\mu_0 E_c - v_{sat})$, E_c is the saturation electric field, μ_0 is the low-field mobility, and v_{sat} is the saturation drift velocity. Therefore, the drain current is obtained using the mobility equation in the previous drain current equation as [52]

$$I_{ds} = \frac{Zq\mu_0}{\left(1 + \frac{1}{E_1} \frac{dV_c(y)}{dy} \right)} \left(n_s(y) \frac{dV_c(y)}{dy} + \frac{k_B T}{q} \frac{dn_s(y)}{dy} \right)$$

where the $V_c(y)$ has boundary conditions with channel length L ,

$$V_c(y)|_{y=0} = I_{ds} R_s$$

$$V_c(y)|_{y=L} = V_{ds} - I_{ds} (R_s + R_d)$$

where $R_s(R_d)$ is the parasitic source (drain) resistance and V_{ds} is the applied drain voltage.

Transconductance g_m and output resistance g_{ds} are obtained by [54]

$$g_m = \left. \frac{dI_{ds}}{dV_{gs}} \right|_{V_{ds}=const.}$$

Output conductance and resistance have the following relation, which is a slope of the I-V curve, as shown in Figure 13 [54].

$$g_{ds} = \frac{1}{r_{ds}} = \left. \frac{dI_{ds}}{dV_{ds}} \right|_{V_{gs}=const.}$$

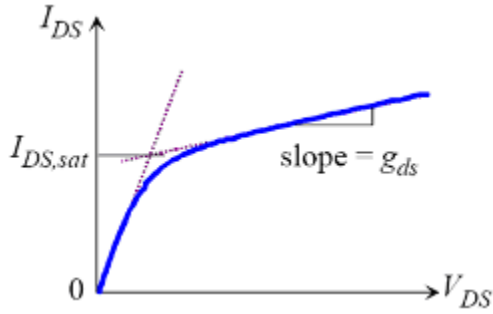


Figure 13: Derived output conductance g_{ds} from I-V curve in GaN HEMT devices [54].

For microwave applications, the unity gain cut-off frequency f_T is given by the transconductance and device capacitances as [55]

$$f_T = \frac{g_m}{2\pi(\text{total capacitance})} = \frac{Zv_s C_i}{2\pi(ZLC_i + C_p)} = \frac{v_s}{2\pi(L + C_p / ZC_i)}$$

where $C_i = \epsilon(x)/q(d_d+d_i)$ and C_p are the parasitic capacitances. The cut-off frequency could be improved if semiconductors have large v_s , a gate structure with an ultra-short gate length, and a device configuration with minimum parasitic capacitances [55].

3.4 Two dimensional electron gases (2DEG) in heterostructure

It is useful to understand the unique properties of GaN-based heterostructures by comparing them with GaAs-based heterostructures, which are conventional III-V materials. Modulated doped AlGaAs layers in AlGaAs/GaAs heterostructures induce electron carriers in undoped channel regions. The corresponding electrons are accumulated into an interface potential well, resulting in two-dimensional electron gases (2DEG) [10]. The mobility of these electrons is higher than electrons in active bulk layers because the electrons in 2DEG are spatially separated from dopants in AlGaAs barrier layers [56].

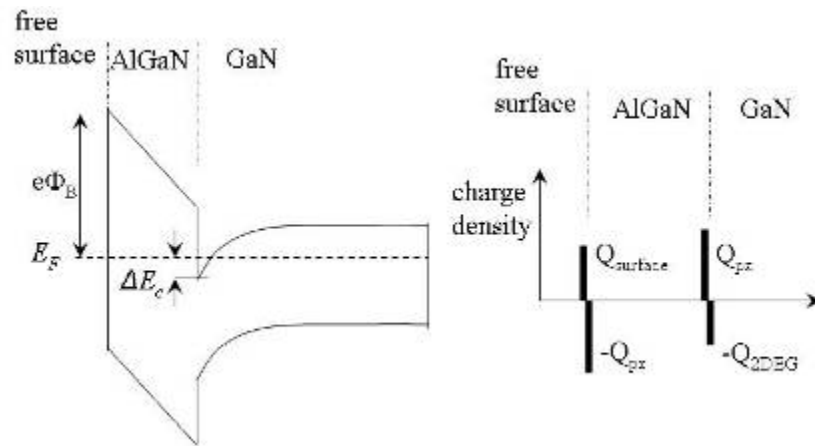


Figure 14: Band diagram and schematic charge density of AlGaN/GaN heterostructures, where $e\Phi_B$ is Schottky barrier height [58].

For AlGa_N/Ga_N heterostructures, the modulated doping is not required in order to have a 2DEG because of the donor-like surface states from the surface of AlGa_N/Ga_N layers induced by polarization, which acts as a primary source of electrons in the channel of heterostructures [57]. The outstanding performance of Ga_N-based FETs comes from 2DEG with a sheet carrier concentrations of 10¹³ cm⁻² or higher without any intentional doping, which is achievable only by the intentional doping in the conventional III-V materials [10]. Therefore, it is necessary to understand the 2DEG in AlGa_N/Ga_N heterostructures to improve device performance.

According to the study of Asbeck et al [58], the formation of 2DEG is mainly dependent on the height of conduction-band discontinuity (ΔE_c) at the interface between the AlGa_N barrier layers and the Ga_N bulk layers, shown in Figure 14 [58]. The conduction-band discontinuity has a polynomial relationship with the mole fraction of Al in AlGa_N barrier layers as shown by following equations [59].

$$\Delta E_c(\text{Al}_{1-x}\text{Ga}_x\text{N}/\text{GaN}) = \begin{cases} 1.341x^2 - 0.789x + 0.794 & x < 0.43 \\ 2.756x^2 - 5.198x + 2.442 & x > 0.43 \end{cases}$$

As mentioned earlier, the 2DEG is critically affected by polarization at a heterointerface, which acts as a primary source of electrons in the channel of heterostructures [57]. The polarization, \mathbf{P} , in AlGa_N/Ga_N heterostructures consists of spontaneous polarization, \mathbf{P}_{SP} , and strain-induced, piezoelectric polarization, \mathbf{P}_{PZ} . Polarization at zero strain refers to spontaneous polarization, which is increased by the increase of crystal non-ideality, such as the displacement or disordering of constituent atoms in crystals [60]. The piezoelectric polarization presents in strained layers of III-

nitrides grown along the (0001) orientation with wurtzite crystal structures aligned along the [0001] direction, is given by

$$\mathbf{P}_{\text{PZ}}(x) = 2d_{31}(C_{11} + C_{12} - 2C_{13}^2/C_{33})\varepsilon_{xx}$$

where d_{31} is a relevant piezoelectric constant (i.e., AlN: -2×10^{-10} cm/V [61]), C_{ij} are elastic constants, and $\varepsilon_{xx} = a_{\text{GaN}}/a_{\text{AlGaN}} - 1$, where a_{GaN} and a_{AlGaN} are the lattice constants of GaN and $\text{Al}_x\text{Ga}_{1-x}\text{N}$, respectively [62]. The difference in polarization across AlGaN/GaN heterostructures makes an interface charge dictated by electrostatic boundary conditions imposed by Gauss' Law. The polarization-induced interface charge density $\rho_p = -\nabla \cdot (\varepsilon \mathbf{E} + \mathbf{P})$, where $\mathbf{P} = \Delta \mathbf{P}_{\text{PZ}} + \Delta \mathbf{P}_{\text{SP}}$. $\Delta \mathbf{P}_{\text{PZ}}$ and $\Delta \mathbf{P}_{\text{SP}}$ are the differences of spontaneous and piezoelectric polarization at the heterointerface, respectively. The interface charge concentration in 2DEG can be described by the following electrostatic analysis [63]:

$$\begin{aligned} n_s &= \sigma_{pz} / e - (\varepsilon_{\text{AlGaN}} / de^2)(e\phi_b + E_F - \Delta E_c) \\ \sigma_{pz} / e &= 2d_{31}(C_{11} + C_{12} - 2C_{13}^2/C_{33})(a_{\text{GaN}} / a_{\text{AlN}} - 1)x_{\text{Al}} \end{aligned}$$

where $\varepsilon_{\text{AlGaN}}$ is the dielectric constants, d_{31} is a relevant piezoelectric constant, d is the height of $\text{Al}_x\text{Ga}_{1-x}\text{N}$ barrier layers, $e\phi_b$ is Schottky barrier height, E_F is the Fermi level with respect to GaN conduction-band-edge energy at an AlGaN/GaN heterointerface, ΔE_c is conduction-band discontinuity, and x_{Al} is Al concentration [63].

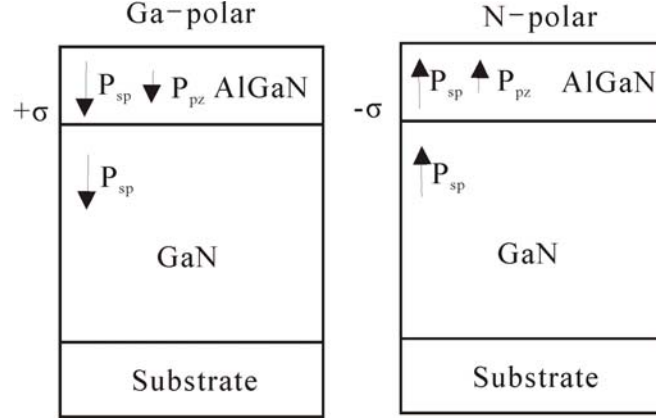


Figure 15: The direction of spontaneous and piezoelectric polarization and sheet charge density in Ga-polar and N-polar AlGaN/GaN heterostructures [10].

The direction of polarization can be determined by the polarity of III-nitrides, which also affects the 2DEG density. Tensile-strained AlGaN layers on relaxed Ga-polar GaN layers have a direction of polarization opposite to a growth direction, as shown in Figure 15 [10]. Thus, sheet charge density is positive ($+\sigma$), and free electrons will accumulate to compensate the polarization-induced charge [10]. In the case of AlGaN layers on N-polar GaN layers, negative sheet charge density ($-\sigma$) is induced at the heterointerface, causing 2DEG depletion or the accumulation of holes, as shown in Figure 15. [10]. Polarization-induced charge density at AlGaN/GaN heterostructures is given by [10]

$$\sigma = \mathbf{P}(\text{AlGaN}) - \mathbf{P}(\text{GaN}) = \mathbf{P}_{\text{SP}}(\text{AlGaN}) + \mathbf{P}_{\text{PE}}(\text{AlGaN}) - \mathbf{P}_{\text{SP}}(\text{GaN})$$

Tensile-strain between the AlGaN layers and the GaN bulk layers causes piezoelectric polarization, resulting in maximized 2DEG density. The tensile strain is mainly affected by the thickness, Al compositions, and roughness of AlGaN layers [10].

In summary, the conduction-band discontinuity and polarization are important control factors for forming 2DEG.

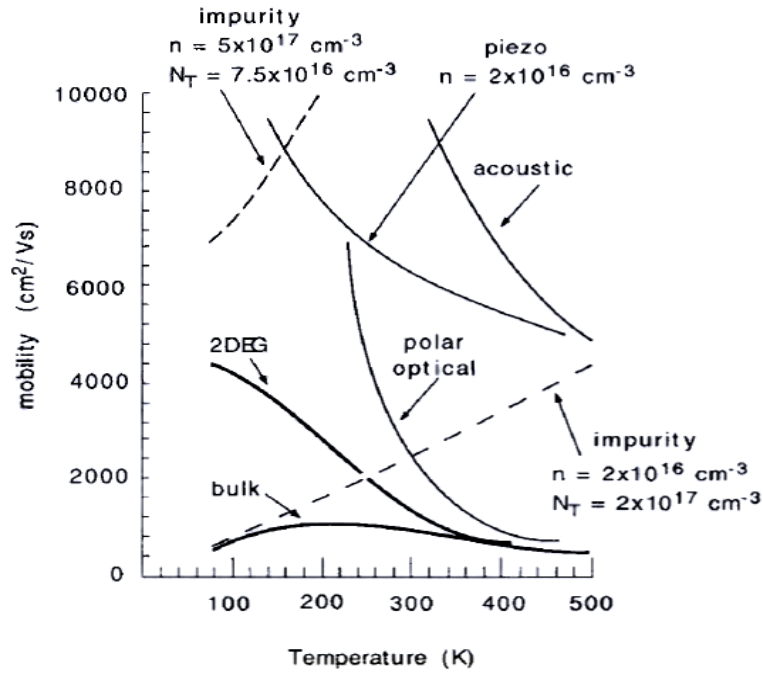


Figure 16: Temperature dependencies versus electron drift mobility in GaN, including impurity scattering: electron concentration (n) and ionized impurity (N_T) [65].

3.5 Mechanisms of degrading electron mobility in HEMTs

Pearton et al [64] reviewed the following two research works [65,66] to show the mechanisms of degradation of the electron mobility in GaN films. M. Shur et al. [65] have shown that electron mobility in the 2DEG would be degraded by scattering mechanisms dominated by polar optical scattering, ionized impurity scattering, and piezoelectric scattering in the 2DEG (with $n > N_T$) and GaN bulk (with $n < N_T$), as shown in Figure 16, where electron concentration, n , and the total concentration of ionized impurities, N_T . In the work, the electron mobility has been theoretically calculated and

comparable to measured values of $\mu = 2019 \text{ cm}^2/\text{Vs}$ with the sheet charge of $1.3 \times 10^{13} \text{ cm}^{-2}$ at $T = 300 \text{ K}$ and $\mu = 8583 \text{ cm}^2/\text{Vs}$ with the sheet charge of $1.0 \times 10^{13} \text{ cm}^{-2}$ at $T = 300 \text{ K}$ and $T = 77 \text{ K}$, respectively [50]. N. Weimann et al. [66] have reported another scattering mechanism at charged vertical dislocation lines, one of dominant defects in GaN bulk layers. These acceptor-like dislocations have trapped negatively charged electrons, resulting in their acting as scattering centers in the shape of lines. The calculated transverse mobility at charged dislocation lines is plotted in Figure 17 as a function of dislocation density and doping. In addition, Y. Zhang et al. [67] have calculated the effect of mobility variations in the 2DEG dependent on the interface roughness of AlGaIn/GaN heterostructures and Al contents of AlGaIn layers as shown in Figure 18. A rough surface has decreased electron mobility in the 2DEG. Higher Al contents in AlGaIn layers have increased piezoelectric field and sheet charge density, resulting in degraded channel mobility due to significant alloy scattering. Each of these mechanisms can contribute to the totality of mobility reduction. As will be shown later in chapters 7, 9 and 10, interface roughness and polarity inversions creating scattering centers are the dominant mechanisms for reduction of HEMT mobility when grown on LN and LT.

In summary, this section discussed the basic material properties, contact properties, and fundamental operation of GaN based high electron mobility transistor (HEMT) devices. The GaN-based HEMT devices have high electron mobility caused by the 2DEG, resulting in outstanding rf performance. The carrier density in the 2DEG is dominated by polarization, which acts as a primary source of electrons in the channel of heterostructures. Additionally, the mobility is limited by the dislocation density,

polarization scattering, and interface roughness. The dislocation density and interface roughness could be improved by a shutter modulation technique, which provides improved grain size and surface morphology as addressed in Chapter 7. The next chapter will discuss the polarity control of 2DEG and how to provide better epitaxial growth of III-nitrides for better device performance.

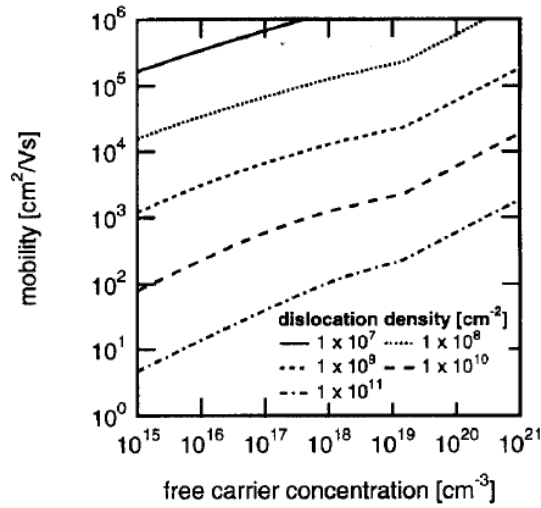


Figure 17: Transverse mobility components because of scattering at charged dislocation lines [66].

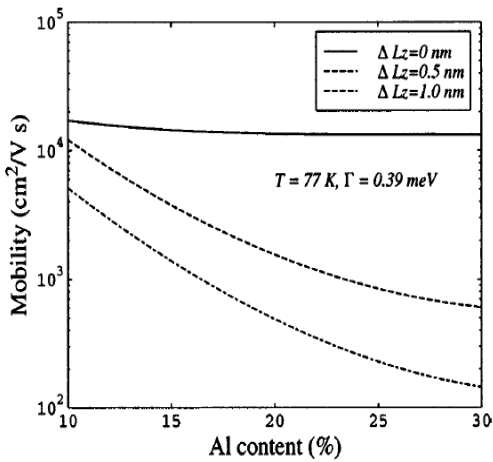


Figure 18: Electron mobility over Al contents with different interface roughness degrees, Lz is the height of random islands at an AlGaN/GaN heterointerface [67].

CHAPTER 4: EPITAXIAL GROWTH CONDITIONS FOR III-NITRIDES ON FERROELECTRIC MATERIALS

There are several aspects to be considered for making better epitaxy growth of III-nitrides on ferroelectric materials. First, lattice mismatch between III-nitrides and ferroelectric materials needs to be minimized, resulting in reducing the dislocation density of films. Second, the electrostatic boundary condition needs to be considered for controlling the polarization directions of epitaxy films. III-nitrides and ferroelectric materials are polar materials, which have polarization directions. The two different polarizations generate surface charges at the interface between the two polar materials because of the electrostatic boundary condition. Third, the crystalline stability of ferroelectric materials needs to be considered for improving the crystal quality of epitaxy films. The crystalline stability measured by spectroscopic ellipsometry shows that the ferroelectric materials have different crystalline/chemical phases with temperature variations. Fourth, there are some practical difficulties to grow III-nitrides on the ferroelectric materials. Finally, the surface chemistry between III-nitrides and ferroelectric materials is studied by x-ray photoemission spectroscopy (XPS) and Auger electron spectroscopy (AES). The first three aspects, lattice mismatch, electrostatic boundary condition, and crystalline stability are discussed in this Chapter 4. The practical difficulties are addressed and are solved by suggested solutions in Chapter 5. The final surface chemistry is discussed in Chapter 6.

4.1 Lattice mismatches

One of the critical hindrances of developing III-nitrides has been the lack of substrate materials that have suitable lattice-matching and thermal compatibility. Typically, III-nitrides have been grown on foreign substrates such as GaAs, sapphire, or SiC, with large lattice mismatches and less thermal compatibility, leading to extremely high defect density [68]. Sapphire has been the most widely used substrate to grow III-nitrides because of its wide availability, hexagonal symmetry, ease of handling, and crystalline stability at high temperatures ($\sim 1000^\circ\text{C}$). Sapphire has a lattice mismatch of $\sim 16\%$ to GaN in Figure 19a and a small thermal conductivity of ~ 35 W/mK, which is almost five times lower than that of GaN. While lithium niobate (LN) has a similar crystal structure on the c-plane as sapphire, it has a larger oxygen sub-lattice spacing in its surface structure, resulting in better average lattice mismatch to III-nitrides. LN has a lattice mismatch of 6.6% compared to GaN, as shown in Figure 19b. According to RHEED pattern studies, AlN (0001) grows on LN (0001) with an in-plane epitaxial alignment of $\text{AlN}[10\bar{1}0] \parallel \text{LN}[11\bar{2}0]$. The lattice mismatch between AlN and LN is nearly 4.7% [69]. Lithium tantalate has also a hexagonal structure with a lattice constant of 0.5154nm. LT has a lattice mismatch of 6.5% to GaN. The in-plane epitaxial relationship between GaN, AlN, and LT is $\text{GaN}[10\bar{1}0] \parallel \text{AlN}[10\bar{1}0] \parallel \text{LT}[11\bar{2}0]$ by RHEED pattern studies. The lattice mismatch between AlN and LT is about 4.6% [70]. Although the smaller lattice mismatch gives only minimal improvement in crystal structure, LN (LT) can be a promising substrate for III-nitride epitaxy. LN (LT) also has small thermal conductivity of ~ 38 W/mK. Thus, it needs to use the same strategies as sapphire to distribute heat dissipation in devices.

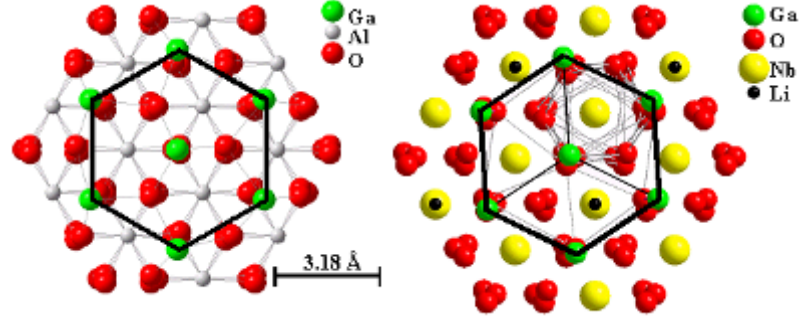


Figure 19: Crystal structures of (a) sapphire (left) and (b) LN (right) along c-axis showing GaN unit cell alignment on oxygen sublattice [1,2].

4.2 Electrostatic Boundary condition

In a homogeneous medium, there are no abrupt changes in electric field (\mathbf{E}) or electric flux density (\mathbf{D}). According to the Gauss's law, the divergence of the electric flux density is equal to the free charge density at the interface between two different media ($\nabla \cdot \mathbf{D} = \rho$). The electrostatic boundary condition on the normal component of \mathbf{D} can be derived as one a dimensional equation, in which the difference between two normal components of electric flux densities is equal to interface charge or sheet charge (ρ_{sheet}).

$$\mathbf{D}_1 - \mathbf{D}_2 = \rho_{sheet}$$

$$\text{or } (\varepsilon_1 \mathbf{E}_1 + \mathbf{P}_1) - (\varepsilon_2 \mathbf{E}_2 + \mathbf{P}_2) = \rho_{sheet}$$

where $\mathbf{D} = \varepsilon \mathbf{E} + \mathbf{P}$, ε is dielectric constant and \mathbf{P} is the total polarization of spontaneous, piezoelectric, and pyroelectric polarizations [71].

The electrostatic boundary condition can be applied to control the polarization directions of epitaxial films in two cases. First, the polarization direction can be controlled by only the properties of films in case of thin films grown on thick and non-

polar substrates. In this case, \mathbf{E} of the substrate is negligible and \mathbf{P} of the substrate is zero because of thick and non-polar substrates, respectively, as shown in Figure 20 (a). The second case is to control the surface charge by the properties of thin films and polarization direction of the substrate as shown in Figure 20 (b).

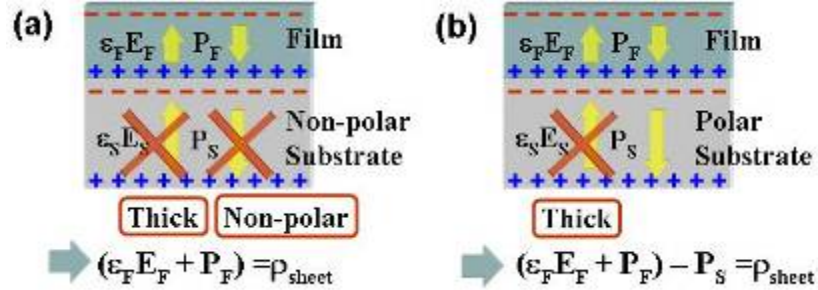


Figure 20: (a) In the case of films grown on non-polar substrates, the sheet charge (ρ_{sheet}) can be controlled by only film properties. (b) In the case of using polar substrates, the sheet charge is affected by film properties and the polarization direction of substrates [71].

The practical evidence of the polarization control is shown in Figure 21. In the experiment, GaN films were grown on periodically poled lithium niobate (PPLN), which was provided by Crystal Technology Inc. GaN films on PPLN had Ga-polar and N-polar domain walls alternatively, which are straight and parallel to the z-axis and y-axis of the crystal. Normally, PPLN has been used for nonlinear-optical materials in many infrared optical parametric oscillators because of its high nonlinearity, tuning capability, and robust repeatable process [72]. Figure 21 shows that Ga-polar and N-polar areas on GaN films on PPLN were disclosed after wet etching with phosphoric acid. Therefore, this disclosure is the evidence of controlling the polarization direction of films using the electrostatic boundary condition [1].

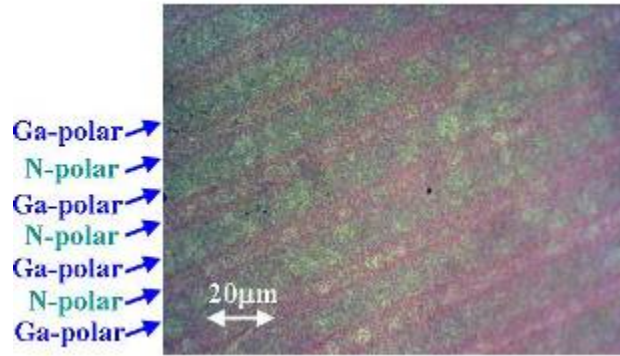


Figure 21: Experiment result of film polarization control using periodically poled lithium niobate observed by optical microscope. Red color area indicates N-polar and green color area indicates Ga-polar after etching with phosphoric acid [1].

4.3 Crystalline stability of lithium niobate and lithium tantalate

The thermal behavior of LN and LT and its impact on GaN growths were monitored using real-time spectroscopic ellipsometry, which investigated LN and LT modifications upon annealing to 800 °C in vacuum. Figure 22 shows the spectral dependence of the pseudorefractive index, $\langle n \rangle$, and pseudo-extinction coefficient, $\langle k \rangle$, of CLN, SLN, and LT crystals before any treatment. Since LN and LT are biaxial materials [73], the measured complex pseudo-refractive index is a mixture of ordinary and extraordinary refractive indexes. However, in the present study the ordinary and extraordinary contributions have not been separated, since we were only interested in detecting modification of the overall properties upon annealing. LN (LT) crystals are transparent up to photon energy of approximately 4 eV, where absorption begins and is associated with *d*-orbitals of the Nb (Ta)-metal, while the dominant residual absorption below 4 eV appears to be associated with OH impurities[74]. Figure 22(a) shows the effect of surface Li-enrichment of LN on the complex pseudo-refractive index, which consists of slight increases of the pseudorefractive index, seen at higher photon energies where the

sampling depth decreases, becoming more sensitive to the surface layer. Figure 22(b) shows the higher cut-off energy of 4.68 eV for LT compared to 4.05 eV for LN in the $\langle k \rangle$ spectra. The residual absorption below the cut-off energy has been attributed to OH-group impurities inside the crystal as well as on its surface and is detected by the 3484 cm^{-1} stretching mode in the FTIR spectra [75]. Furthermore, the LT is characterized by a complex pseudo-refractive index lower than LN.

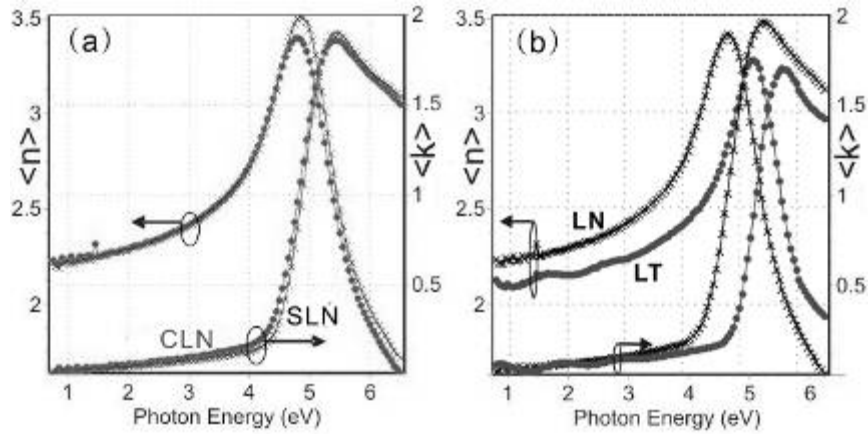


Figure 22: Ellipsometric spectra of pseudorefractive index, $\langle n \rangle$, and pseudoextinction coefficient, $\langle k \rangle$, of (a) CLN (circles) and SLN (cross) substrates (b) LT (circles) and LN (cross) substrates before any treatment.

Figure 23 shows the temporal variation of the above bandgap (4.5 eV) pseudo-refractive index and pseudo-extinction coefficient during annealing in vacuum at various temperatures in the range of 100 °C ~ 800 °C for CLN, SLN, and LT. For CLN, three different temperature regions were discerned on the basis of the variation of the pseudo-refractive index. In particular, in the range of 100 °C < T < 350 °C, a decrease of $\langle k \rangle$ and an increase of $\langle n \rangle$ were observed with increasing temperature. Those variations may be related to the degassing of the surface and the loss of OH groups present in the films, as supported in the present study by FTIR measurements reported by Herrington *et al.* [74].

This is because inhomogeneity caused by the presence of opposite direction domains arises in crystal with increasing temperature at $T > 800\text{ }^{\circ}\text{C}$ [27].

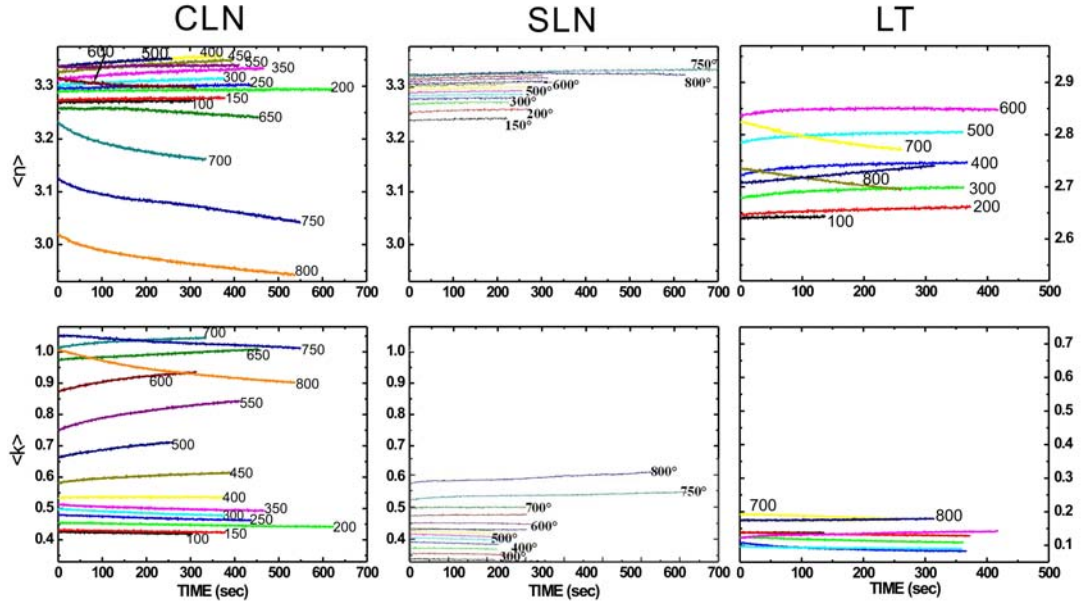


Figure 23: Time variation of the pseudorefractive index, $\langle n \rangle$, and pseudoextinction coefficient, $\langle k \rangle$, during annealing in vacuum at various temperatures in the range of 100°C - 800°C with an increment of 50°C for CLN, SLN, and CLT. The different initial point is because of the different temperatures investigated.

The trends reversed for temperatures $400\text{ }^{\circ}\text{C} < T < 700\text{ }^{\circ}\text{C}$, i.e., an increase of $\langle k \rangle$ was observed with increasing temperature. According to previous studies [76], these observations are likely related to the out-diffusion of Li and O from the outmost layer and surface segregation/accumulation of Li and O-species on the surface while the surface layer becomes Nb-rich. This is consistent with the changes observed in Figure 22. Furthermore, a strong decrease of $\langle k \rangle$ and $\langle n \rangle$ is observed for $T > 700\text{ }^{\circ}\text{C}$, which can be related to the decomposition of LN substrates [76] with surface evaporation of O-species

also as O₂ (loss of surface O) and Li desorption. Conversely, only surface degassing without decomposition is observed for SLN and LT in Figure 23, demonstrating their higher thermal stability.

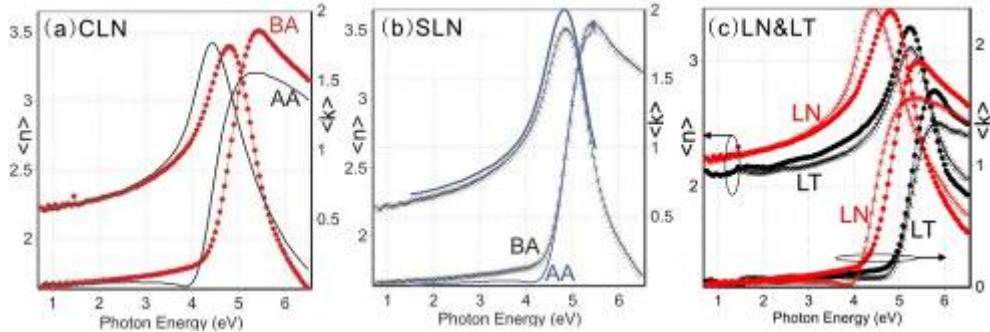


Figure 24: Ellipsometric spectra of the pseudorefractive index, $\langle n \rangle$, and pseudoextinction coefficient, $\langle k \rangle$, of (a) CLN and (b) SLN substrates before (BA) and after (AA) furnace annealing at 800°C for approximately 20 min. (c) comparison between LN and LT. Real time ellipsometric measurements are at 4.5 eV photon energy.

Figure 24 (a) and (b) compare the spectra of the complex pseudo-refractive index of the CLN and SLN before and after annealing at 800 °C for approximately 20 min. Figure 24c shows the comparison between LN and LT before and after annealing. A strong modification resulting from surface decomposition is observed for the CLN, which corresponded to a decomposition of approximately 8 nm of LN surface layer. On the contrary, almost no variation is observed for the annealed SLN and LT, indicating its higher vacuum thermal stability. Furthermore, the decrease of the residual absorption below 4 eV is consistent with the degassing of OH, and a broad band at energies below 4 eV appears for the annealed LN, whose amplitude depends on annealing times and temperatures. This band has been previously detected for LN and LT annealed in O₂-free

atmospheres. The origin of this peak has been the subject of controversy as reported by Jhans *et al.* [77] since it has been ascribed to polarons, or d-d transitions of niobium or to electrons trapped at oxygen vacancies originated during the surface decomposition or to cation and oxygen vacancies [78]. The higher thermal stability found for LT is in agreement with the lower Li_2O out-diffusion coefficient of $D \sim 10^{-10} \text{ cm}^2/\text{sec}$ for LN and of $D \sim 10^{-11} \text{ cm}^2/\text{sec}$ for LT at approximately $900 \text{ }^\circ\text{C}$ [79].

In summary, there were several aspects to be considered for better integration between III-nitrides and ferroelectric materials. Among the several aspects, the properties of lattice mismatch, electrostatic boundary condition, and crystalline stability were discussed in this chapter. LN and LT have smaller lattice mismatch to GaN films than that of sapphire and are polar materials, which have a benefit of the polarity control of GaN films. SLN and LT substrates showed better crystalline stability than CLN, and resulted in better GaN crystal quality. In the next chapter, several practical difficulties are addressed and resolved by suggested solutions.

CHAPTER 5: PRACTICAL ISSUES OF III-NITRIDE GROWTH ON FERROELECTRIC MATERIALS

As mentioned in Chapter 4, there are several aspects to be considered for epitaxial growth of III-nitrides on ferroelectric materials. This chapter addresses several practical difficulties to grow GaN films on ferroelectric materials and suggests solutions of the difficulties. First, lithium niobate (LN) or lithium tantalate (LT) substrates have cracked at high growth temperatures. This is because LN (LT) has a higher thermal expansion property compared to GaN. This cracking problem required design of a special spring plate to minimize mechanical stress on samples. Second, LN (LT) has poor adhesion of GaN films, resulting in the film peeling-off. This poor adhesion was improved using a furnace anneal step, which also enhanced the surface smoothness.

5.1 Cracking problem and special mounting for MBE growths

To absorb radiation from a substrate heater in an MBE system, transparent materials such as LN (LT), sapphire, or SiC must have a deposited metal coating on the back side, normally using tantalum, molybdenum, or titanium. To mount these samples inside the MBE system, spring plates made of molybdenum were used to hold the samples, which, however, induced mechanical stress on the samples. LN has an anomalously high thermal expansion coefficient (CTE) of $\alpha_{\perp} = 15 \times 10^{-6}/^{\circ}\text{C}$ and $\alpha_{\parallel} = 7.5 \times 10^{-6}/^{\circ}\text{C}$. LT has a high CTE of $\alpha_{\perp} = 16 \times 10^{-6}/^{\circ}\text{C}$ and $\alpha_{\parallel} = 4 \times 10^{-6}/^{\circ}\text{C}$ [80]. Therefore, the huge CTE of LN (LT) and the mechanical stress from the spring plate explain why earlier attempts to grow III-nitrides on LN (LT) resulted in cracked samples at high growth

temperatures. Thus, grips on the spring plate were adjusted to minimize the sample holding pressure, but were strong enough to hold a sample. Figure 25 shows the specially designed spring plate, which has almost two times longer grips than that of normal spring plates.

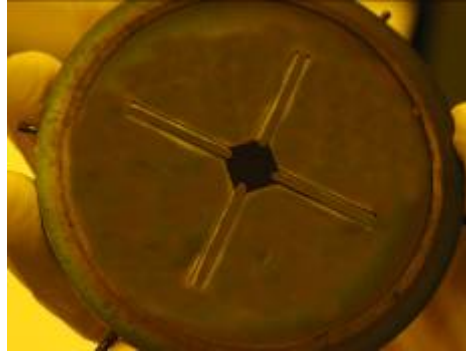


Figure 25: Specially designed spring plate with two times longer grips for reducing mechanical stress on the LN or LT.

5.2 Furnace annealing effects on lithium niobate and lithium tantalate

Even though LN (LT) samples had comparatively smaller lattice mismatch to III-nitrides than that of sapphires, earlier experiments had very low yields of successful growth of III-nitrides because of the delamination of epilayers grown thicker than $0.5 \mu\text{m}$. As-received LN (LT) samples had surface damage such as scratches and corrugations in nanometer scale range because of the factory mechanical polish, as shown in Figure 27(a), observed by atomic force microscopy (AFM). However, the surface damage was removed by high-temperature furnace anneals at $1000 \text{ }^\circ\text{C}$ in a dry air environment [4,90,91], resulting in atomically flat surfaces. The annealing furnace is shown in Figure 26.



Figure 26: Mini brute annealing furnace from Thermco Inc. with a customized fume hood and a flow meter system.

After annealing at 1000 °C for 2 hours in a dry air environment, the surface morphology of CLN showed atomically flat terraces of ~320 nm width between step-edges with an average vertical step height of 0.15 nm, Figure 27(b) and Figure 27(c). However, longer anneals degraded surface roughness as a result of facet coarsening and affected the variation of terrace width, as shown in Figure 27(d) and Figure 27(e). CLN (LT) samples produced atomically flat terraces of ~200 nm width after annealing for 3 hours, as shown in Figure 27(d), which were very similar to the annealed samples for 4 hours in Figure 27(e). However, after 5 hours of annealing, the surface became slightly porous and rough, as shown in Figure 27(f). These observations led to the conclusion that 2~3 hour anneals give the best surface condition with the largest terrace width, which is suitable for epitaxial growth. The surface morphology of as-received stoichiometric LN (SLN) in Figure 28(a) showed dramatic changes after annealing at 1000 °C in a dry air environment for 2 hours. The annealed SLN samples formed bunched steps and larger facets with periodic valleys of around 6 nm depths, as shown in Figure 28(b). The newly

formed facets and individual facets coalesced with longer anneals (10 hours), as shown in Figure 28(c).

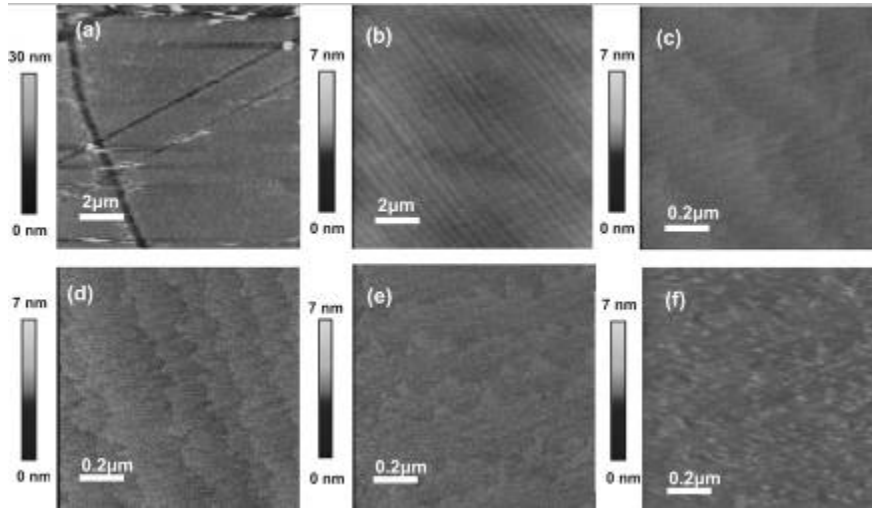


Figure 27: The surface morphologies of CLN samples observed by AFM (a) before annealing; (b) after annealing in a dry air environment at 1000°C for 2 hours and (c) in the same sample with different scale; the surface of LiNbO₃ after (d) furnace annealing in the same environment at 1000°C for 3 hours, (e) 4 hours, and (f) 5 hours.

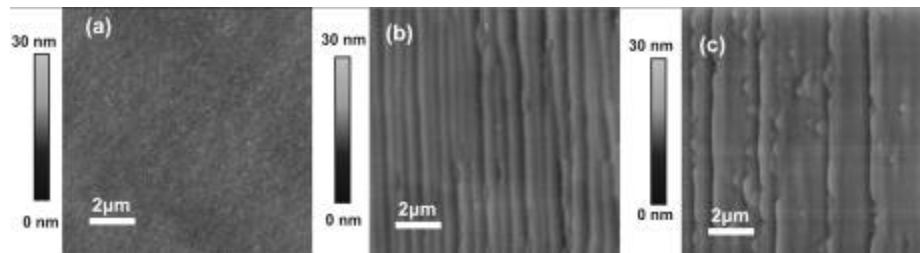


Figure 28: Surface of SLN samples by AFM for (a) as-received and (b) after furnace annealing in a dry air environment at 1000°C for 2 hours and (c) for 10 hours.

5.3 Polarity inversion domains and etching studies

Even though furnace anneals in a dry air environment improved surface smoothness, they caused the formation of polarity inversion domains on the surface of

LN samples. The polarity inversion domains on LN samples affected the polarity of GaN films, resulting in deteriorated mobility in III-nitride-based devices [4]. The polarity inversion domains on LN samples were delineated by an etching study, which used a mixture of acids ($\text{HF}:\text{HNO}_3 = 1:2$ in volume) for 45 minutes in a boiling water bath [81]. Figure 29(a)-(c) show etched surface morphologies of as-received CLN, furnace annealed CLN at 1000°C for 2 hours, and outgassed CLN in vacuum at 200°C for 1 hour, respectively. Figure 29(a) and Figure 29(c) barely show etching pits, but all regions of the furnace annealed samples in Figure 29(b) have etching pits in a triangular shape because of the faster etching rate around polarity inverted domain areas. Figure 29(d)-(f) show etched surface morphologies of (d) as-received SLN, (e) furnace annealed SLN, and (f) only outgassed SLN in vacuum for one hour. Even though the furnace annealed SLN sample has periodic valleys, there are few pits in Figure 29(f).

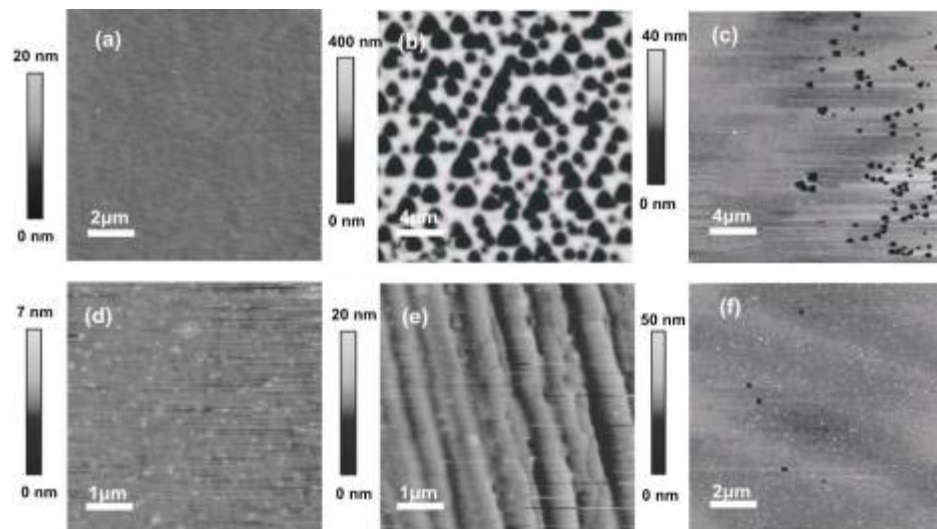


Figure 29: Study of etched LN samples: AFM surface morphologies of (a) as-received CLN, (b) furnace annealed CLN at 1000°C for 2 hours in a dry air environment, (c)

outgassed CLN at 200°C for 1 hour in vacuum, (d) as-received SLN, (e) furnace annealed SLN, and (f) outgassed SLN at 200°C for 1 hour in vacuum.

In summary, furnace anneals at high temperatures give atomically smooth surface of CLN samples with inverted domains, but corrugated surface on SLN samples without inverted domains. Future efforts on intermediate lithium composition materials may balance the advantages of lithium lean congruent sample smoothing during a furnace anneal with the lack of inverted domains found in SLN samples.

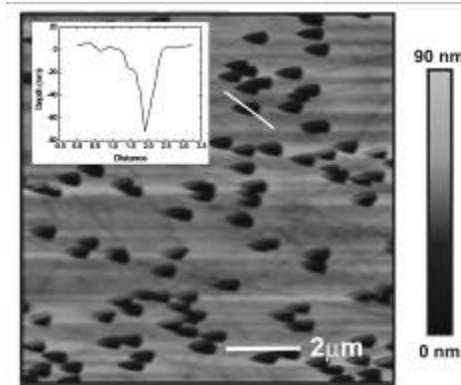


Figure 30: AFM image after etching with HF+HNO₃ acids in a boiled water bath for 3 minutes. These etch pits indicate the multi-ferroelectric domains of LN and LT samples.

Figure 30 shows the surface morphology of high-temperature annealed LT after etching with HF+HNO₃ acids for 45 minutes in a boiled water bath. Etch pits were observed on the sample, indicating that furnace annealed LT samples also had ferroelectric inverted domains. In general, LN (LT) samples have one degree of freedom for lithium atomic movement, along the z-axis, where ferroelectric polarization is determined by displacing Li atoms through the adjacent plane of oxygen [27]. Thus, the samples have a single polarization (or a single domain) by applying an external electric field during material growth to fix the Li atoms' displacement at one crystal lattice

position [27]. However, furnace anneals at high temperatures created variations in crystal composition because of the non-uniform evaporation of lithium from the near-surface of LN (LT) samples [27]. This resulted in a disruption of previous displacement of Li atoms near the surface. Therefore, the composition deviation of the near-surface affected the inverted domains on LN (LT) samples [27,82].

5.4 Polarity studies with various annealing temperatures

The previous section introduced the annealing effects that annealed CLN in dry air at 1000 °C had - atomically flat surfaces and the improvement of film adhesion. However, the annealed CLN had polarity inverted domain areas, a process called repolarization, which degraded the polarity uniformity of III-nitrides. These limiting factors have been obviated using stoichiometric LN (SLN: 49.9 mole% of Li_2O), which is very stable in vacuum over a wide-temperature range and also results in the better adhesion of the III-nitride films annealing, as confirmed by spectroscopic ellipsometry (SE), polarity etching and Kelvin probe force microscopy (KPFM).

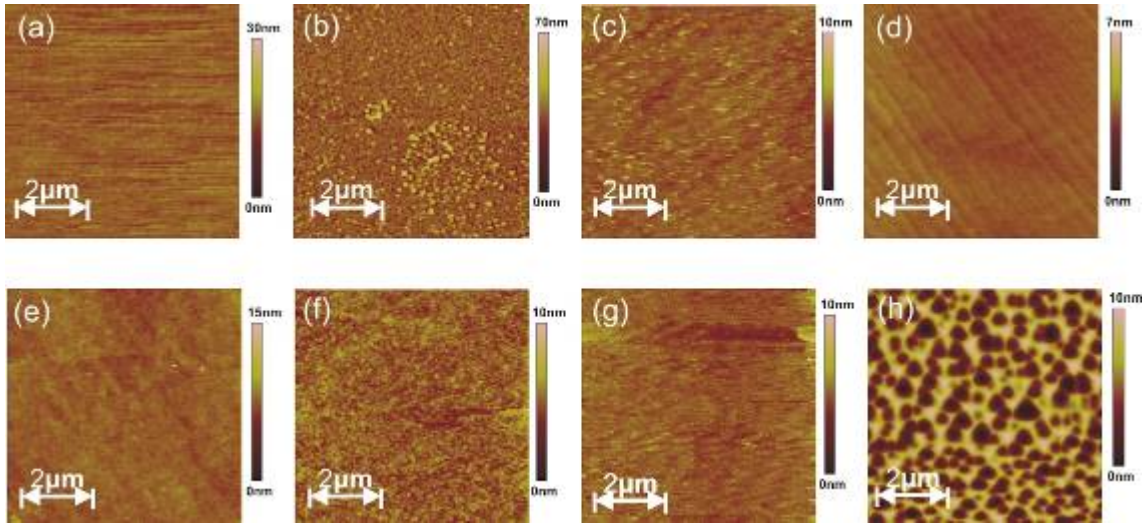


Figure 31: Surface Morphology by AFM on annealed Lithium Niobate with different conditions: Before wet-etching (a) ~ (d) and after wet-etching (e) ~ (h). Annealing temperatures of (a, e) 500°C, (b, f) 600°C, (c, g) 800°C, and (d, h) 1000°C.

The SLN solution resolves the limiting factors on CLN, however, is expensive and difficult to use because of the limited commercial availability of SLN. This limited availability leads to another solution that solves the problem of repolarization on CLN by lowering the annealing temperature at the expense of surface smoothness. The effects of various annealing temperatures on CLN are shown in Figure 31. The annealed CLN substrates show the surface roughness of (a) 1.3nm @ 500°C, (b) 5.58nm @ 600°C, (c) 0.46nm @ 800°C, and (d) 0.2nm @ 1000°C with no ferroelectric repolarization effect except when annealing at 1000 °C, as confirmed by etching ($\text{HNO}_3\text{:HF}=2\text{:1}$ at 100°C) in Figure 31(h). III-nitrides on the annealed LN with 500 °C and 1000 °C have no significant difference of GaN FWHMs in (0002) ω scan measured by high resolution x-ray diffraction (HRXRD). Therefore, annealing temperatures less than 1000 °C, while not providing the best surface smoothness, do provide no evident ferroelectric repolarization and improve film adhesion without degrading crystal quality.

5.5 Properties of ferroelectric materials at high temperatures

In the previous section, annealed CLN has the repolarization on the surface, which degrades the polarity uniformity of III-nitride films. To resolve the repolarization problem, it is necessary to understand the repolarization on the annealed CLN. Therefore this section explains the nature of the repolarization with high temperature annealing.

As temperatures increase, the unit cell of LN contracts along the c -axis and extends along the a axis, as shown in Figure 32a [31].

Xue et al [31] found that a LN (LT) structure has the stacking sequence of Li-Vacancy-Nb (Ta)-Li at room temperature. At higher temperatures, by electrically driving the Li^+ ion through the oxygen plane into the vacancy occupied octahedra, the spontaneous polarization of LN (LT) can be changed as shown in Figure 2 [31], resulting from Figure 32b.

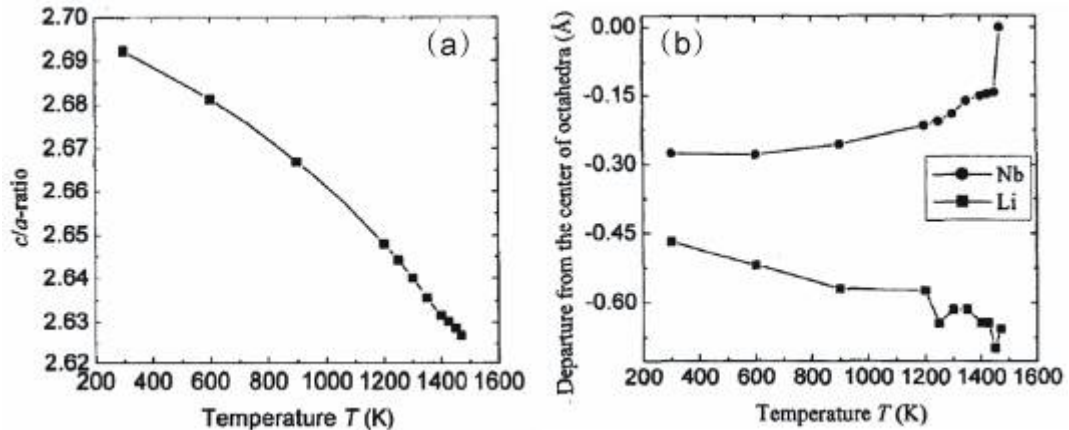


Figure 32: Temperature dependent behavior for (a) the ratio change of c -axis over a -axis, (b) the position change of Li^+ and Nb^{5+} : Nb^{5+} goes back to an original position, and Li^+ goes to the center of the bottom oxygen triangle plane of LiO_6 octahedron [31].

According to the statement of Xue et al [31], in Figure 32b, the Nb^{5+} goes back to an original position and Li^+ goes to the center of a bottom oxygen triangle plane at high temperatures. After cooling, the location of Li^+ would not be recovered to the original position, which leads to domain inversions, called repolarization, on the surface of LN crystals [31]. The depth of the repolarization region could reach up to one half of substrate thickness [83], and be suppressed using dehydrated LN and LT substrates, in which fewer hydroxides (OH) are contained [84]. The randomly located Li^+ is not only completely and permanently determined by heating, but also by an electrical field effect, called the coercive field.

Lines et al [85] defined the coercive field as the required electric field to switch the polarization of ferroelectric materials from having a remnant polarization to zero polarization. The calculated coercive field based on the phenomenological Landau-Ginzburg equation is several orders of magnitude greater than experimental values [85,86]. Kim et al [86] investigated that the practical calculation gap is from neglecting pre-existing domain wall. Using the Ginzburg-Landau-Devonshire equation [27], the experimentally observed coercive field can be approximated by summing the space-charge field and bulk dipolar defect field as follows [86]:

$$E_C \approx \pm 0.385 \alpha_1 P_S = \pm \frac{0.385 \times P_S}{2\varepsilon},$$

where dielectric constant ε , $\alpha_1 = 1/(2\varepsilon)$, $P_S = 0.75 \text{C}/\text{m}^2$ for LN, and $P_S = 0.55 \text{C}/\text{m}^2$ for LT. The directions of domains on ferroelectric materials can be inverted by applying external positive high voltage to the z^+ face of samples, which slightly exceeds the coercive field of materials [87]. The coercive fields of materials are $< 21 \text{ kV}/\text{mm}$ for

CLN, < 4 kV/mm for SLN, < 3.5 kV/mm for Mg doped (5 mol%) LN [87], < 21 kV/mm for CLT, and < 1.7 kV/mm for SLT at room temperature. The coercive fields are varied with temperatures, for example, 5 MV/mm at 25 °C and 5 kV/mm at 250 °C for CLT [88] and others [89].

Similar to LN, LT has spontaneous polarization, P_s , of 0.55 C/m^2 [86] and room-temperature lattice parameters in hexagonal indices of the a -axis: 5.143 \AA , c -axis: 13.756 \AA [39]. According to the statement of Roitberg et al [38], however, with increasing temperature, the unit cell of LT contracts along the a -axis maximally at $660^\circ \pm 10^\circ \text{ C}$, which is the Curie temperature of LT, as shown in Figure 33. Even though LN (LT) has repolarization at high temperatures in a dry air environment, the annealed LN (LT) has an atomically flat surface with step edges [4,90,91], which provides an ideal surface condition for epitaxial growths. The atomically flat surface is requisite for the layer-by-layer growth mode (Frank-vander Merwe growth mode) [92]. The nature of forming a step-edge structure may be related to repositioned octahedrons during high temperature anneals.

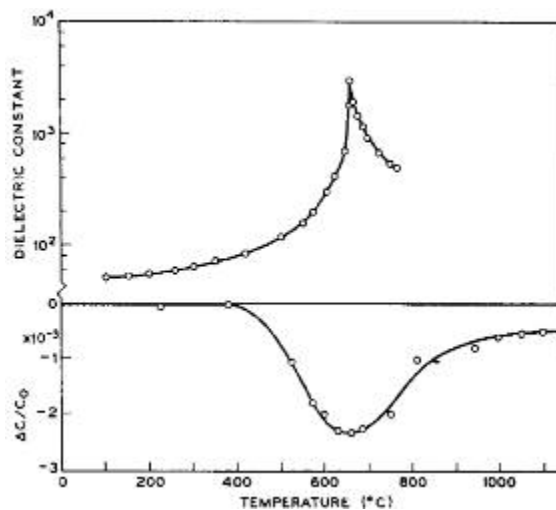


Figure 33: Variation in $\Delta c/c_0$ versus temperatures and variation in dielectric constant with temperatures in lithium tantalate [38].

In summary, this chapter addressed several practical difficulties to grow GaN films on ferroelectric materials and resolved some of the difficulties using including a new sample mounting method and high-temperature anneals. The new sample mounting method could minimize mechanical stress on samples and resolved the sample cracking problem. The high-temperature anneals could improve the adhesion properties of GaN films on ferroelectric materials. Even with a benefit of having an atomically flat surface on CLN, the high-temperature anneals developed repolarization domains, which induced inversion domains in subsequent III-nitrides. On the other hand, SLN and LT provided better surface repolarization and stability during the high-temperature annealing but at the cost of less surface smoothing. In the next chapter, the surface chemistry between III-nitrides and ferroelectric materials will be investigated.

CHAPTER 6: SURFACE CHEMISTRY

As introduced in Chapter 4, there are several aspects to be considered for making better epitaxy growth of III-nitrides on ferroelectric materials. This chapter presents the surface chemical and structural study of the interface between III-nitrides and ferroelectric materials using x-ray photoemission spectroscopy (XPS) and Auger electron spectroscopy (AES). The purpose of this study is to understand the interfacial properties of III-nitride growth on ferroelectric materials by studying the initial stages of deposition, disclosing various out-diffusion behaviors.

6.1 Introduction

The ferroelectric materials lithium niobate (LN) and lithium tantalate (LT) have been integrated with III-nitrides for optoelectronic applications [93,94,95,96,97,98]. The integration enhances the multi-functionality of electrical and optical devices. Several previous works demonstrated the integration of GaN-based high electron mobility transistor (HEMT) devices on LN, providing the possibility of cost-effective chips for optical and electronic devices [93,94,95]. Surface acoustic wave (SAW) devices were implemented by AlN epitaxial layers on LN, resulting in partially relieving the temperature instability and increasing the SAW velocity [96,98]. Stoichiometric LN (50 mole% of Li_2O) showed better crystalline stability than Congruent LN (48.39 mole % of Li_2O), resulting in improving device performance [99]. Furthermore, LT substrates were considered as a substrate for III-nitride growth [100]. That study pointed out that some residual conductivity existed beyond the channel in the AlGaIn/GaN grown on LN

substrates, resulting in degraded channel mobility. Therefore, the residual conductivity needs to be minimized to improve device performance. In this paper, the origin of the residual conductivity of GaN films on ferroelectric materials is investigated using x-ray diffraction (XRD), x-ray photoemission spectroscopy (XPS), and Auger electron spectroscopy (AES). This analysis will include an overview of interfacial properties and a description of the initial stages of the growth mechanism and impurity diffusion between GaN films and ferroelectric materials.

6.2 Stoichiometric effects of GaN films on LN substrates

Several GaN films were grown directly on LN substrates without buffer layers to study the properties of the nucleation layers of the GaN films. The LN samples were annealed at 500°C in a dry air environment to enhance the adhesion of GaN films [99,100,101]. Several GaN films were grown with various gallium fluxes and constant nitrogen flow at the same growth temperatures to verify the effects of V/III ratio on the GaN/LN interface with different growth regimes [102]. In this experiment, first, GaN films were grown in the intermediate Ga-rich (IGR) condition (sample A) at 600°C for 920Å thickness with a Ga flux of 8.4×10^{-7} Torr and 1.3 sccm nitrogen at an rf power of 350 watts. Second, GaN films were grown in the extremely Ga-rich (EGR) condition (sample B) with a Ga flux of 9.1×10^{-7} Torr after nitridation at 200°C for 30 minutes. Third, GaN films were grown in the extremely Ga-rich condition (sample C) with the highest Ga flux of 9.3×10^{-7} Torr after nitridation at 200°C for 30 minutes. Finally, GaN films were grown in the barely Ga-rich (BGR) condition (sample D) with a Ga flux of 6.1×10^{-7} Torr without nitridation. These four samples were grown using a shutter

modulation technique, which provided a significant improvement of the surface morphology and crystal quality of GaN films [103,104].

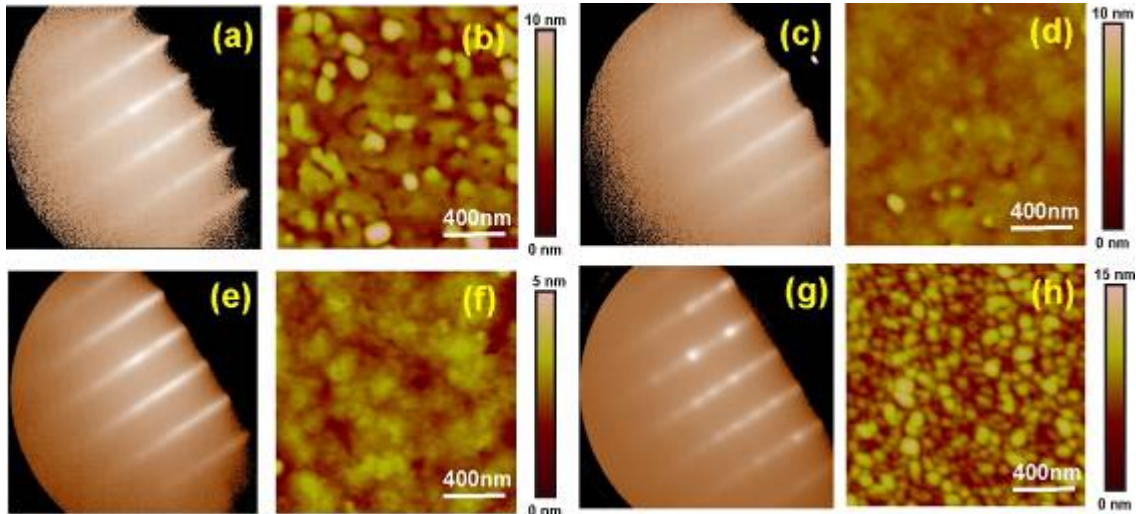


Figure 34: RHEED patterns of GaN films and surface morphologies with rms roughness: (a) at 6 min and (b) 1.03nm in sample A; (c) at 6 min and (d) 0.428nm in sample B; (e) at 6 min 30 sec and (f) 0.384nm in sample C; and (g) at 7 min 30 sec and (h) 1.13nm in sample D.

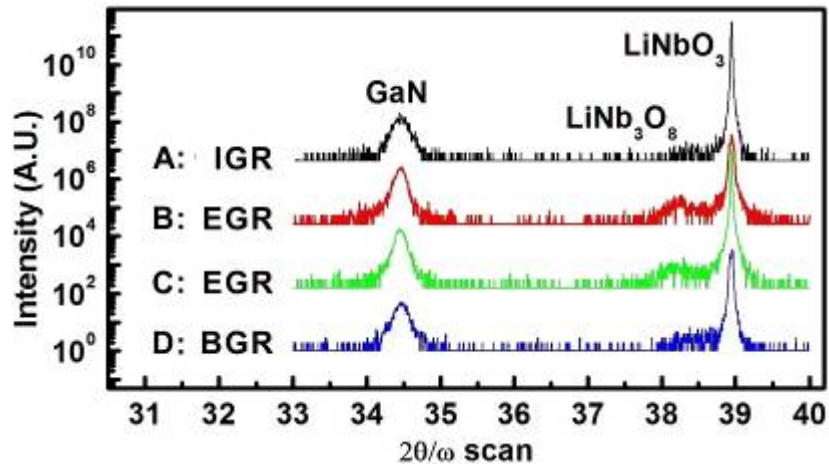


Figure 35: X-ray diffraction study on the four samples.

In general, stoichiometric GaN films have streaky RHEED patterns and a smoother surface. However, the GaN films in sample A showed streaky and spotty mixed

RHEED patterns and rough surface morphology with an rms roughness of 1.03 nm, as shown in Figure 34 (a) and (b). Sample A had a resistivity of $6.7 \times 10^{+4} \Omega/\square$ and an FWHM of 1.6638° on Ω -scan with 920Å thickness, resulting from the poor quality of nucleation layers. The minor phase separation in sample A was observed by XRD measurement, as shown in Figure 35.

Samples B and C grown in the EGR condition had very streaky RHEED patterns and smooth surfaces, as shown in Figure 34 (c), (d), (e), and (f). However, the samples had a resistivity $4.8 \times 10^{+2}$ and $5.3 \times 10^{+2} \Omega/\square$, respectively, which might be an inaccurate measurement because of un-etched Ga droplets on the surface. These samples had an FWHM of 1.3811° and 1.3644° with 880 and 1037Å thickness. Note that these samples grown in the EGR regime have more phase separation ($\text{LiNbO}_3 + \text{LiNb}_3\text{O}_8$) [99,100], confirmed by XRD measurement, as shown in Figure 35. This may be because Li from LN substrates tends to segregate into Ga. This is related to why GaN buffer layers block the out-diffusion inefficiently compared to AlN buffer layers, as discussed in [105]. Sample F grown in the BGR condition had spotty RHEED patterns and a rough surface. The sample had less phase separation compared to the other samples, confirmed by XRD measurement, as shown in Figure 35. The GaN films in sample D had the highest resistivity of $2.1 \times 10^{+5} \Omega/\square$ among the other samples. Also, sample D had an FWHM of 1.5308° with 974Å thickness. In conclusion, the BGR GaN layers offer a better capability of blocking the out-diffusion from substrates than do the BGR GaN films. Nitridation at low temperatures was expected to improve crystal quality [106], but instead resulted in no crystal quality improvement on LN substrates. The growth conditions and characterization of these samples are summarized in Table 1.

Table 1: Characterization of GaN films on lithium niobate substrates. n: carrier concentration as measured by Van der Pauw method, ρ : resistivity, ϕ : thickness (\AA), and FWHM: full width of half maximum of GaN diffraction on Ω -scan.

| Sample | Growth Condition | Ga flux (Torr) | N (cm^{-3}) | ρ (Ω/\square) | ϕ (\AA) | FWHM($^\circ$) |
|--------|-----------------------|----------------------|------------------------|-----------------------------|-------------------------|------------------|
| A | IGR No Nitridation | 8.4×10^{-7} | $-1.1 \times 10^{+19}$ | $6.7 \times 10^{+4}$ | 920 | 1.66 |
| B | EGR Nitridation | 9.1×10^{-7} | $-1.2 \times 10^{+20}$ | $4.8 \times 10^{+2}$ | 880 | 1.38 |
| C | EGR Nitridation | 9.3×10^{-7} | $-1.0 \times 10^{+20}$ | $5.3 \times 10^{+2}$ | 1037 | 1.36 |
| D | BGR No-Nitridation | 6.1×10^{-7} | $-1.7 \times 10^{+19}$ | $2.1 \times 10^{+5}$ | 974 | 1.53 |

6.3 Depth profiles and composition analysis with XPS and AES

The effects of impurities in GaN films on LN substrates were investigated using x-ray photoelectron spectroscopy (XPS) and Auger electron spectroscopy (AES). A PHI 10-360-4-015 hemispherical analyzer and PHI 04-173-0-077 Mg/Al dual anode non-monochromated x-ray source were used for XPS and a PHI 15-110B single pass cylindrical mirror analyzer was used for AES [107]. XPS depth profile and composition analysis were performed on the four samples, which evaluated the interface properties of GaN films on LN substrates. Argon ions with a kinetic energy of 4 keV were injected over $4 \times 4 \text{mm}^2$ to etch III-nitride films. The analysis areas of XPS and AES were about 1.1mm^2 and $5 \mu\text{m}^2$, respectively. XPS peak shape processing was performed using a full width at half maximum (FWHM) ranging from 1.3 to 1.8eV for different elements with a Lorentzian-Gaussian convolution-type model (an 80% Gaussian and 20% Lorentzian peak shape), calibrated by a clean $\text{Au}4f_{7/2}$ photo-electron peak showing a FWHM of 1.2eV.

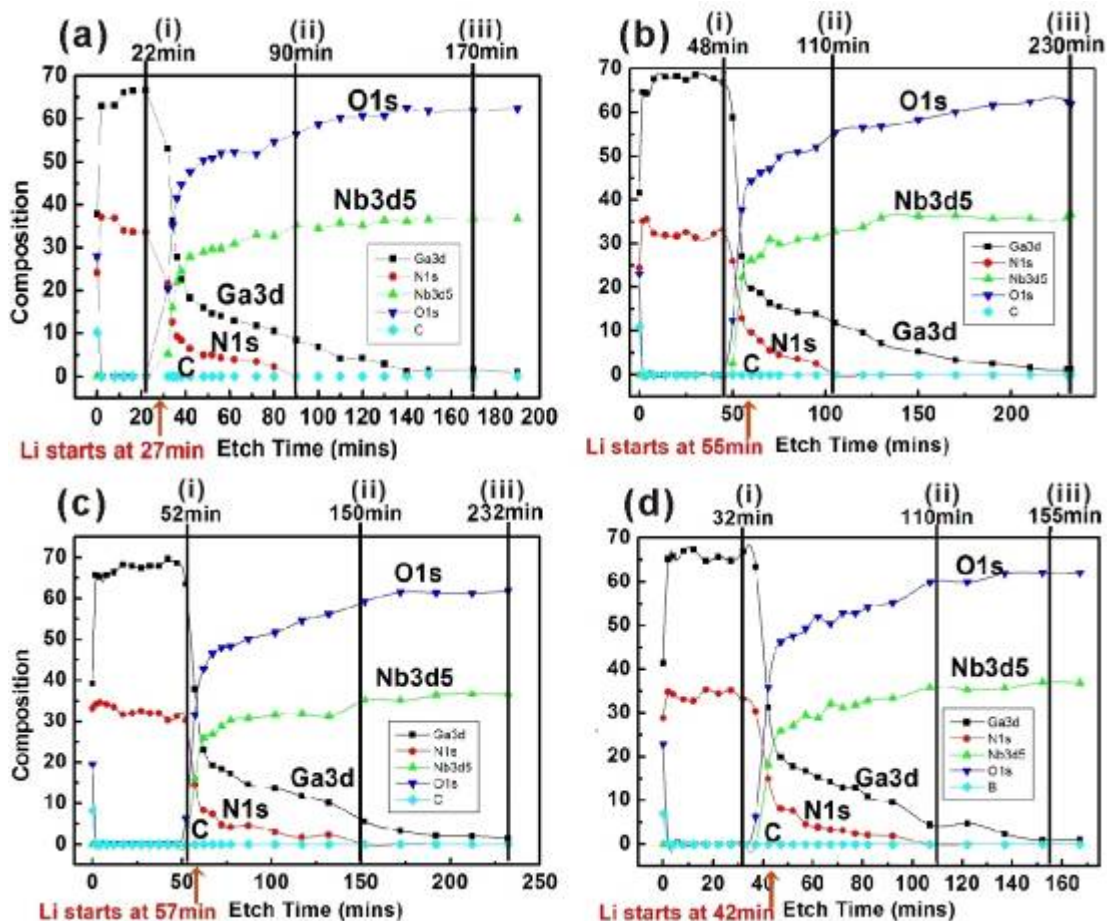


Figure 36: The depth profiles of (a) sample A, (b) sample B, (c) sample C, and (d) sample D, where (i): the start point of intermixing layer, (ii): the end of nitrogen diffusion, and (iii): the end of gallium diffusion.

The composition analysis on the surface of the four samples using XPS and AES is summarized in Table 2. The XPS composition results were from one measurement and the AES composition results were averaged for three different measurements. All measurements were performed after etching to clean the surface. The XPS and AES had the following sampling depths: XPS: Ga2p - 16Å, Ga3d - 68Å, N1s - 51Å, Nb3d5 - 60Å; and AES: Ga - 72Å, N - 27Å, Nb - 18Å. Sample A had a small density of Ga droplets, samples B and C had many Ga-droplets, and sample D had very few Ga-droplets. Note that the excess gallium on top of the GaN films were oxidized in air and changed to

gallium oxides, which is confirmed by the two bonding states of Ga2p shown in the XPS analysis.

Table 2: Surface composition analysis of the four samples using XPS and AES.

| Element (±10%) | Sample A, IGR No-Nitridation | | Sample B, EGR Nitridation | | Sample C, EGR Nitridation | | Sample D, BGR No-Nitridation | |
|-------------------|---------------------------------|------|------------------------------|------|------------------------------|------|---------------------------------|------|
| | XPS | AES | XPS | AES | XPS | AES | XPS | AES |
| | Ga | 44.3 | 39.7 | 47.0 | 45.6 | 50.2 | 51.6 | 49.3 |
| N | 28.4 | 13.4 | 29.3 | 14.9 | 41.5 | 29.8 | 37.8 | 25.8 |
| O | 20.1 | 17.9 | 15.9 | 17.7 | 8.4 | 7.5 | 12.9 | 15.2 |
| C | 7.2 | 27.6 | 7.8 | 21.8 | 0 | 11.1 | 0 | 10.6 |
| Nb | 0 | 0 | 0 | 0 | 0 | 0 | 0 | 0 |
| Ga/N | 1.56 | 2.96 | 1.60 | 3.06 | 1.21 | 1.73 | 1.30 | 1.88 |

The degree of impurity diffusion into the GaN film was evaluated using XPS depth profiles for the four samples, as shown in Figure 36. The Ga/N ratios of the four samples were 1.97, 2.10, 2.16, and 1.90 in the GaN films, respectively. Note that the XPS depth profiles were performed after the surface chemical bonding analysis, which will be shown in the next section. This is because bonding information is not reliable after the samples have been damaged by argon ion bombardment. The depth profile information was given in time because of the lack of knowledge of GaN etch rate. However, a rough estimation of the GaN etch rate was approximately 10 Å/min, based on a known thickness of SiO₂/Si. Li detection information was not included in the depth profiles because the Li peak overlapped with the Nb4s peak. Even though the Li peak was hard to qualify, the time of the Li appearance in the spectra was indicated approximately. Note that the absolute values of the Ga/N ratio can be influenced by different etch rates of Ga and N because of the different sputter rates of the materials. The Ga/N ratio of the

apparent film was an average of the depth profiles before the appearance of oxygen and/or niobium. A summary of the depth profiles of the four samples is provided in Table 3.

Table 3: The summary of depth profiles of the four samples.

| Sample | Growth Condition | Apparent Film “thickness” and Ga/N ratio | Nitrogen Diffusion Depth | Gallium Diffusion Depth |
|--------|-----------------------|--|--------------------------|-------------------------|
| A | IGR No-Nitridation | 22 min / 1.97 | 68 min | 148 min |
| B | EGR Nitridation | 45 min / 2.10 | 65 min | 182 min |
| C | EGR Nitridation | 52 min / 2.16 | 100 min | 180 min |
| D | BGR No-Nitridation | 32 min / 1.90 | 78 min | 118 min |

The samples had relatively constant composition except sample C. The Ga/N ratio and film thickness for each sample were matched to that expected from the growth conditions. During depth profiles, the relatively uniform composition of films suggested well-formed GaN films. Samples B and C showed significantly wider inter-mixed regions than those of the other two samples. One of the reasons for the wider inter-mixed regions could be the nitridation on these two samples, B and C, resulting in more nitrogen diffusion into the substrates. Furthermore, as mentioned earlier, the excess gallium on the two samples pulled out more impurities (e.g., lithium oxide), resulting in greater phase separation ($\text{LiNbO}_3 + \text{LiNb}_3\text{O}_8$), confirmed by XRD measurement in Figure 35. Note that the gallium in-diffusion was deeper than the nitrogen in-diffusion in all samples. Sample C showed the largest inter-mixed region, which had the deepest in-diffusion of gallium and nitrogen. Note that even though sample B and C showed unexpected Ga/N ratio on

surface layer level as shown in Table 2, they had the expected Ga/N ratio in the depth profiles as shown in Table 3. This behavior is unclear at this moment, but it may have resulted from irregular etching effects or surface roughness differences between samples

6.4 Surface Bonding analysis with XPS

The surface bonding energy of the four samples was analyzed using XPS to provide an understanding of the chemical interaction. Figure 37, Figure 38, and Figure 39 show the Ga2p, Ga3d, and N1s core-level spectra for the four samples, A, B, C, and D before and after sample surface cleaning. Legends in the figures indicate the bonding states of each element.

As-received GaN showed that oxidation on the surface caused a surface charge of 0.7 ~ 1.1eV, observed by the position of the surface C1s peak (284.6eV). After cleaning by Ar⁺ ion bombardment for 1 minute, the surface charge reduced to 0.1 ~ 0.3eV because of oxide removal. The intensities for all of the XPS spectra reported here were normalized for comparison and were calibrated by the C1s peak (284.6eV) of adventitious carbon.

The surface sensitivity of the XPS analysis is determined by the inelastic mean-free path of the electrons in the samples. Thus, peaks at different energy positions have different surface sensitivities. Since the Ga2p and Ga3d photoelectrons have inelastic mean-free paths of 0.5nm and 2.7nm, respectively, the Ga2p peaks have more surface-sensitive information and the Ga3d peaks have more bulk-sensitive information [108].

In Figure 37(a), after 16Å deep surface analysis, the as-received four samples have two peaks of the Ga2p spectra that are detected at 1118.0eV for Ga-N bonding and

1119.0eV for Ga-O bonding. These peaks are nearly matched to 1118.2eV for Ga-N bonding and 1119.5eV for Ga-O bonding on oxidized polycrystalline GaN powder [109,110]. The peak shift from Ga-O to Ga-N bonding is around 1.0eV for all four samples. These shifts are close to a peak shift of 1.3eV of Ga-O to Ga-N bonding [110]. *This implies that the gallium atoms on the surfaces of all samples were oxidized.* The majority of Ga-O bonding energy could be from the oxidized excess metallic gallium on top of the GaN films [111]. The number of Ga-O bonds in the four samples was 20.5, 58.8, 5.9, and 15.3% for samples A, B, C, and D, respectively. The number of Ga-O bonds of the samples was proportional to the supplied Ga-flux for the samples except sample C. This exception could be from an incomplete etch during a wet-etching process used to remove the residual droplets on the GaN films before XPS analysis.

After surface cleaning and thus, approximately 16Å deep into the surface, the Ga-O bonding peaks disappeared in samples A and B and were significantly reduced in samples C and D, as shown in Figure 37(b). Thus, samples C and D had 5.7% and 3.3% of Ga-O bonding, respectively. The surface cleaning procedure confirmed the removal of oxidized excess metallic gallium atoms on the surface of the GaN films and indicated that the oxidation resulted from the atmospheric exposure, not from the oxide substrate out-diffusion. Therefore, Ga-O bonds were mainly the result of the oxidized excess metallic Ga on top of the GaN films [111], confirmed by the surface-sensitive Ga2p spectra analysis after surface etching.

Ga3d peaks were detected using XPS high-energy resolution scans with an energy resolution of 0.08eV [112], as shown in Figure 38(c) for as-received samples and (d) for cleaned samples. No metallic Ga peaks were detected at 18.7eV [113]. In Figure 38(c),

the Ga3d core level peaks were detected at 19.6eV for Ga-N bonding and 20.6eV for Ga-O bonding. These peaks are similar to the reported data of 19.6eV for Ga-N bonding, which represents a single Ga atom bonded to 4 N atoms, and 20.8eV for Ga-O bonding [110]. The as-received four samples had bonding energy shifts of 1eV between the Ga-N and Ga-O bonds, which almost matched the reported binding energy shift of 1.2eV [110].

After cleaning the sample surface, there was no significant change of Ga3d core level peaks, as shown in Figure 38(d), because surface cleaning by low-energy Ar⁺ removes less than approximately 1 nm of the film from the surface, which is much thinner than the sample depth for Ga3d of around 7nm. The Ga3d core level peaks were detected at 19.6eV for Ga-N bonding and 20.6eV for Ga-O bonding. The binding energy shift was 1eV for the four cleaned samples. Compared to the metallic gallium peak at 18.7eV [113], Ga-O bonding peaks and Ga-N bonding peaks were shifted as 1.9eV and 0.9eV, respectively, for both the as-received samples and the cleaned samples. A higher shift for Ga-O bonding resulted from the greater electronegativity of the oxygen atom compared to the nitrogen atom.

The oxidation of GaN has been studied by many groups using XPS to reveal information about Ga-O bonding, including a peak shift in the Ga3d binding of 0.5 ~ 1.2eV energy from Ga-O to Ga-N [110,114,115]. The range in shift reported in the literature implies that the oxidized excess Ga atoms may form different bonds with oxygen and/or nitrogen, a hybrid Ga-O-N, on the sample surface [116]. The hybrid Ga-O-N bonding was detected at the binding energy of 20.2eV in Ga3d spectra. Another possibility for the peak shifts is a hydrogen-related complex Ga-H-N, which was detected at 19.21eV [117] although no significant source of hydrogen is available to these MBE

grown samples. Therefore, the oxidized or hybridized GaN films could be from surface contamination in air resulting in oxygen or hydrogen bonding.

Table 4 shows the Ga-O/Ga-N, Ga-N/N, and Ga/N ratios for the four samples using Ga3d peak, O1s, and N1s peaks. All of the ratios increase as Ga-flux is increased except sample E. As mentioned earlier, the etch process before XPS analysis may cause this discrepancy. The high Ga-O/Ga-N ratio indicates a high degree of oxidation on the GaN films. The data indicates that the GaN films in the four samples are oxidized, as Ga-O-N and the Ga/N ratios are higher than the designated values. The nitrogen-deficient GaN films are not necessarily interpreted as nitrogen vacancies because the missing nitrogen atoms are replaced with oxygen atoms, which act as *n*-type donors [112].

Table 4: Bonding energy percentage ratio summary with various comparisons, derived from XPS analysis of Ga 3d peaks and N 1s peaks.

| Sample | Growth Regime | As-received | | | Cleaned | | |
|--------|-----------------------|-------------|--------|------|-----------|--------|------|
| | | Ga-O/Ga-N | Ga-N/N | Ga/N | Ga-O/Ga-N | Ga-N/N | Ga/N |
| A | IGR No-Nitridation | 0.28 | 1.15 | 1.48 | 0.34 | 1.16 | 1.56 |
| B | EGR Nitridation | 0.31 | 1.32 | 1.74 | 0.32 | 1.21 | 1.60 |
| C | EGR Nitridation | 0.10 | 0.97 | 1.07 | 0.24 | 0.98 | 1.21 |
| D | BGR No-Nitridation | 0.24 | 1.00 | 1.24 | 0.27 | 1.02 | 1.30 |

N1s peaks are shown in Figure 39(e) for as-received samples and (f) for cleaned samples. In the N1s spectra, N-Ga bonding peaks were detected at 397.1eV for both the as-received samples and at 397.2 ~ 397.4eV for the cleaned samples, which were in good

agreement with the reported values of 397.2eV [118]. Note that the N1s spectra had the second unknown peaks, noted N-O in the figure, shifted to a higher energy at 398.8eV for both as-received samples and cleaned samples. This might indicate that nitrogen bonded with such elements that are more electronegative than gallium does. The bonding state of this peak is not yet fully understood. The peak could originate from a complex intermediate bonding state involving Ga-N-O bonds and/or nitrogen dangling bonds centered at 400.3eV [119] or/and N-H bonds centered at 399.7eV [117]. The N-H binding energy was analyzed using samples grown by NH₃ sourced MBE. The source of hydrogen could be the LN substrates, which generated O-H elements [120] but it is expected that such a source of hydrogen would not be detectable by surface analysis. N-H was considered as a hydrogen-related donor candidate responsible for the high electron background concentration in the GaN films [117].

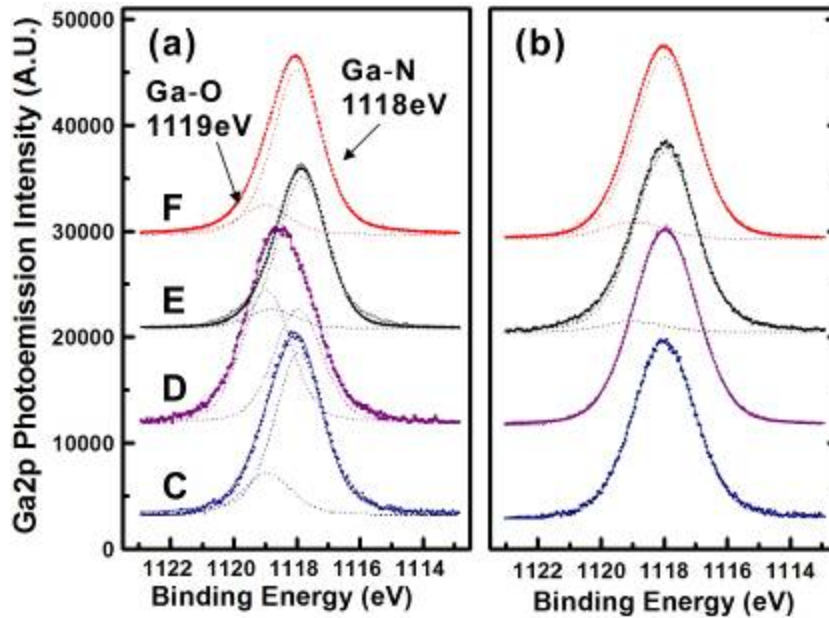


Figure 37: XPS spectra of Ga2p photoelectron peaks of (a) as-received and (b) cleaned four samples.

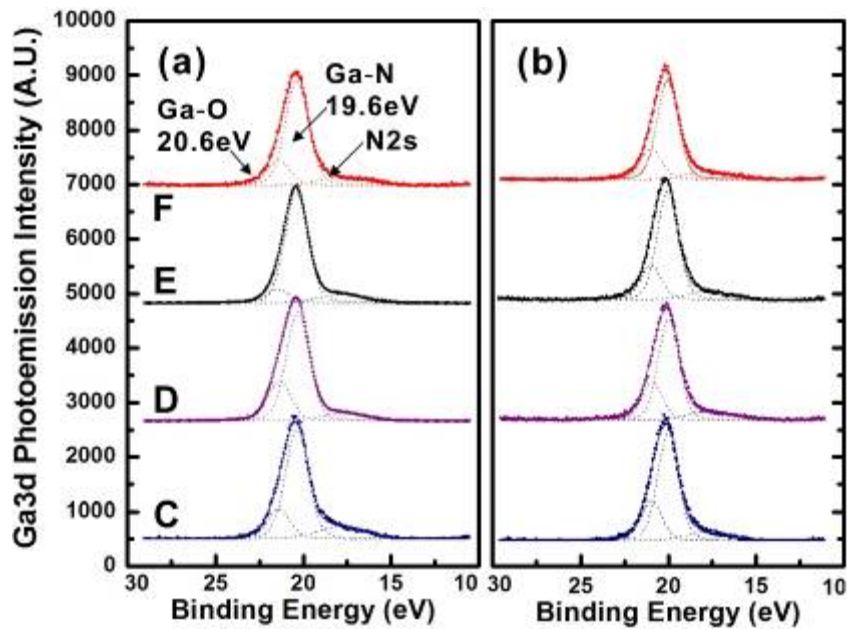


Figure 38: XPS spectra of Ga3d photoelectron peaks of (a) as-received and (b) cleaned four samples.

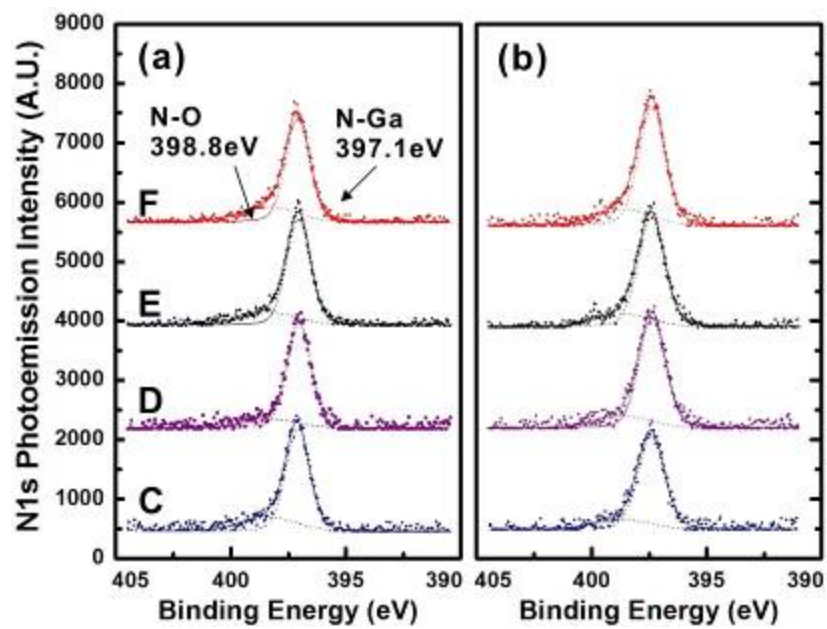


Figure 39: XPS spectra of N1s photoelectron peaks of (a) as-received and (b) cleaned four samples.

6.5 Conclusion of chemical analysis

In this chapter, the origin of the conductive GaN films on ferroelectric materials was investigated using XRD, XPS, and AES analysis tools. The study showed that oxygen-related impurities dominantly have a deleterious effect on the resistivity of GaN films on ferroelectric materials. The origin of impurities and interdiffused layers and their effects were investigated at the nucleation layers of GaN films on ferroelectric materials in depth. The extremely Ga-rich GaN films showed greater phase separation of LN substrates and had a higher conductivity than that of barely Ga-rich GaN films. The depth profiles showed the impurity diffusion in both GaN films and LN substrates. The bonding energy analysis showed that all of the elements had shifted peaks, resulting from oxidization in GaN films. It is concluded that direct GaN film growth on ferroelectric materials is forbidden because of the interdiffusion problem and is made worse with higher Ga flux (wetter nucleation). To suppress the interdiffusion, non-conductive buffer layers need to be grown between the GaN films and ferroelectric materials.

CHAPTER 7: III-NITRIDE GROWTH ON FERROELECTRIC MATERIALS

The first integration of III-nitrides on ferroelectric materials was published in 1999 [7]. In the work, GaN layers were grown on SrTiO₃(100) substrates using gas source reactive molecular beam epitaxy (RMBE), resulting in strong *c*-oriented nature and the polycrystalline structure of GaN films on SrTiO₃. Then, aluminum nitride (AlN) layers were deposited on z-cut LN substrates using reactive rf magnetron sputtering in 2002 [8]. That work showed that the crystalline orientation of AlN layers was dependent on deposition conditions and had demonstrated the fabrication of AlN/LN based surface acoustic wave (SAW) devices. In the same year, the first high-quality III-nitride growth method on LN was developed using plasma-assist MBE (PAMBE) [1,2]. In the subsequent years, integrated AlGaN/GaN electronic drivers on the ferroelectric material LN crystals were implemented [3,4]. Furthermore, aluminum nitride (AlN) epitaxial layers were demonstrated to partially relieve temperature instability and increase surface acoustic wave (SAW) velocity compared to bulk LN (LT) SAW devices [5].

7.1 III-nitrides growth on lithium niobate and lithium tantalate

The performance of AlGaN/GaN-based devices can be improved by high-quality III-nitride materials. The crystal quality is affected by many growth conditions: substrate temperatures, III-V ratio, and pre-growth treatments, a nucleation layer, an III-V ratio, and the polarity of GaN films. The quality of earlier GaN films directly grown on sapphire has been very poor with high background electron concentration, in some cases, as high as 10^{20} cm⁻³, rough and uneven surfaces, and very broad x-ray rocking curves

[20]. However, the quality of GaN films has been improved substantially using a nucleation layer, called a buffer layer, grown prior to the growth of the active device layer. Amano *et al.* have achieved dramatically improved surface morphology of GaN films as well as electrical and optical properties by introducing a low-temperature AlN buffer layer [121,122]. The AlN buffer layer has resulted in the electron concentration below 10^{17}cm^{-3} and electron mobility of $600\text{ cm}^2/\text{Vs}$ at 300 K. Without the AlN buffer layer, the electron concentration has been increased to 10^{19}cm^{-3} and the electron mobility has been decreased to $50\text{ cm}^2/\text{Vs}$. Therefore, the AlN buffer layer could optimize a transition between substrates and GaN films, resulting in a high-density nucleation layer for the following epilayers, decoupled from the crystal arrangement of the substrate crystal structure.

The stoichiometry of GaN films has not been easily controlled because of the low solubility of nitrogen with Ga and the high vapor pressure of nitrogen over GaN films. However, these difficulties have been overcome by several advanced techniques: metal-organic chemical vapor deposition (MOCVD), metal-organic vapor phase epitaxy (MOVPE), and molecular beam epitaxy (MBE) process. The MOCVD and MOVPE have used a nitrogen molecule source supplied by cracking ammonia (NH_3) on the substrate surface at high temperatures ($> 1000\text{ }^\circ\text{C}$). Reactive MBE has used lower ammonia-cracking temperatures ($700 \sim 1000\text{ }^\circ\text{C}$) [20]. Furthermore, MBE has been equipped by ECR plasma or rf plasma to crack N_2 directly, leading to the most efficient nitrogen solubility with Ga and relatively low-growth temperatures ($500 \sim 1000^\circ\text{C}$) [21]. GaN films with a low III/V flux ratio (N-stable or N-rich condition) have shown faceted surface morphologies and tilted columnar structures with high density of stacking faults

and rough surface [123]. GaN films with a high III/V flux ratio (Ga-stable or Ga-rich condition) have shown smooth surface morphologies and the significant improvements of structural and electrical properties. The Ga-rich GaN films could be achieved by controlling Ga cell fluxes close to a value where Ga droplets have been formed and provided two-dimensional growth with the high surface mobility of Ga adatoms [123].

In most cases of MOCVD growth, smooth epitaxial films have Ga-polar GaN films on c-plane sapphire substrates grown in the (0001) direction. MBE growth has commonly occurred in the (000-1) direction, yielding N-faced films [124]. However, it is observed that the polarity of GaN films on sapphire can be controlled using an AlN buffer layer, which fully wets the surface of sapphire [125]. GaN films grown on the AlN buffer layer show 1nm surface roughness and a typical background electron concentration of $5 \times 10^{13} \sim 1 \times 10^{14} \text{ cm}^{-3}$, which are desirable for GaN-based HFET devices. This technique has been adapted to the AlGaN/GaN heterostructure growth, leading to the highest ever Hall mobility of 2019 cm^2/Vs with large 2DEG concentration of $1.3 \times 10^{13} \text{ cm}^{-2}$ at 300K, and 10250 cm^2/Vs below 10 K, grown by MOVPE on 6H-SiC in $\text{Al}_{0.2}\text{Ga}_{0.8}\text{N}/\text{GaN}$ heterostructures [126]. MBE grown $\text{Al}_{0.33}\text{Ga}_{0.67}\text{N}/\text{GaN}$ heterostructures on sapphire with an AlN buffer layer have shown the mobility of 974 cm^2/Vs with 2DEG concentration of $1.3 \times 10^{13} \text{ cm}^{-2}$ at 300 K, in which different nitridation schemes have been used to suppress inhomogeneous AlN+NO layers [127]. The mobility of $\text{Al}_{0.33}\text{Ga}_{0.67}\text{N}/\text{GaN}$ hetero-structures have been improved up to 1341 cm^2/Vs with 2DEG concentration of $1.6 \times 10^{13} \text{ cm}^{-2}$ by inserting a thin AlN layer between the AlGaN barrier layers and the GaN bulks. The thin AlN layer separates the channel from an AlGaN barrier, resulting in reduced alloy scattering [128]. Double buffer layers, consisting of low-temperature GaN

layers and high-temperature AlN layers, have been used to improve the mobility of AlGaN/GaN heterostructures, resulting in the highest mobility of 1587 cm²/Vs with 2DEG concentration of 1.25×10¹³ cm⁻² [127]. Therefore, this work proposes to use the AlGaN/GaN heterostructures in [127] as a target structure, which has the highest mobility of GaN films on sapphire substrates with AlN buffer layers using PAMBE, as shown in Figure 40.

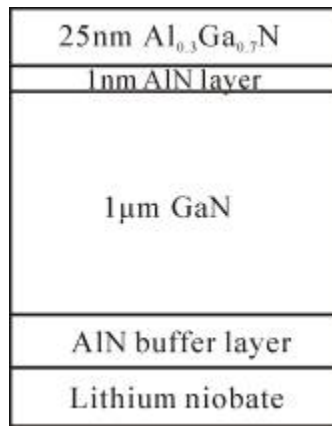


Figure 40: A target structure of AlGaN/AlN/GaN heterostructures with AlN buffer layers.

7.2 AlN buffer layer on lithium niobate and lithium tantalate

The mobility of AlGaN/GaN heterostructures is affected by the uniformity of polarity in GaN films. Non-uniform polarity causes potential differences between the AlGaN barrier and the GaN bulk, which block traveling electrons, as shown in Figure 41. The uniformity of polarity can be controlled using AlN nucleation layers [125]. AlN buffer layers [129] were grown at 600 °C for 100 nm thickness using a Veeco-Unibulb nitrogen source with 0.35 sccm nitrogen at the rf power of 350 watts. During the AlN buffer growth, reflection high-energy electron diffraction (RHEED) reconstructions were

observed with a streaky pattern, as shown in Figure 42(a). With increasing Al flux, a 2x2 reconstruction was observed. A further increase in Al flux resulted in a 1x1 RHEED pattern. A 2x2 reconstruction was reproducibly observed during cooling with exposure to an active nitrogen source. The 2x2 reconstruction implies that the AlN buffer layers have Al polarity, which guarantees Ga-polarity GaN [130].

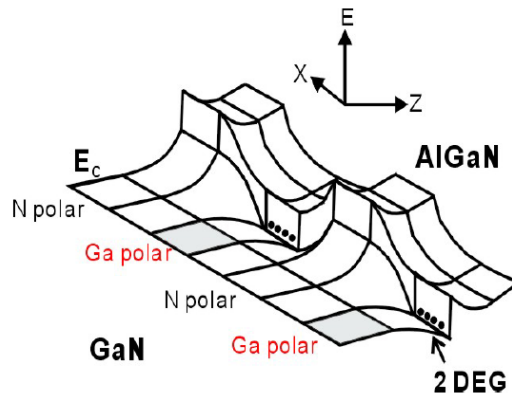


Figure 41: Demonstration of mixed polarity effects on electron mobility on a channel [127].

The mobility of AlGaIn/GaN heterostructures can be improved by having a smooth surface of GaN, which is affected by the roughness of prior AlN buffer layers. Thus, the AlN layers and GaN layers need to be smoothed using the shutter modulation method, which opens and closes each metal source shutter periodically [104]. The principle of the shutter modulation method is based on the behavior of the cation-anion reaction during epitaxial growths. Because cation atoms (gallium Ga^{3+} , aluminum Al^{3+}) are very reactive with anion atoms (nitrogen N^{3-}), the cation atoms have a longer surface diffusion length in the absence of the anion. The effect enhances surface migration for the cation atoms and improves material quality due to better epitaxial self-organization. The

shutter modulation method was applied for AlN buffer layers on sapphire, resulting in a smoother surface morphology, as shown in Figure 42(b) [131].

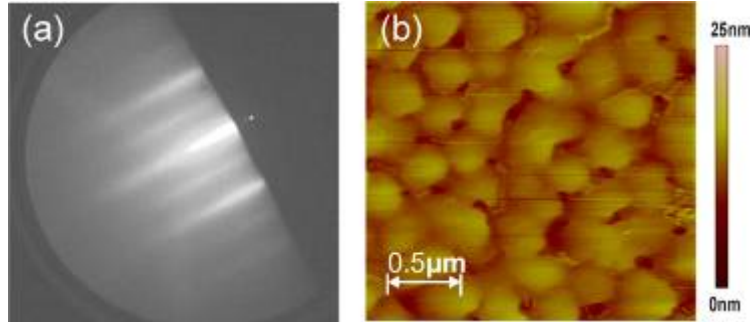


Figure 42: (a) RHEED reconstruction of AlN buffer layers on sapphire. The RHEED reconstruction implies the AlN buffer layers are Al polarity, which results in Ga-polar GaN layers and (b) surface morphology of AlN buffer layers with Al cell shutter modulation [127,131].

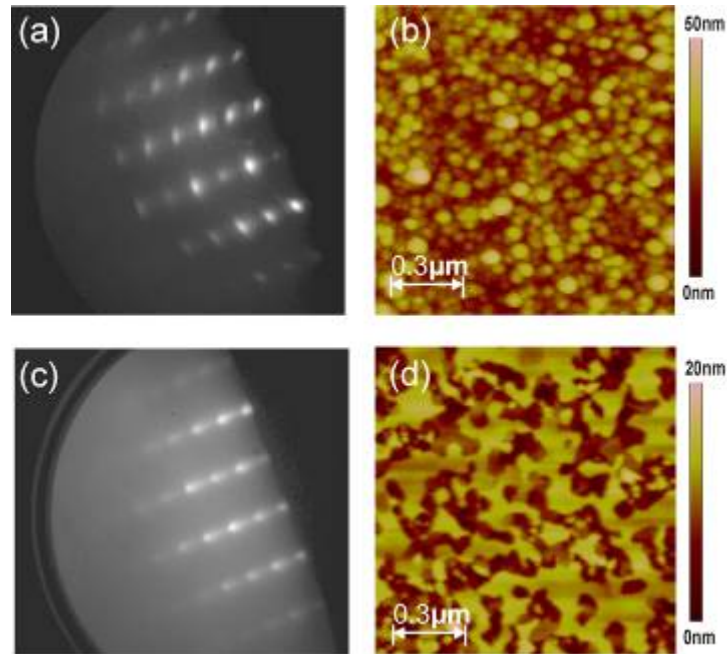


Figure 43: (a) Slightly amorphous RHEED pattern and (b) AFM surface morphology of AlN on LN at 800°C of substrate temperature; (c) spotty RHEED pattern and (d) AFM surface morphology with Al droplets at 600°C of substrate temperature with Al cell shutter modulation.

High-quality AlN nucleation layers on LN (LT) would be achieved by being grown at high substrate temperature (800 °C), which is the same growth temperature of AlN layers on sapphire. However, the high-temperature AlN layers on LN (LT) showed a slightly amorphous RHEED pattern and very grainy shape on the surface even with Al-rich condition, as shown in Figure 43(a) and Figure 43(b). This is because the in-diffusion of lithium from LN (LT) into the AlN layers makes an unexpected aluminum and lithium alloy, resulting in unexpected crystalline structure and rough surface. Therefore, it is necessary to grow the AlN layers at lower temperatures to minimize the in-diffusion of lithium from LN (LT). However, an AlN layer grown at the substrate temperature of 600°C still shows a rough surface morphology, indicating the existence of the unexpected aluminum and lithium alloy, as shown in Figure 43(c) and Figure 43(d).

7.3 AlGaN/GaN heterostructures on lithium niobate and tantalate

GaN films were grown on +z-LN (LT) substrates with AlN buffer layers, which were described in the previous section. The z+ direction of the substrates results in Ga-polar GaN films as dictated by the electrostatic boundary condition imposed by Gauss' Law. The GaN films were grown with two different temperature conditions, 650 °C for 300 nm of its thickness and 700 °C for the remaining 450 nm of thickness, both with 0.5 sccm nitrogen. A typical GaN layer grown on LN substrates is observed by AFM, shown in Figure 44(a), and has an approximate 1 μm grain size similar to other GaN films on various substrates. A shutter modulation method is also demonstrated for the improved intra-run uniformity of GaN films [104]. This method was applied for making a smoother GaN surface, as shown in Figure 44(b).

Figure 45(a)-(c) show x-ray diffraction (XRD) peaks of GaN films grown on LN and LT substrates by PAMBE. The GaN films have thicknesses of 0.5 - 1.0 μm and 0.7 μm for LN and LT, respectively. Both LN and LT substrates have (0002) GaN XRD peaks, which indicates that the growth direction of the epitaxial films is GaN [0001] || LN (LT) [0001]. The distinct difference of GaN growth on LN, rather than LT, is the formation of a second phase of (60-2) LiNb_3O_8 , indicated by a peak on the ω - 2θ scan at $2\theta = 38.1^\circ$, in addition to the original LiNbO_3 peak. This can be explained by the fact that congruent LN (48.39 mole% Li_2O) is metastable in vacuum and will decompose into the two phases of LiNb_3O_8 and Li_2O -rich LN at elevated growth temperatures [132]. As-received LN samples do not have any of the LiNb_3O_8 phase, so LiNb_3O_8 forms during outgassing of the substrate in the introduction chamber and during the growth [4]. Therefore, growth conditions of III-nitrides on LN must be carefully chosen to avoid the formation of the Li-deficient phase interfacial layer, LiNb_3O_8 , between the GaN films and LN substrates.

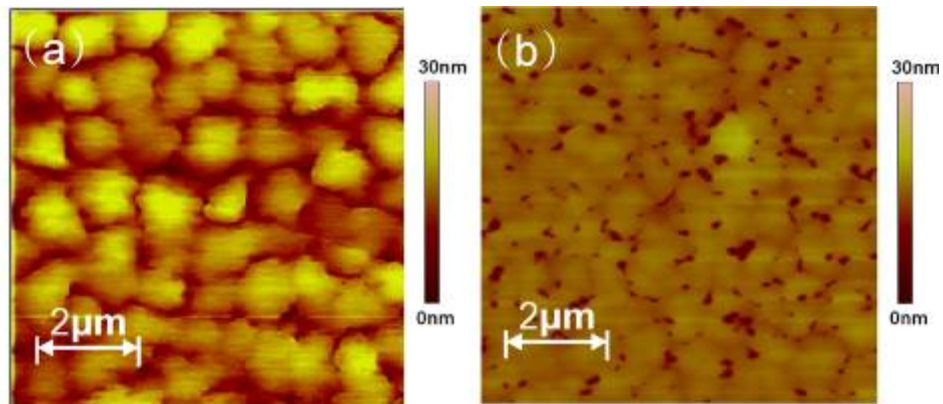


Figure 44: Surface morphologies of GaN films on LN by AFM (a) without Ga cell shutter modulation (b) with Ga cell shutter modulation.

To minimize the second phase of LiNb_3O_8 , a GaN buffer layer was grown at high temperatures (900 – 950 °C), where the congruent-melting composition in the two-phase field ($\text{Li}_2\text{O-Nb}_2\text{O}_5$) appears and the LiNbO_3 phase is stable [132]. XRD in Figure 45(b) indicates that the second phase of LiNb_3O_8 is reduced when the high temperature (900 – 950 °C) buffer layer is used, rather than the low temperature buffer layer at 500°C. For LT, the second phase is not observed with high resolution XRD, indicating that LT is more stable than LN at the growth temperatures.

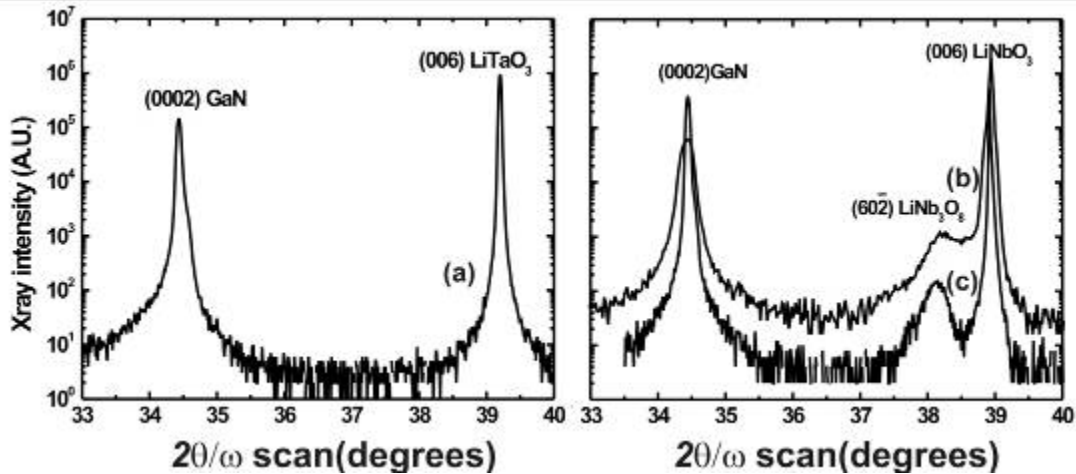


Figure 45: $2\theta/\omega$ x-ray scan of GaN films grown on LN and LT. (a) GaN films on LT, (b) GaN films grown on a high temperature (900 °C) GaN buffer layer, and (c) GaN grown on a low temperature (500 °C) GaN buffer layer.

Figure 46(a) shows the in-plane XRD peaks of the GaN layer on LN obtained by a rotational scan (ϕ -scan) about the c-axis of the (10-11) plane of the GaN epitaxial layer and the (11-23) plane of the LN (LT) substrate. This shows the in-plane relationship at the interface. The six respective peaks of GaN (10-11) and (11-23) planes indicate that the GaN layer has a hexagonal structure and is grown epitaxially on the LN (LT)

substrates, which also have a hexagonal structure. Furthermore, the ϕ -scan of GaN (10-10) was equivalent to that of LN (LT) (11-20), which implies that the hexagonal structure of GaN films is rotated 30° relative to the LN (LT) hexagonal structure. The selected area electron diffraction (SAED) pattern, with incident beam direction $z = [11\bar{2}0]$ GaN, shown in Figure 46(b), clearly suggests that GaN films grew epitaxially on the LN (LT) substrates.

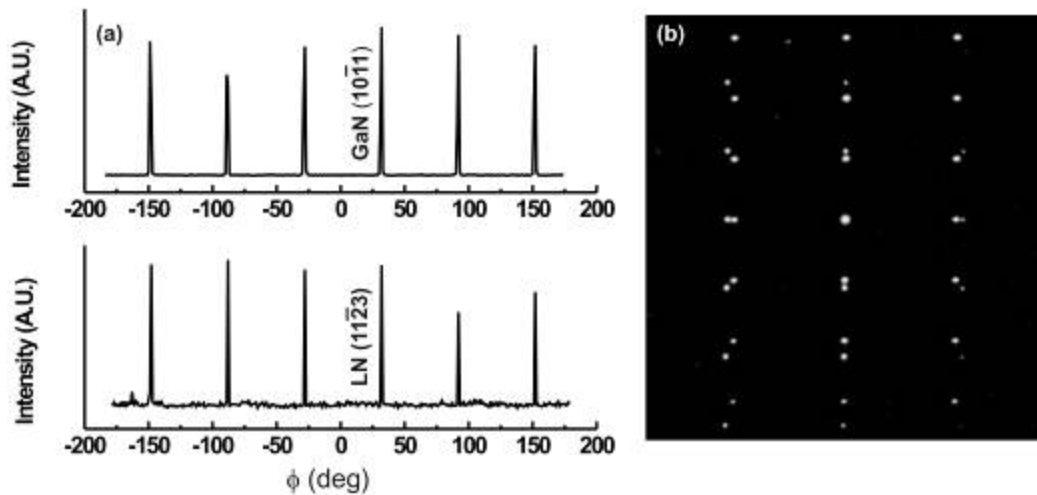


Figure 46: (a) ϕ scan of GaN films grown on LN substrates and (b) selected area electron diffraction (SAED) of the GaN films on LN substrates. GaN films are aligned with LN and LT after 30 degrees rotation.

AlGaIn/GaN heterostructures were also grown on furnace annealed CLN, SLN, and LT substrates under slightly N-rich followed by Ga-rich growth conditions. During the GaN layer growth, *in-situ* high-energy electron diffraction (RHEED) was monitored. Figure 47(a) shows the RHEED pattern of CLN at 200 °C, indicating smooth surface confirmed by AFM images. However, after increasing growth temperatures to 600~700 °C, a streaky RHEED pattern develops satellite peaks as shown in Figure 47(b),

indicating surface modification. Further growth of GaN films recovers the streaky RHEED pattern shown in Figure 47(c).

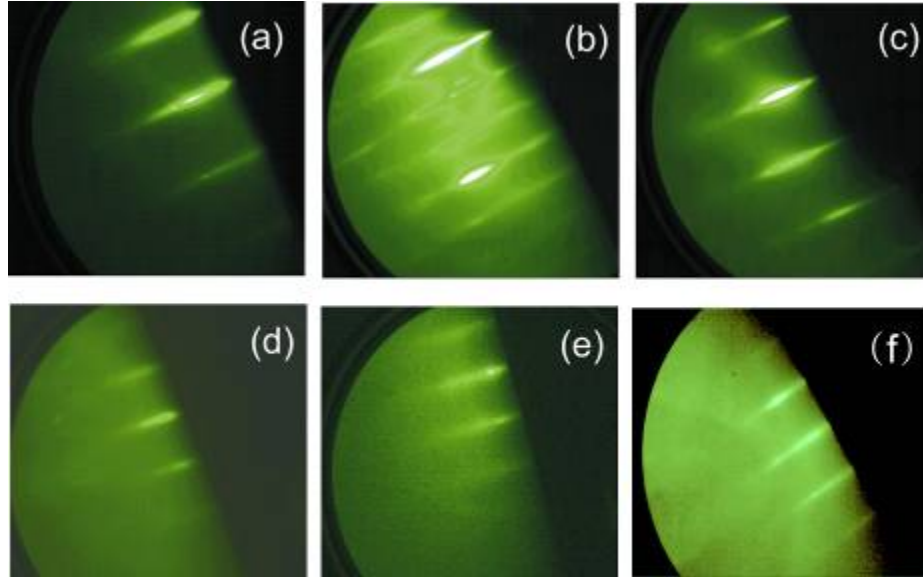


Figure 47: *in-situ* RHEED patterns on (a) CLN at 200°C, (b) CLN at 500°C~650°C, (c) GaN on CLN at 650°C, (d) SLN at 650°C, (e) GaN on SLN at 650°C, and (f) LT at 600°C.

On the other hand, SLN at the growth temperatures remain streaky, but dimmed pattern in Figure 47(d), indicating a stable but rough surface. The GaN layers on SLN show streaky RHEED pattern in Figure 47(e). LT at the substrate temperature of 600°C shows streaky RHEED patterns, indicating stable surface. These RHEED results confirm different surface stability among CLN, SLN, and LT substrates, performed by spectroscopic ellipsometry experiment at different temperatures.

Figure 48(a) shows RHEED pattern for GaN buffer layers on LN substrates at the substrate temperature of 500 °C. LN substrates prior to growth have a very streaky RHEED pattern, which indicates a smooth surface. RHEED patterns observed following GaN growth were changed to streaks and double spots, corresponding to the [111]-

oriented cubic GaN (c-GaN), indicating a mixture of hexagonal and cubic phases of GaN films [133]. The mixed cubic-hexagonal GaN phases develop into a single hexagonal phase of GaN films. A similar RHEED pattern was observed for GaN films on LT.

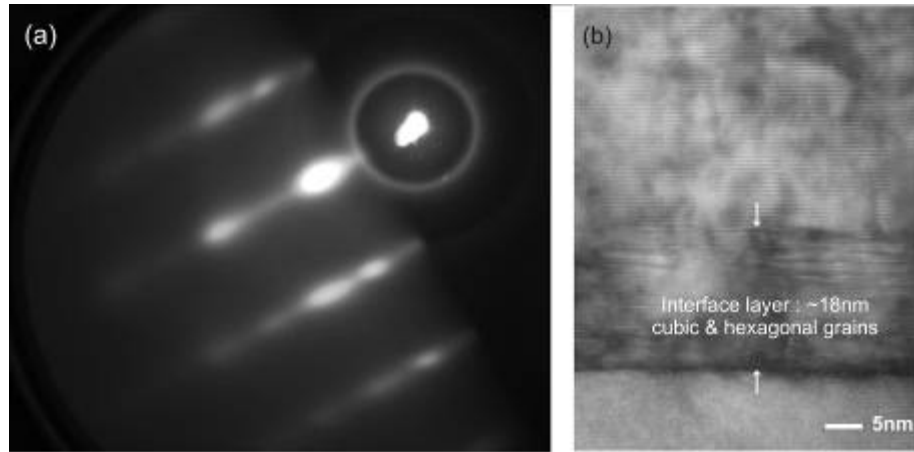


Figure 48: (a) GaN RHEED on LN showing a mixture of cubic and hexagonal phases viewed along the [11-20] azimuth and (b) GaN TEM image grown on LT showing a mixture of cubic and hexagonal phases.

Figure 48b shows the cross-sectional TEM images of GaN/LT interfaces. The high resolution images taken at the interface of GaN/LT indicate an approximately 18 nm thick interface region, which shows stacking faults with mixed phases of cubic and hexagonal GaN. The mixed phase of GaN is possibly related to oxygen on the surface of LT [134,135,136]. Cubic GaN has been observed in the local environment of oxygen [135,136] or oxygen-terminated surfaces in GaN [134], which cause stacking faults, as observed in TEM images. Stacking faults are the main types of extended defects occurring in an oxygen rich local environment, or oxygen-terminated surfaces. Yeh *et al.* have indicated that a slight difference in formation energies, approximately 10 meV atom^{-1} , is needed to create stacking sequences between cubic and hexagonal phases [137].

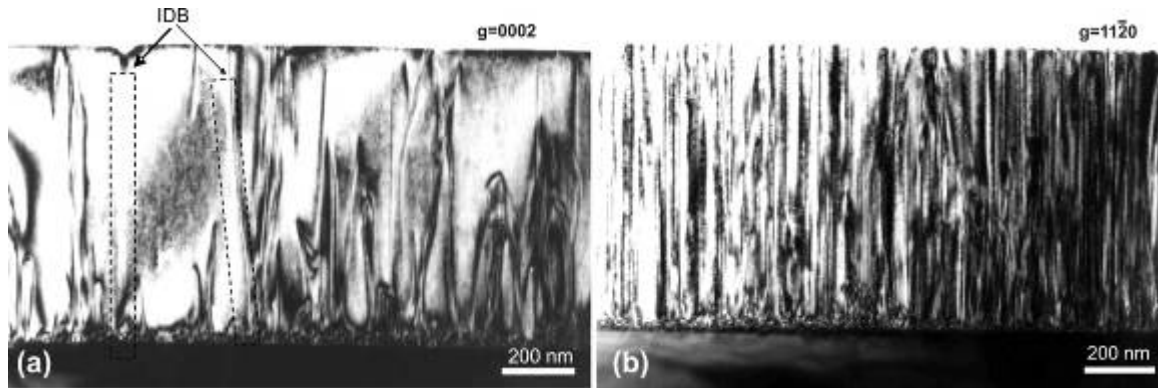


Figure 49: Cross-sectional TEM images of the GaN film grown on LT with (a) $g=0002$ and (b) $g = 11\bar{2}0$.

Furthermore, TEM images were used to analyze the structural quality and quantify the dislocation density of GaN films on LT substrates. Figure 49(a) and Figure 49(b) are TEM images under $g=0002$ and $g = 11\bar{2}0$ two-beam conditions, respectively. Under the $g=0002$ two-beam condition, pure screw and mixed dislocations are visible while pure edge and mixed dislocations can be observed under $g = 11\bar{2}0$ two-beam conditions [138]. Therefore, from Figure 49(a) and Figure 49(b), pure edge dislocations are dominant and estimated at more than 10^{10} cm^{-2} for GaN films grown on LT substrates. For GaN films on a LN substrate, TEM analysis shows the similar results. GaN films usually possess dislocation density typically in the range of $10^9 \sim 10^{10} \text{ cm}^{-2}$ due to the large lattice and thermal mismatches between sapphire or SiC and GaN films. LN and LT possess enormously large thermal expansion coefficients [80,139]. The values of in-plane thermal expansion coefficients of $\alpha_a=5.59$ and $7.5 \times 10^{-6} \text{ K}^{-1}$ for GaN and sapphire substrates [140] are considerably smaller than $\alpha_a=14.3$ and $16.1 \times 10^{-6} \text{ K}^{-1}$ for LN and LT [80], respectively. Therefore, the larger thermal expansion coefficients of LN/LT substrates give rise to a higher density of dislocations during cooling down from the

growth temperature even though they each have smaller lattice mismatches compared with that of sapphire and SiC substrates.

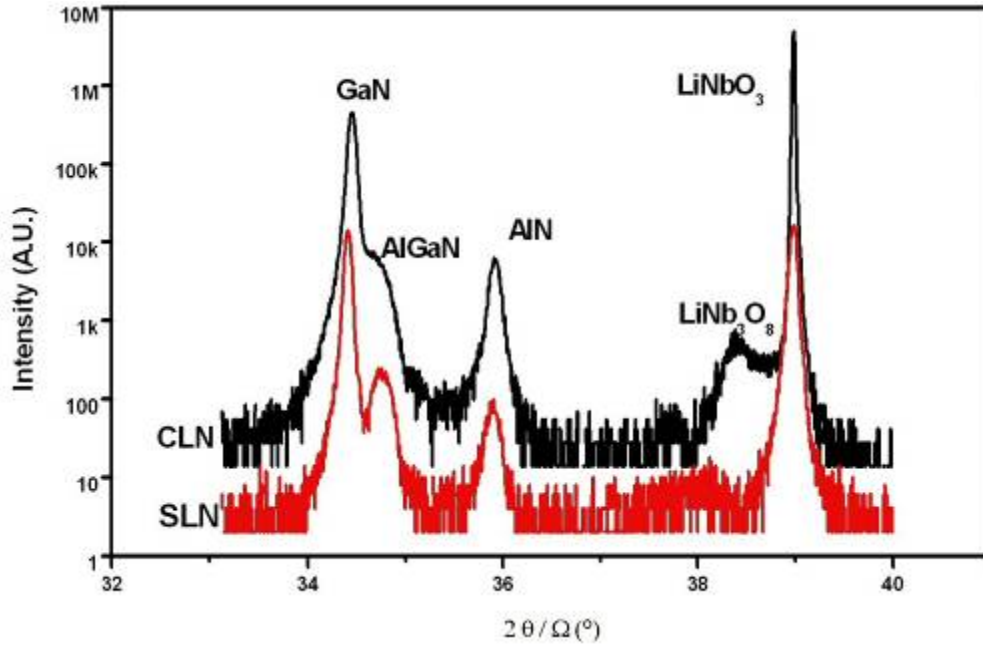


Figure 50: The x-ray diffraction 2θ - Ω spectra of HEMT structures: Upper - CLN, Lower - SLN showing that SLN has lower intensity of x-ray diffraction peak of LiNb_3O_8 .

The structural quality of AlGaIn/GaN heterostructures is assessed by 2θ - ω x-ray diffraction. As shown in Figure 50, the x-ray diffraction spectrum shows a well-oriented GaN film on CLN - upper graph - as well as the presence of a lithium triniobate, LiNb_3O_8 , surface layer. However, in the lower graph in Figure 50, SLN shows the lower peak intensity of the LiNb_3O_8 surface layer. The Al mole fraction of the $\text{Al}_x\text{Ga}_{1-x}\text{N}$ layer is estimated to be 20 % from the curve peak separation of the $\text{Al}_x\text{Ga}_{1-x}\text{N}$ and GaN layers. This heterostructure has an x-ray diffraction rocking curve, ω spectrum, for the GaN film of 1581 arcsec for (0002) FWHM and 1870 arcsec for (10-12) FWHM on CLN and 1601 arcsec for (0002) FWHM and 2076 arcsec for (10-12) FWHM on SLN, respectively.

Those broad FWHM values are partially due to initial GaN growths under nitrogen rich growth right after the AlN buffer layers growth to reduce the dislocation density [141], but also represent the relative immaturity of GaN films on LN substrates.

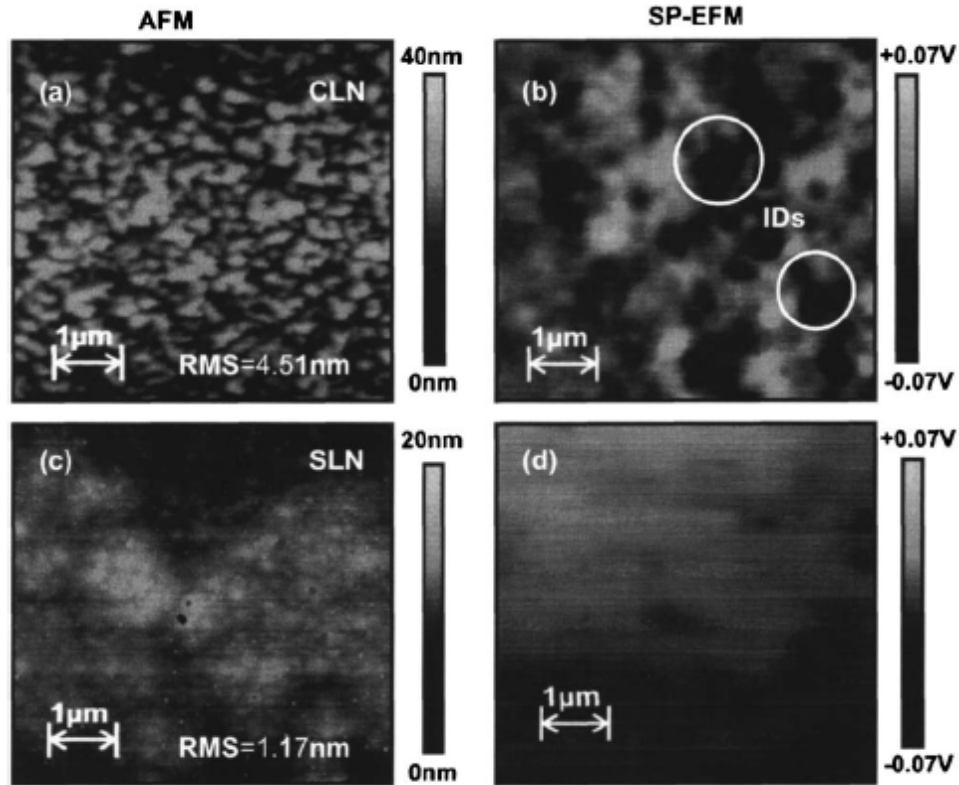


Figure 51: (a) Surface morphology and (b) the surface potential measurement of the AlGaIn/GaN on CLN substrates by AFM and surface potential EFM. (c) The surface morphology and (d) the surface potential of AlGaIn/GaN on SLN, indicating smoother surface and no inversion domains.

The electron transport properties in AlGaIn/GaN HFETs were measured by Hall effect measurement at room temperature. It showed the mobility of $\sim 380 \text{ cm}^2/\text{Vsec}$ with the sheet charge of $1.7 \times 10^{13} \text{ cm}^{-2}$ on CLN substrates and $\sim 780 \text{ cm}^2/\text{Vsec}$ with $7.7 \times 10^{12} \text{ cm}^{-2}$ on SLN substrates. The higher mobility on SLN can be explained due to improved surface roughness and a lower polarity inversion domain density. Figure 51 shows the

surface morphology and surface potential of AlGaN/GaN heterostructures on CLN and SLN via Kelvin probe microscopy (KPM) [129]. The surface of AlGaN/GaN heterostructures on SLN is much smoother than films grown on CLN substrates, indicating that the surface roughness after annealing at high temperatures does not affect but it is inferred that the surface stability is more crucial factor than the surface roughness. Furthermore, inversion domains were observed on CLN substrates while a few inversion domains, lower surface potential area, have been measured on SLN.

It is reported that a 0.25 μm gate Si-doped MODFET was operated at the cutoff frequency of 21.4 GHz and maximum frequency of 77.5 GHz with a mobility of $680 \text{ cm}^2/\text{Vsec}$ at $\sim 7.3 \times 10^{12} \text{ cm}^{-2}$ on sapphire [142]. These figures of merit thus imply the present results may already be suitable for the desired integrated devices for 10GHz modulators driven by AlGaN/GaN transistor amplifiers, although they are significantly less than similar structures grown on other mature substrate technologies. Future improvement can be expected as growth conditions are further optimized.

It is concluded that LN has been shown to be a viable substrate for the growth of GaN via MBE because of the structural similarity between GaN and LN. However, GaN growth on LN is challenging due to interfacial properties of surface segregation, delamination, and repolarization. Surface segregation and delamination problems can be relieved by furnace annealing. However, the furnace annealing at 1000 $^{\circ}\text{C}$ gives polarity inversion domains on the surface of CLN, which degrade the channel mobility of III-nitride devices. SLN is an alternative solution to minimize inversion domain formation and shows stable crystalline behavior, resulting in two times improved electrical channel

mobility in AlGaN/GaN heterojunction structures. Future efforts will address improved crystalline quality and demonstrating optical modulation from integrated optoelectronic structures.

CHAPTER 8: RESISTIVITY CONTROL ON III-NITRIDES

An extensive part of this research has focused on increasing the resistivity of GaN films, specifically grown on LN and LT. Highly resistive GaN films are critically needed in the high-frequency operation of GaN-based high electron mobility transistor (HEMT) devices to avoid parallel conductivity pathways through the GaN bulk layers. Highly resistive GaN films, therefore, enhance the device pinch-off. In this chapter, the conductivity of GaN films on lithium niobate (LN) and lithium tantalate (LT) is investigated. Compared to the case of GaN films on sapphire substrates, the GaN films on LN and LT show a highly conductive property. According to Chapter 6, the GaN films were conductive because of the impurity out-diffusion from the ferroelectric substrate materials. Therefore, this chapter investigates various ways to suppress the out-diffusion from the substrates.

8.1 Review of resistivity control on undoped GaN films

The resistivity of GaN films could be increased by adding acceptor doping (Fe, Mg, Zn) [143]. This method, however, was not appropriate for applying to HEMT devices because the added acceptors reduced the material mobility by introducing additional scattering centers and exact compensation of donor by acceptors requires prior knowledge of the number of residual donors which is not known. The resistivity of GaN was also controlled using different carrier gases during the nucleation layer deposition [144] and using different source gas pressures [145] in MOCVD systems. These experiments revealed that the resistivity of GaN is closely related to the threading

dislocations and grain boundary size. These two factors are inversely proportional to each other. The dislocation-related defects contribute to scattering, trapping, and compensating centers in the conducting regions in GaN films. Thus, screw dislocations act as one of the conductive paths, thereby increasing the electrical conductivity of GaN films along vertical directions as observed by the ballistic electron emission microscopy (BEEM) [146]. As the opposite of the screw dislocations, the edge dislocation density is inversely proportional to the resistivity of GaN films. Therefore, as the edge dislocation density is increased and the screw dislocation density is decreased, it is possible to grow highly resistive GaN layers [144]. The dislocation density of GaN films on sapphire substrates has been varied from 10^8 to 10^{10} cm^{-2} , depending on the growth process conditions. A recent commercial GaN-based HEMT structure on sapphire substrates by MOVPE shows an average sheet resistance of $431.2\Omega/\square$, electron concentration of low 10^{15} cm^{-3} , average mobility of $1100\text{cm}^2/\text{Vs}$, and average sheet charge of 1.19×10^{13} cm^{-3} [147].

Commercially available GaN films on sapphire normally have AlN buffer layers between the films and the substrates. The AlN buffer layers are distinguishable, by observing the bright area of a scanning electron microscopy (SEM) cross-sectional image, as shown in Figure 52(a) [148]. The brightest region, called a transition region, in the image indicates the high intensity of electron charging in the SEM. This is because electrons are collected and accumulated in an insulator region. Therefore, GaN films on sapphire have a transition region that is highly resistive. In contrast, the brightness of GaN films is less than that of AlN layers, indicating less resistive GaN films. As a comparison, columnar-shaped GaN films grown on lithium niobate (LN) (sample number: N2422) had an indistinguishable narrow transition region in the SEM image

shown in Figure 52(b). This observation indicates that the GaN films grown on ferroelectric materials are highly conductive.

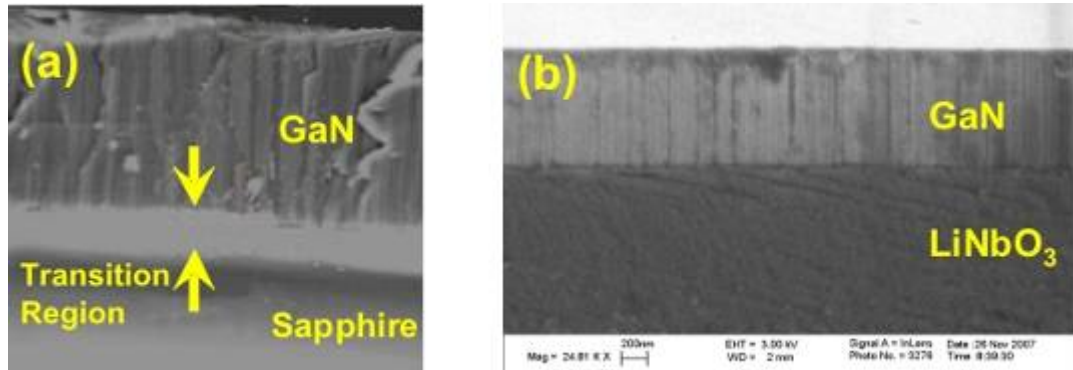


Figure 52: SEM cross-sectional image of (a) the GaN/Al₂O₃ interface with transition region [148], (b) GaN/LiNbO₃ interface (sample number: N2422).

8.2 Low-temperature growth scheme and super-lattice layers

Research reported an out-diffusion problem when growing GaN films on ZnO substrates [149]. The degree of out-diffusion at the GaN/ZnO heterointerface was estimated using the glancing incidence x-ray reflectivity (GIXR) technique. GIXR reveals the thickness, interfacial roughness, and density of interfacial layers by comparing x-ray reflectivity and theoretical information from the Fresnel equation [150,151,152]. An example of the GIXR technique is shown in the inset in Figure 53. This inset of the GIXR simulation, shows the fitting between measured data and theoretical simulation for a GaN/ZnO sample grown at 500 °C. The measurement indicates that there is no interfacial layer at the interface of the sample. The thickness variation of the interfacial layer as a function of growth temperature is shown in Figure 53 [149]. The thickness of the interfacial layer increased with the increase of growth

temperature above 500 °C. Therefore, GaN films on ZnO substrates need to be grown at low temperatures to suppress the impurity out-diffusion.

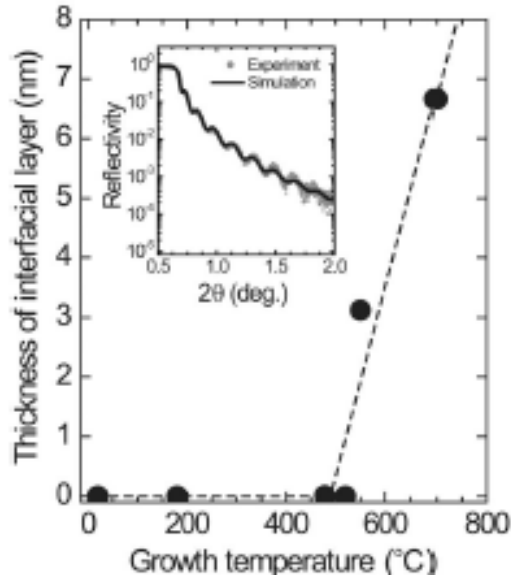


Figure 53: The dependency of interfacial-layer thickness is shown in the function of growth temperatures. An inset figure shows the GIXR curve of a GaN/ZnO sample grown at 500°C [149].

To suppress the impurity out-diffusion, super-lattice layers were applied in GaN films grown on an LiGaO₂ substrate [153]. The super-lattice layers are composed of the periodically alternative AlN and GaN layers. Secondary ion mass spectroscopy (SIMS) profiles show that the Al-containing layer effectively suppresses the lithium out-diffusion from the LiGaO₂ substrate during GaN growth. Therefore, in the following section, the low-temperature growth scheme with the super-lattice layers is applied to growing GaN films on ferroelectric materials for suppressing the impurity problem.

8.3 GaN growth at low temperatures with super-lattice layers

Several GaN films were grown to investigate the effects of the low-temperature buffer with the super-lattice layers. Since the growth temperature is very important for suppressing the out-diffusion from substrates as concluded in the previous section, various growth temperatures were used to investigate.

Before growing the GaN layers, LN or LT samples were pretreated to overcome the practical difficulties mentioned in Chapters 5 and 7. The LN or LT samples were annealed at 500 °C or 1000 °C in dry air and outgassed at 200 °C, 500 °C, or 700 °C in a vacuum environment. Then, super-lattice or GaN or AlN nucleation layers were grown on the pretreated LN or LT samples at various temperatures. The super-lattice layers were made of five periodic layers of AlN and GaN with two different time periods: the thickness of each AlN or GaN is ~ 10nm and ~ 50nm, respectively. AlN or AlGaIn buffer layers were followed with about 100nm thickness to control polarity. Finally, GaN bulk layers were grown at several different temperatures with about a 900nm thickness by Ga-rich conditions. The summary of the growth conditions is shown in Table 5.

AlN layers were grown with super-lattice nucleation layers in sample N2408 to investigate conductivity. The AlN layers had relatively low resistivity compared to AlN layers grown on sapphire, which is normally an insulator. After growing GaN layers on top of the AlN buffer layers (N2409), the resistivity of GaN became lower, indicating the effect of continuous out-diffusion from the substrates during growth. As shown in Table 5, the GaN films grown on LN are highly conductive compared to GaN films grown on sapphire, which have the resistivity of the low $10^{+11} \Omega/\square$ range.

Table 5: GaN growth at low temperatures with several buffer layers on lithium niobate: FA: furnace anneals, VA: vacuum anneals, SL: super-lattice, AL: GaN/AlN alternating layers, R: resistivity, and FWHM: full width of half maximum of GaN x-ray diffraction on (0002) Ω -scan.

| Sample # | Pre-treat FA/VA(°C) | SL (°C) | AlN (°C) | GaN (°C) | R(Ω/\square) | FWHM(") |
|----------|------------------------|-------------|-------------|----------|-----------------------|---------|
| N2408 | 500/200 | 500+GaN 500 | 650 | None | 6.2E+6 | N/A |
| N2409 | 500/200 | 500+GaN 500 | 650 | 650 | 1.2E+3 | 1496 |
| N2427 | 500/200 | 600 | 600 | 600 | 2.1E+3 | 1078 |
| N2430 | 500/700 | None | 600 | 600 | 1.1E+3 | 2432 |
| N2422 | 500/200 | None | 200 | 475 | 4.2E+8 | 3107 |
| N2485 | 500/700 | AL200 | 500 | 600 | 2.6E+7 | 2700 |
| N2488 | 1000/700 | AL 200 | 500 | 600 | 1.6E+9 | 3046 |
| N2453 | 500/500 | 475+GaN 475 | AlGaIn 475 | 500 | 9.6E+6 | 1381 |
| N2454 | 500/500 | 475+GaN 475 | AlGaIn 475 | 475 | 9.1E+6 | 1468 |
| N2465 | 500/500 | 600 | 650 (200nm) | 600 | 8.7E+2 | 1586 |
| N2466 | 500/700 | 600 | 650 (200nm) | 600 | 4.7E+4 | 1415 |
| N2489 | 500/700 | GaN 200 | None | 600 | 4.3E+3 | 1976 |
| N2505 | 1000/200 | InN 385 | InGaIn 385 | 475 | 3.1E+3 | 1870 |

In sample N2427, the resistivity of the GaN films is increased slightly by lowering GaN growth temperatures, implying less out-diffusion from the substrates. Sample N2427 has higher crystal quality compared to the N2409, confirmed by x-ray diffraction. Note that the GaN films were grown on both the z-axis and x-axis of LN simultaneously, observed by cross-sectional SEM, as shown in Figure 55. The growth of both sides could be possible because the substrate was thick enough (~1mm) to grow very thin GaN films (~10nm) on the side walls. The films on the side walls (x-axis), however, became conductive paths from the GaN films on +z-axis to metal-coatings on -

z-axis. Therefore, isolation patterns were required to measure the resistivity of the GaN films grown on the +z-axis of LN substrates.

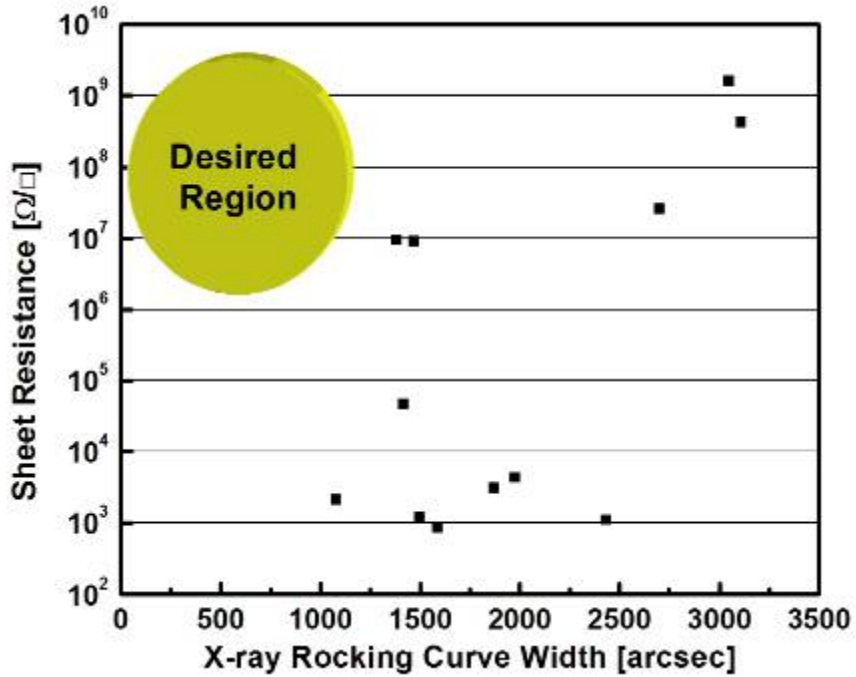


Figure 54: Rocking curve vs. Sheet resistance variation for the different processes described in Table 5. Note the clustering of samples around 1000 ohms/square and the only two samples approaching the desired region containing AlGaIn buffers.

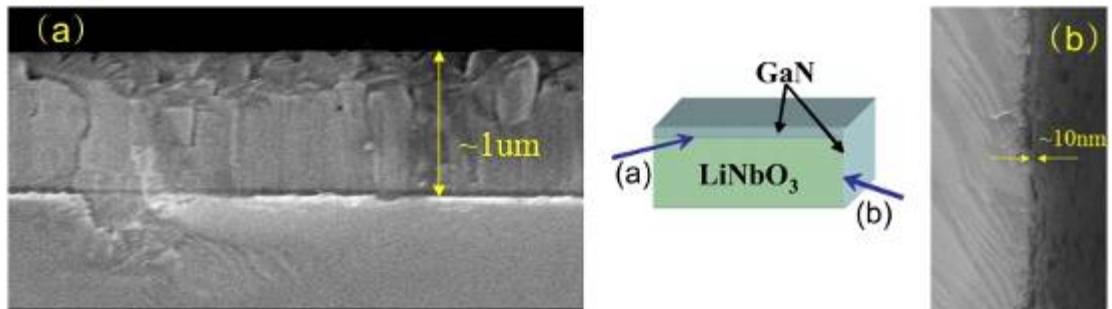


Figure 55: SEM cross-sectional image of N2427 sample: (a) III-nitrides grown on z axis with $\sim 1\mu\text{m}$ thickness (b) III-nitrides grown on x-axis with $\sim 10\text{nm}$ thickness. An inserted cartoon in the middle illustrates the direction of the SEM images.

The effect of using a super-lattice (SL) was investigated in the sample N2430. The GaN films without SL layers show the highest conductivity and worse crystal quality. The SEM cross-sectional image of the N2430 sample shows a very deep level of inter-diffusion patterns, spike-like shapes penetrating ~20 μm into the substrate as shown in Figure 56 (a). A smaller scaled image is shown in Figure 56 (b), which shows no obvious barrier between the films and the substrate. This is probably caused by an interaction between aluminum from the AlN layers and lithium from the substrate at the heterointerface. It is proven that higher outgassing temperatures can improve the resistivity and crystal quality of GaN films in the N2465 and N2466 cases. As a result, the degradation of resistivity and crystal quality in N2430 result from the absence of super-lattice layers. Therefore, it is concluded that SL layers could partially minimize the out-diffusion and suppress spike-like shapes at the interface, resulting in improved resistivity and crystal quality of GaN films.

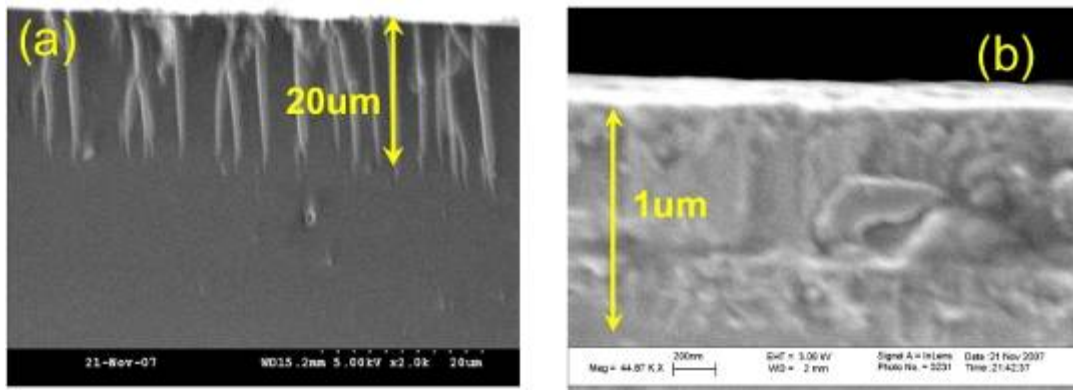


Figure 56: SEM cross-sectional image of N2430 sample (a) large scaled image with spike-like shapes (b) smaller scaled image of GaN/AlN films with intermixed layers

The effect of low-temperature growth is investigated in N2422. The low-temperature AlN and GaN layers were grown at 200 $^{\circ}\text{C}$ and 475 $^{\circ}\text{C}$, respectively. The

SEM cross-sectional image of the sample is shown in Figure 52. The image shows no transition region, but has a brighter region on GaN films than the substrate, indicating the high-resistive GaN films. However, the crystal quality of the sample is very poor. These results indicate the low-temperature AlN layers act as a very efficient out-diffusion blocker, but provide poor nucleation layers at the same time.

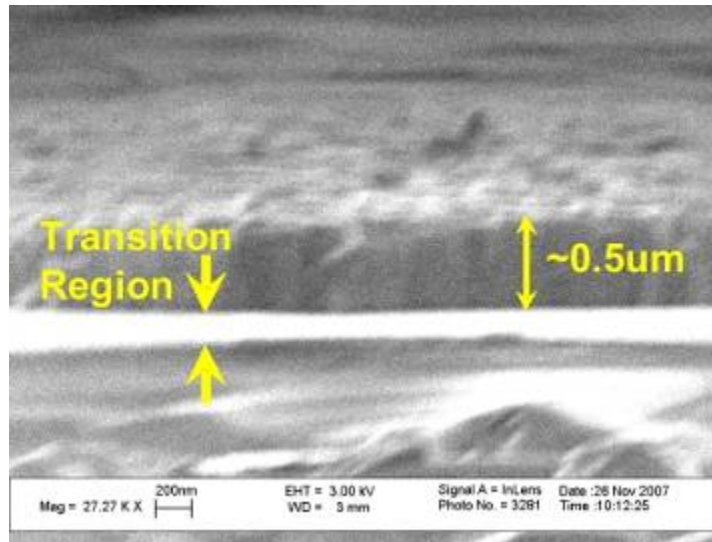


Figure 57: SEM cross-sectional image of N2488 with bright barriers (transition region), indicating insulation property at the interface, but rough surface morphology

The low-temperature AlN layers are applied for modifying the super-lattice layers in the N2485 and N2488 samples. The modified super-lattice layers have a growth time five times longer than alternatives of GaN and AlN at 200 °C. After using the modified SL and growing GaN films at 600 °C, the N2485 sample has improved crystal quality, but lower resistivity. The resistivity was improved using 1000 °C furnace annealed samples in N2488 with slightly worse crystal quality. The SEM cross-section image of the N2488 sample shows a very bright barrier at the interface between III-nitrides and the substrate, indicating insulation property, as shown in Figure 57. The N2488 sample has

the highest resistivity. However, the image shows rough surface morphology because of poor nucleation layers. It is concluded that the low-temperature SL or AlN layers are efficient out-diffusion blockers because the chemical interaction is minimized at low temperatures, but they provide poor crystal quality.

Instead of AlN buffer layers, AlGaN layers were grown as buffer layers in N2453 and N2454 samples to investigate the resistivity and crystal quality. These AlGaN layers had a 30% Al composition and are expected to be more easily formed at lower growth temperatures than those of AlN layers. GaN films were grown on top of the AlGaN layers with Ga-droplets. As a result, the GaN films on the AlGaN layers have higher resistivity and reasonable crystal quality. Even though the GaN films were grown under Ga-rich conditions, they have facet surface morphology, confirmed by spotty and streaky RHEED patterns, as shown in Figure 58(a). This is because aluminum, gallium, and nitrogen atoms might not have enough surface mobility at the low temperatures. This approach needs to be modified to improve the surface roughness but in general offers the best alternative for future research of all buffer layers tried in Table 5.

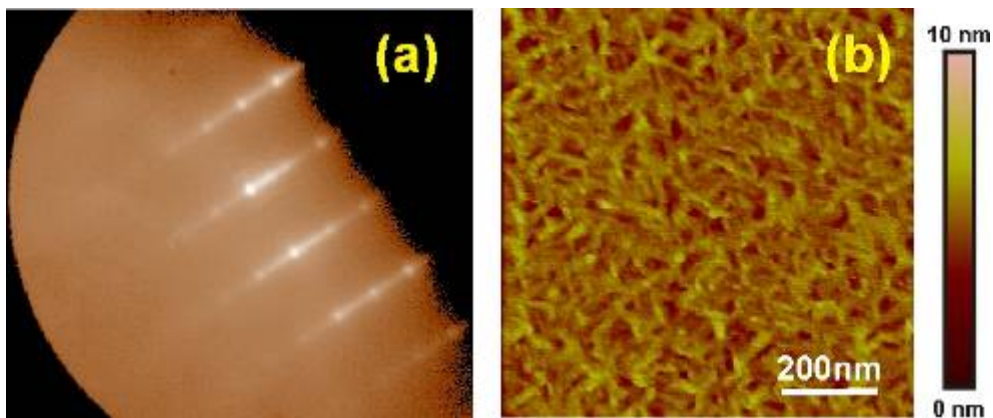


Figure 58: (a) Spotty and streaky RHEED pattern of N2453 sample with AlGaN buffer layers (b) AFM surface morphology of the out-gassed LiNbO₃ at 800 °C for 30min with porous shapes.

The effects of vacuum annealing or outgassing were investigated in the samples N2465 and N2466. These samples had the same growth conditions, with thicker AlN layers (~200nm) at 650 °C, except for different vacuum annealing temperatures. Both samples showed reasonable crystal quality, but lower resistivity because of the high growth temperatures. Therefore, higher resistivity with higher outgassing temperature implies that impurities may be expelled more with higher outgassing temperatures.

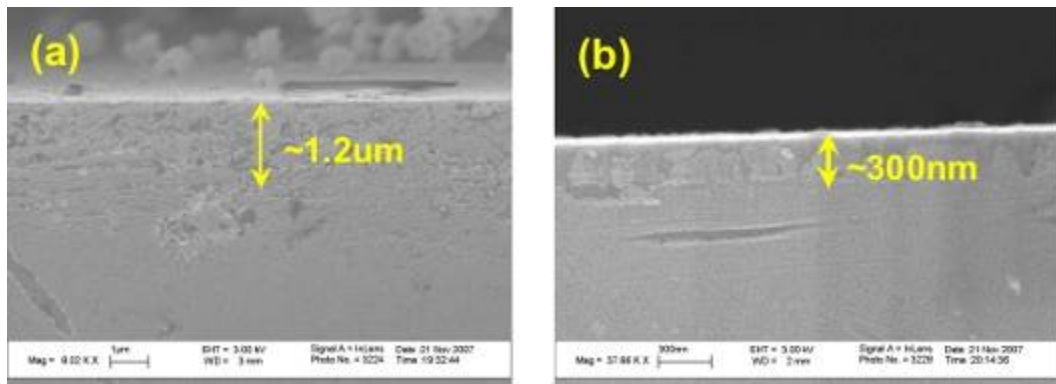


Figure 59: SEM cross-section of (a) N2489 sample with low-temperature GaN buffer layers grown at 200 °C with unexpected 1.2 μm thick films (b) N2505 sample with InN and InGaN buffer layers.

The effects of GaN buffer layers (N2489) and InGaN buffer layers (N2505) without SL layers were investigated as alternative buffer layers. The GaN buffer layers were grown at 200 °C. The InGaN buffer layers were grown with compositions graded to 30% of gallium at 375 °C. GaN films grown on both buffer layers were highly conductive. The SEM cross-sectional images of the samples show no obvious barriers between films and substrates, as shown in Figure 59. The target thickness of GaN films with GaN buffer layers in N2489 was 1 μm thick. However, the total thickness of the films observed by SEM was about 1.2 μm , indicating a deep interfacial region because of

significant out-diffusion from the substrates. The thickness behaviors are the same in the N2505 sample. Therefore, both GaN and InGaN buffer layers are inefficient for blocking the out-diffusion from substrates during growth.

In conclusion, this section discusses several important points for low-temperature growth with SL layers: First, AlN buffer layers are efficient for blocking the out-diffusion from substrates. Second, lower growth temperatures reduce out-diffusion. Third, isolation patterns are required to measure the resistivity of GaN films grown on 1mm-thick LN samples because of extraneous leakage paths. Fourth, SL layers could partially minimize the out-diffusion and suppress spike-like shapes at the interface. Fifth, outgassing at high temperatures produced so many defects that while the resistivity improved, the crystal quality was so poor that use in a HEMT was impossible. Finally, only the use of AlGaN SL showed promise for future research. However, it was not clear as to why the surface quality of these layers was so highly degraded and had such unusual morphology.

8.4 GaN growth with lithium alloyed buffer layers

Another buffer layer synthesis method is to make a lithium-aluminum alloyed buffer (LAAB) layers. The alloyed layers are made by depositing aluminum on LN substrates at high temperatures without a nitrogen source. The purpose of this method is to trap the out-diffusing lithium oxides by the LAAB layers before growing the GaN bulk layers. The buffer layer formed a $2\times$ reconstruction RHEED patterns when aluminum was deposited on LiNbO₃ at high temperatures, as shown in Figure 60 (a) and (b). The N2419 and N2420 samples are synthesized at 650 °C and 800 °C for 5 minutes,

respectively. The $2\times$ reconstruction RHEED patterns may result from the overlapping of two different reconstruction patterns of the aluminum alloys and the LN substrate and thus is not an indicator of good surface quality as one would normally imply. The surface morphology of the LAAB layers is shown in Figure 60 (c) with pits and possible coalescence of aluminum and lithium elements. The x-ray diffraction spectra of the N2420 sample in Figure 61 (a) shows distinct phase separation of LiNbO_3 and Al + Li related alloyed peaks since a large amount of lithium oxides was pulled out from the LiNbO_3 substrate during the synthesis.

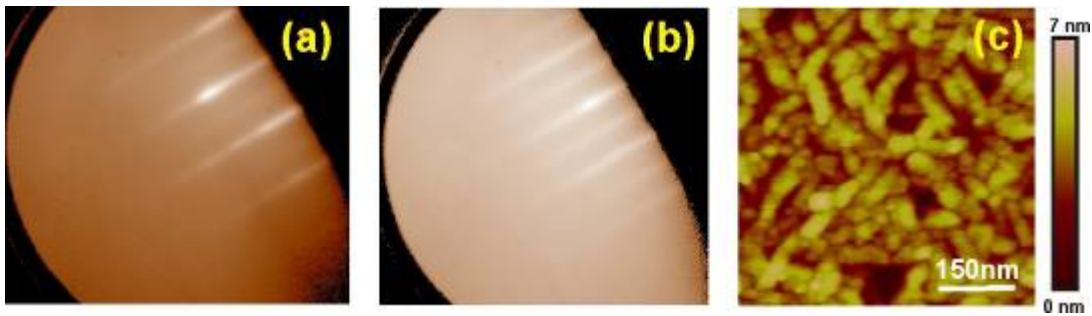


Figure 60: RHEED images of aluminum deposition on LiNbO_3 at the substrate temperature of (a) 650 °C in N2419 (b) 800 °C in N2420 and (c) AFM surface morphology of LAAB layers synthesized at 800 °C in N2420.

LAAB layers with 650 °C and 800 °C were grown on LN substrates in N2419 and N2420 samples, respectively. Then GaN films were grown with AlN, SL, and/or GaN buffer layers on top of the LAAB layers. A summary of the growth conditions is shown in Table 6. The LAAB layers have high resistivity values but in general, poor crystal quality. The N2421 sample has GaN films with AlN buffer layers on top of the LAAB layers. The resistivity of the N2421 sample is reduced compared to that of N2420, indicating the existence of in-diffusion into GaN films. The sample has reasonable crystal

quality. Figure 62(a) shows very rough surface morphology with rms roughness of 10.4nm observed by AFM. The GaN and AlN diffractions are distinguishable in $2\theta/\omega$ spectra as shown in Figure 61 (b). N2487 and N2457 have AlN and GaN buffer layers with slightly different growth conditions, respectively, but show huge differences in resistivity. This indicates that the AlN buffer layers are more efficient than GaN buffer layers in blocking the out-diffusion. GaN films in N2487 have improved resistivity because of SL and thick LAAB layers, but show worse crystal quality.

Table 6: GaN films growth on lithium-aluminum alloy buffer layers: FA: furnace anneals, VA: vacuum anneals, SL: super-lattice, R: resistivity, and FWHM: full width of half maximum of GaN x-ray diffraction on (0002) Ω -scan.

| Sample # | Pre-treat FA/VA(°C) | Al deposit at (°C) / min | AlN (°C) | GaN (°C) | R(Ω/\square) | FWHM(") |
|----------|---------------------|--------------------------|-----------|----------|-----------------------|---------|
| N2419 | 500/200 | 650/5min | None | None | 9.6E+7 | N/A |
| N2420 | 500/200 | 800/5min | None | None | 6.1E+7 | N/A |
| N2421 | 500/200 | 800/5min | 650 | 650 | 1.4E+6 | 1251 |
| N2487 | 500/200 | 650/20min | 650+SL575 | 600 | 2.1E+7 | 2042 |
| N2457 | 500/200 | 650/20min | GaN+SL575 | 575 | 4.7E+4 | 2904 |
| N2486 | 1000/200 | 800/20min | 650 | 600 | 3.1E+6 | 3125 |
| N2506 | 1000/200 | Ga 800/20min | 650 | 600 | 2.9E+4 | 3140 |

GaN films in N2457 were grown at 575 °C with GaN buffer and SL layers, resulting in higher conductivity and worse crystal quality. The higher conductivity can be explained by the absence of AlN layers as mentioned in a previous section. The N2457 sample has a smoother surface than that of N2421, observed by AFM as shown in Figure 62. The N2457 sample shows less phase separation between LiNbO₃ and Al + Li related

alloy peaks because of a lower LAAB deposition temperature, as shown in Figure 61 (c). The N2486 sample was grown with a growth condition similar to that of N2421 except for a higher furnace annealing temperature, resulting in higher resistivity and worse crystal quality. Note that the GaN crystal quality becomes worse as Al deposition time increases, as observed in the N2487, N2457, and N2486 samples. This is because the surface of these samples becomes rougher as Al deposition time increases, as shown in Figure 58(b) and Figure 60 (c).

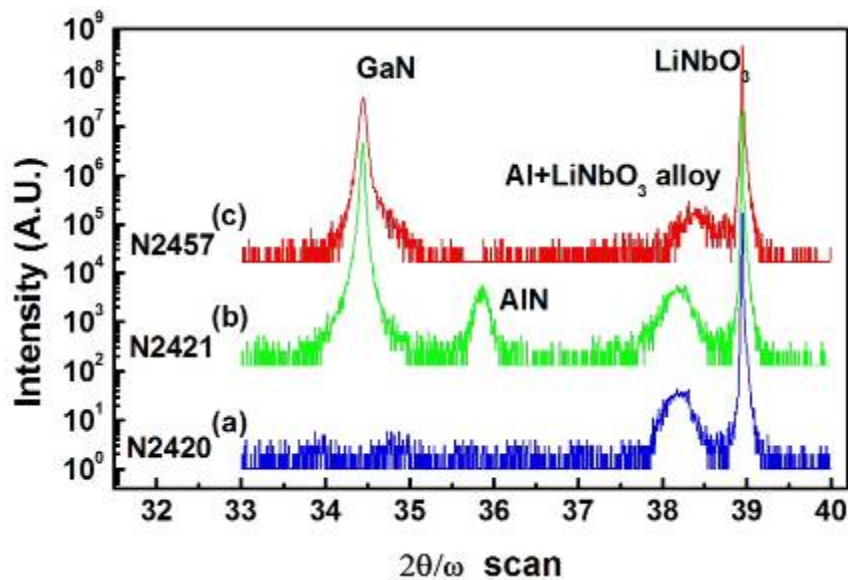


Figure 61: X-ray diffraction $2\theta/\omega$ spectra of (a) the LAAB layers synthesized at 800 °C on LN in N2420, (b) GaN films with AlN buffers on the LAAB/LN in N2421, and (c) GaN films with GaN buffers on LAAB layers synthesized at 650 °C on LN in N2457.

Additionally, lithium-gallium alloy buffer (LGAB) layers were synthesized to investigate the blocking effect of impurity out-diffusion from LN substrates. GaN films grown on the LGAB layers show high conductivity and poor crystal quality, indicating that LGAB layers are not efficient at blocking the out-diffusion from LN substrates.

Figure 63 shows the x-ray diffraction $2\theta/\omega$ spectra of the N2506 sample, which has five different diffraction peaks of GaN, AlN, Ga + Li related alloy, LiNb_3O_8 , and LiNbO_3 .

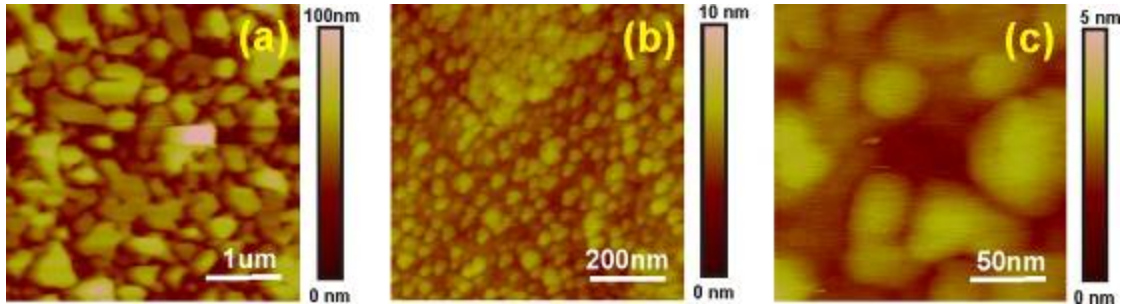


Figure 62: AFM surface morphologies of (a) GaN films of N2421 (b) GaN films of N2457 in $1\mu\text{m}\times 1\mu\text{m}$ scale (c) $200\text{nm}\times 200\text{nm}$ scale.

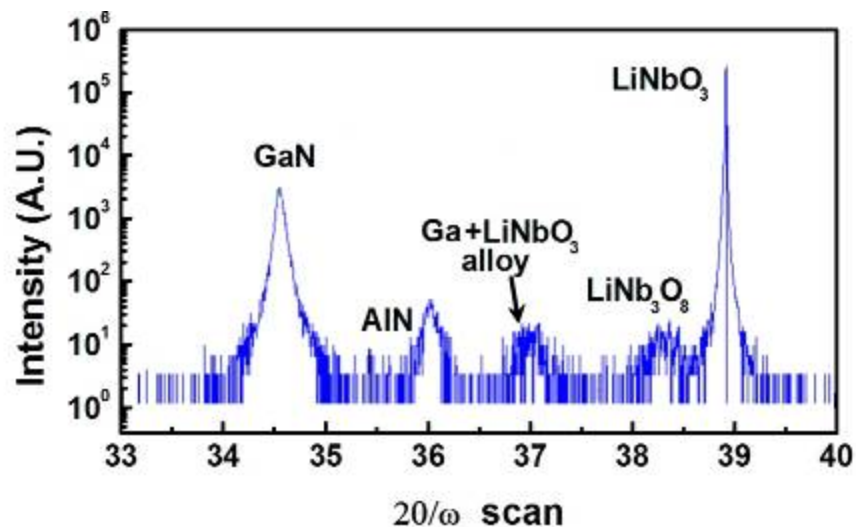


Figure 63: X-ray diffraction $2\theta/\omega$ spectra of GaN films with AlN buffer layers grown on LGAB/ LiNbO_3 in N2506 sample.

In conclusion, the Al or Ga + Li related alloyed buffer layers provide several features: First, the crystal quality of GaN films with LAAB layers becomes worse as Al deposition time increases. Second, LAAB layers roughen the surface of the substrates, resulting in the poor surface morphology of subsequent layers. Third, furnace annealing

at higher temperatures can improve the resistivity of GaN films. Finally, LGAB buffer layers are not efficient buffers for blocking the impurity out-diffusion.

8.5 GaN growth with SiN, SiO₂, and ZnO buffer layers

Silicon nitride buffer layers

Research in reference 154 reported that silicon nitride (SiN_x) films on lithium niobate substrates could enhance the performance of SAW devices. Because of their high resistivity properties, SiN_x films are considered a good candidate for blocking the out-diffusion from substrates. However, SiN_x films have a lattice constant of 0.76nm along the a-axis, which is almost twice that of GaN (a= 0.3189 nm). Therefore it has been claimed that SiN_x films are aligned to GaN films, resulting in the low density of dislocations [155]. However, one should note that SiN_x is monoclinic and thus possesses very little crystalline symmetry. The SiN_x films used in this previous study were formed on silicon substrates by nitridation at 900 °C, resulting in excellent GaN film growth [155]. Other research showed GaN growth with porous SiN interlayers on GaN templates with lateral epitaxial overgrowth technique using MOCVD [156] lowered the threading dislocation density.

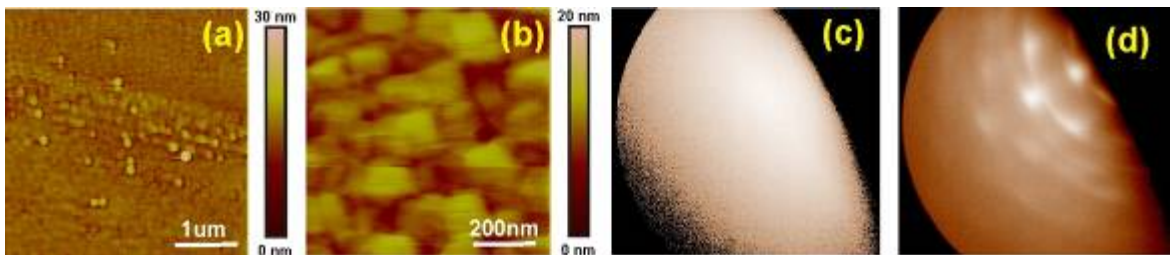


Figure 64: Surface morphology of SiN/LN (N2527) in the size of (a) 5μm x 5μm 1.35nm, (b) 1μm x 1μm with roughness of 1.21nm, amorphous RHEED pattern of (c) SiN films at 200 °C, and (d) AlN/SiN buffer layers on LN substrates at 600 °C.

Table 7: GaN films growth on SiN, SiO₂, and ZnO buffer layers: FA: furnace anneals, VA: vacuum anneals, R: resistivity, SiN: silicon nitride buffer, SiO₂: silicon dioxide buffer, and ZnO: zinc oxide buffer.

| Sample # | Pre-treat FA/VA(°C) | Buffer | Nitridation (°C)/min | AlN (°C) | GaN (°C) | R(Ω/\square) |
|----------|------------------------|------------------|-------------------------|----------|----------|-----------------------|
| N2527 | 1000/200 | SiN | 200/10min | 600 | non | 3.2E+8 |
| N2533 | 1000/200 | SiO ₂ | 800/20min | Non | 650 | 1.8E+8 |
| N2312 | 1000/200 | ZnO | Non | 600 | N/A | N/A |
| N2535 | 1000/200 | ZnO | GaN 500/2min | 600 | 600 | 3.1E+3 |

In this experiment, 100 nm thick SiN_x films were deposited on LN by plasma enhanced chemical vapor deposition (PECVD), with a deposition rate of 500Å per minute at 300 °C, rf power of 200W, and film thickness of about 100nm. Figure 64 (a) and (b) show the surface morphology of the SiN_x films on LN substrates with a roughness of 1.35nm. Importantly, the deposited SiN_x films on LN substrates are unmeasurably highly resistive. On the SiN_x films, AlN layers were grown at 600 °C after nitridation at 200 °C for 10minutes in the N2527 sample. The SiN_x and AlN/SiN_x films on LN substrates show amorphous RHEED patterns as shown in Figure 64 (c) and (d), respectively. Unlike the claim of research in reference [150] using thermally grown SiN_x, our results on PECVD deposited SiN_x indicate that these amorphous patterns are related to the lattice mismatch between SiN_x films and lithium niobate substrates, and the fast growth rate of deposition conditions. In conclusion, SiN_x films deposited with the PECVD system have amorphous crystal structure, resulting in the failure of epitaxial III-nitride growth. Therefore, epitaxial SiN_x films need to be implemented to grow successful epitaxial high-quality III-nitrides.

Silicon dioxide buffer layers

According to research in [157], the dc drift in an LN optical modulator was reduced after silicon dioxide (SiO_2) buffer layers were deposited. The dc drift could be screened by the refractivity of SiO_2 buffer layers, and the refractivity was affected by the amount of OH elements in SiO_2 films. After annealing 500 nm thick SiO_2 films at 900 °C in wet O_2 , the dc drift was minimized. Another study [158] reported the low temperature (< 285 °C) rf sputter deposition of SiO_2 films for MEMS applications. The work showed the optimized deposition conditions of SiO_2 films with low surface roughness and minimized stress. A rf-sputterer was used to deposit 100 nm thick SiO_2 films on LN substrates with 200 W rf power at a 6mTorr sputtering pressure in the N2533 sample. As a result, even though the films show unmeasurably high resistance, the SiO_2 films have amorphous RHEED patterns, indicating non-crystalline structure growth on LN substrates. The deposited SiO_2 films on LN were annealed with nitrogen at 800 °C for 20 minutes, resulting in no crystal structure change, as shown in Figure 65(a). Then, GaN films grown on the annealed SiO_2 films have amorphous RHEED patterns, as shown in Figure 65(b). Therefore, it is required to investigate a method for the epitaxially grown SiO_2 films to achieve successful epitaxial GaN films and block the impurity out-diffusion.

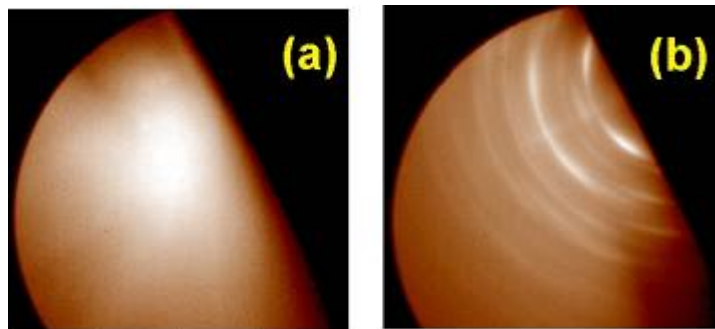


Figure 65: Amorphous RHEED pattern of (a) SiO_2 films on LN substrates at 800 °C and (b) GaN films on SiO_2 buffer (N2533).

Zinc oxide buffer layers

Zinc oxide (ZnO) materials have been highlighted as a promising piezoelectric material for acoustic and optoelectronic devices. ZnO is the correct lattice structure, hexagonal, already is saturated with oxygen and can be heavily doped with Li and thus is less likely to getter Li and O from the substrate. Thus, ZnO is a promising buffer layer for interfacing LN and III-Nitrides. ZnO materials were deposited on LN substrates by ECR-assisted MBE, since a double piezoelectric layer structure enhanced the electro-mechanical coupling factor of SAW devices [159]. The lattice mismatch between ZnO and LN is 8.3% [159]. The structural relationships between the ZnO films and LN substrates are (0001) ZnO || (0001) LN and $[10\bar{1}0]$ ZnO || $[11\bar{2}0]$ LN. The ZnO films were epitaxially grown on LN substrates, confirmed by x-ray ϕ -scans with a six-fold symmetry as shown in Figure 66 [160]. The ZnO films, however, need to be grown at low substrate temperatures because the crystal quality of ZnO films deteriorates with increasing substrate temperatures [159,160]. Other research reported epitaxially grown ZnO films on LN substrates by rf-sputtering. The FWHM of (0002) ω -rocking curve for the ZnO films grown at 550 °C was 1656" [161]. Furthermore, the lattice mismatch between GaN and ZnO is 0.4% for the c-axis and 1.9% for the a-axis [162]. Therefore, this buffer scheme is valuable to investigate because of the minimized lattice mismatch problem with ZnO buffer layers.

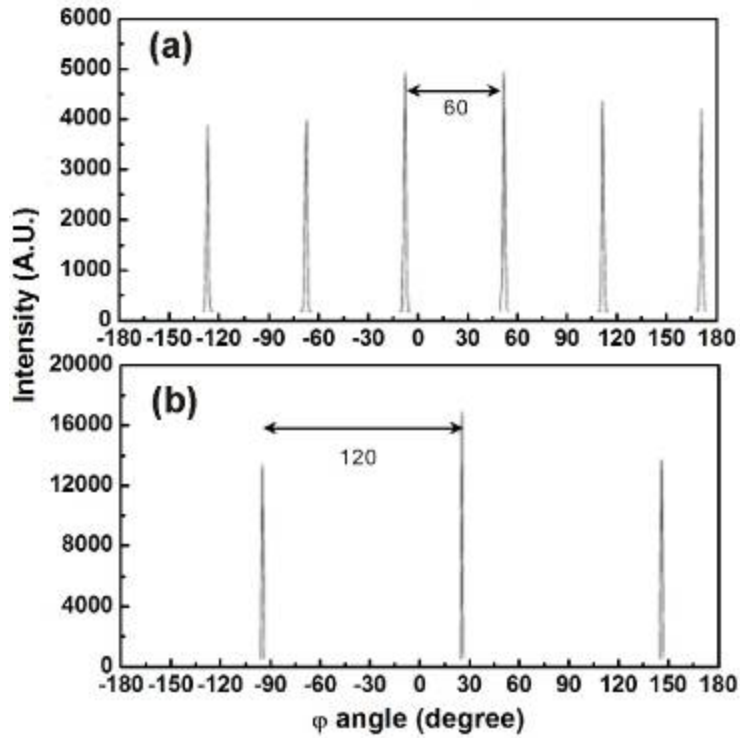


Figure 66: ϕ -scans of (a) the $(10\bar{1}1)$ ZnO and (b) the (012) LN reflections with doubled intervals [160].

In this study, ZnO films were deposited on LN substrates using rf-sputtering with two different experiments: First, the ZnO films were deposited on the positive and the negative z-axis of LN substrates. The films were deposited with 125W rf power under a 6 mTorr sputtering pressure with mixed gases ($\text{Ar}:\text{O}_2=5:5$) with a growth rate of $67 \text{ \AA}/\text{min}$ at $300 \text{ }^\circ\text{C}$ substrate temperature. Second, the ZnO films were deposited on both $1000 \text{ }^\circ\text{C}$ furnace annealed and non-annealed LN substrates. The sputtering condition was the same except for the ratio of mixed gases ($\text{Ar}:\text{O}_2 = 8:2$) with a growth rate of $45 \text{ \AA}/\text{min}$ and $400 \text{ }^\circ\text{C}$ substrate temperature.

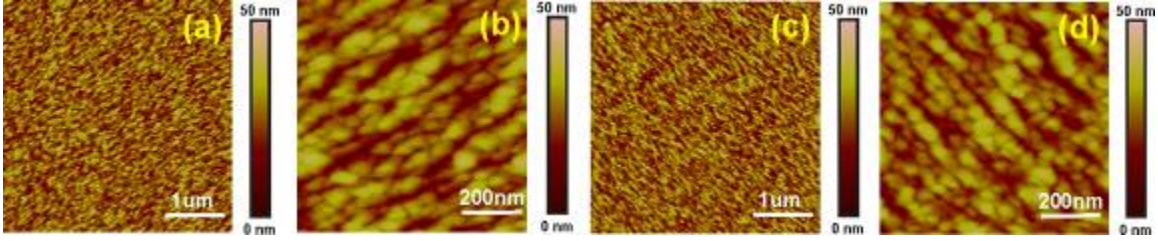


Figure 67: AFM surface morphology of ZnO films on the positive z-axis of LN substrates (a) RMS roughness = 5.34nm (b) RMS roughness = 5.48nm and the negative z-axis of LN substrate (c) RMS roughness = 5.09nm (d) RMS roughness = 1.85nm

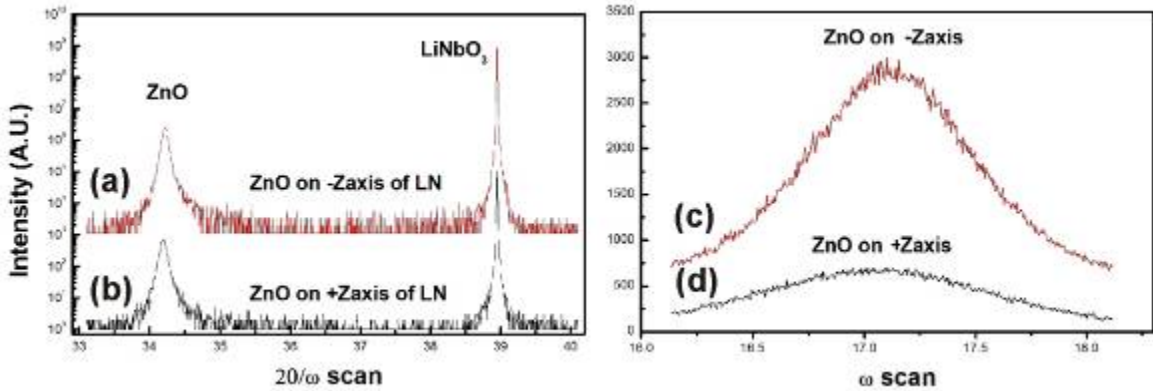


Figure 68: First experiment results: ZnO films on (a) -Z-axis of LN with FWHM of 262" and (b) +Z-axis of LN with FWHM of 324" on $2\theta/\omega$ scan; and (c) -Z-axis of LN with FWHM of 3036" (d) +Z-axis of LN with FWHM of 4415" on ω scan.

The first experiment shows the surface morphologies of ZnO films deposited on the positive and negative z-axis of LN substrates in Figure 67. Note that the crystal quality and surface roughness of the ZnO films could be better by depositing on the negative z-axis of LN substrates. The ZnO films on the positive and negative z-axis LN have the FWHMs of 262" and 324" on $2\theta/\omega$ scan, and 4415" and 3036" on ω -rocking curves, respectively, as shown in Figure 68.

In the second experiment, the ZnO films were deposited at 400 °C substrate temperature, resulting in improved crystal quality. The ZnO films on the non-annealed LN substrates have a rougher surface than that of the annealed substrates because LN

substrates have an atomically flat surface after 1000 °C furnace annealing. Figure 69 confirms the surface roughness improvement on the 1000 °C furnace annealed LN samples using AFM. Figure 70 shows that the FWHMs of (0002) ω -rocking curve for the ZnO films on 1000 °C furnace annealed and non-annealed LN substrates are 2418'' and 2750'', respectively. This result indicates that the crystal quality of ZnO films is improved on annealed LN substrates.

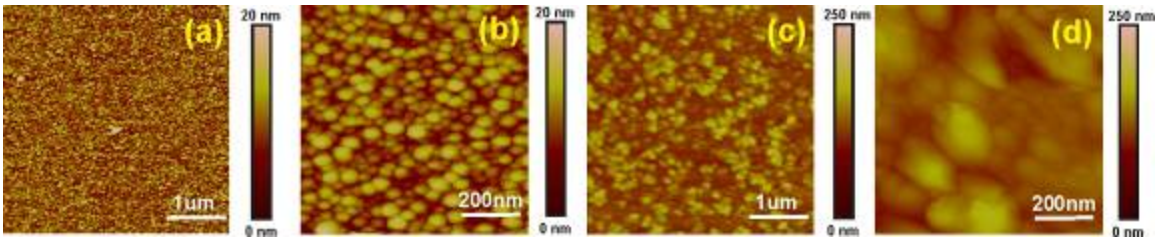


Figure 69: AFM surface morphology of ZnO films on the 1000 °C furnace annealed LN substrates (a) RMS roughness = 2.21nm (b) RMS roughness = 2.1nm and non-annealed LN substrates (c) RMS roughness = 20.1nm (d) RMS roughness = 7.49nm

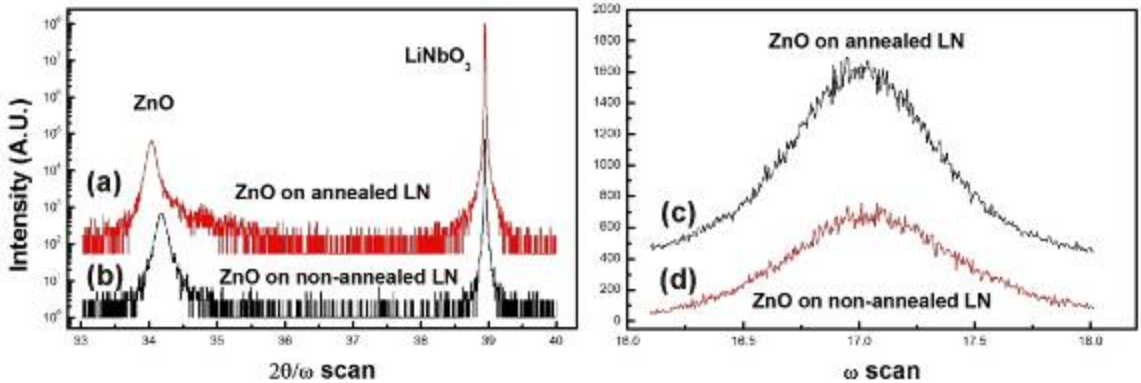


Figure 70: Second experiment results: ZnO films on (a) 1000 °C furnace annealed LN with FWHM of 380'' and (b) non-annealed LN with FWHM of 391'' on $2\theta/\omega$ scan; and (c) 1000 °C furnace annealed LN with FWHM of 2418'' (d) non-annealed LN with FWHM of 2750'' on ω scan.

The rf-sputtered ZnO films on 1000 °C furnace annealed LN substrates showed spotty RHEED patterns as shown in Figure 71(a). AlN films were grown on the ZnO films in the N2312 sample, resulting in amorphous RHEED patterns in Figure 71(b). This is a well-known alloy behavior between aluminum and zinc materials at high temperatures (over 600 °C). The sample was peeled off after growth because of the alloy problem. The alloy problem can be resolved by inserting thin GaN buffer layers before introducing AlN films. This scheme was moderately successful and showed streaky RHEED patterns in N2535 samples as shown in Figure 71(c). Then, GaN bulk layers grown on the buffer layers show 2× RHEED patterns as shown in Figure 71(d), indicating Ga-polar GaN films. Even though the GaN films on ZnO buffers show high crystal quality, the films are very conductive. This is possibly because the given ZnO targets are n-type doped materials and there are out-diffusion problems between GaN, ZnO, and LN materials.

Table 8: ZnO films on lithium niobate with rf sputterer with the rf power of 125W.

| Sample | Furnace Anneal | Growth face | Gas Type (6mTorr) | Growth Rate (Å/min) | Growth Temp.(°C) | FWHM(°) |
|--------|----------------|-------------|-------------------|---------------------|------------------|---------|
| ZnO_A | 1000°C | +Z axis | Ar:O = 5:5 | 67 | 300 | 4415 |
| ZnO_B | 1000°C | -Z axis | Ar:O = 5:5 | 67 | 300 | 3036 |
| ZnO_C | None | +Z axis | Ar:O = 8:2 | 45 | 400 | 2750 |
| ZnO_D | 1000°C | +Z axis | Ar:O = 8:2 | 45 | 400 | 2418 |

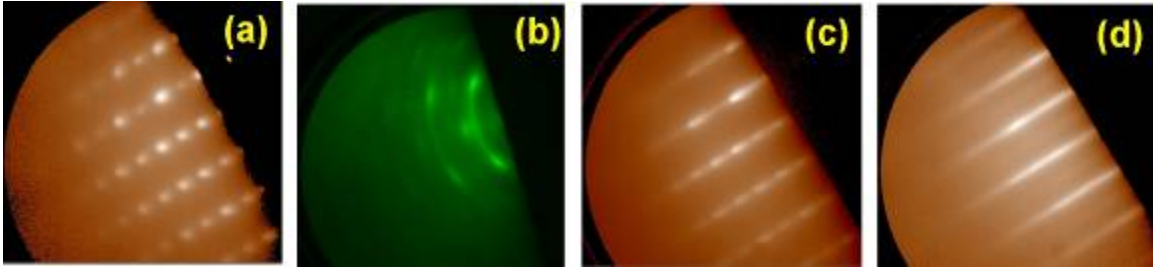


Figure 71: RHEED patterns of (a) ZnO on LN substrates (spotty) (b) AlN on ZnO/LN at 600 °C (N2312: amorphous pattern) (c) AlN layers with GaN buffer layers on ZnO/LN at 600 °C (N2535: spotty and streaky) (d) GaN films on AlN/GaN/ZnO/LN substrates (N2535: streaky 2× pattern) implying Ga-polar materials.

In conclusion, non-conductive GaN films with ZnO buffer layers were investigated with smaller lattice mismatches with LN substrates. The crystal quality and surface roughness of the ZnO films can be improved using the negative z-axis LN substrates and furnace annealed LN substrates. ZnO films deposited at higher temperatures need to be investigated in the future for improving the crystal quality, which is limited in the presently available rf sputterer system. AlN films can be grown on ZnO buffer layers by inserting thin GaN films to minimize the alloy between aluminum and zinc. GaN bulk layers on the ZnO buffer have 2× RHEED patterns, but they are conductive because of the use of n-doped ZnO target during rf-sputtering. Therefore, p-type high-resistive ZnO films need to be investigated to implement high-resistive GaN films. All of ZnO films on LN substrates are summarized in Table 8.

8.6 GaN growth with Mg, MgO, and YSZ buffer layers

Mg and MgO buffer layers

Magnesium oxide (MgO) films are a good candidate for resistive buffer layers because the films are highly resistive and chemically stable materials. MgO films were

used as a buffer layer to grow superconducting thin films on a lithium niobate substrate to minimize the microwave loss in the electrodes of optical modulators [163]. The structural relationships between the MgO films and LN substrates are MgO (0 0 1)[1 1 0] || LiNbO₃ (0 0 6)[2 1 0] with a large lattice mismatch of ~22% [164]. A study in [165] showed that if MgO films reacted with LN substrates, but the Mg doped LN bulk was more radiation tolerant, indicating higher crystalline stability. However, the significant out-diffusion of Li and O substantially degraded the superconductivity of films. As a result, the MgO films and LN substrates had an extremely deteriorated interface observed by the cross-sectional TEM images. The image showed 100nm deep crystal degradation developed into LN substrates from the surface. The MgO films had mutual diffusion of constituent atoms, Li and Nb, from LN substrates observed by energy-dispersive spectroscopy [165].

Table 9: GaN films growth on Mg and MgO buffer layers: FA: furnace anneals, VA: vacuum anneals, R: resistivity, and FWHM: full width of half maximum of GaN x-ray diffraction on (0002) Ω -scan.

| Sample | FA/VA (°C) | Buffer (°C) | SL(°C) | Annealing in O ₂ (°C)/min | AlN (°C) | GaN (°C) | R(Ω/\square) | FWHM |
|--------|------------|-------------|---------|--------------------------------------|----------|----------|-----------------------|------|
| N2534 | 1000/200 | Mg/100 | None | None | non | 600 | 1.4E+3 | 1051 |
| N2538 | 500/200 | Mg/25 | GaN 350 | None | 600 | 600 | 1.8E+6 | 2894 |
| N2553 | 1000/200 | MgO/300 | 600 | 800/30min | 600 | 600 | 1.5E+7 | 1821 |

This work recommended the use of Y₂O₃-stabilized ZrO₂ (YSZ) buffer layers to minimize the mutual diffusion. The MgO films were deposited by an rf-sputterer using the targets of Mg metal or MgO powder with various ratios of oxygen to argon. The best quality of the MgO films were deposited with a ratio of 20% of oxygen to argon [166].

Using this literature as a model, in this work, the MgO films were grown on an LN substrate using two different MBE machines. The first one is the MBE system at the Georgia Institute of Technology and the second machine is owned by a collaborator at the University of Wisconsin-Madison. MgO films were attempted to be grown using the first MBE machine, which has Mg metal sources, no oxygen plasma source, and impurity oxygen sources in the background. Since Mg sources are well-known as a getter of oxygen atoms, the Mg source was evaporated slowly onto LN substrates to trap oxygen atoms in the chamber at 100 °C for about 18 hours. The Mg sources were evaporated using an Mg cracker, whose aperture size was 100 mils and the bulk and tip temperatures were 300 °C and 900 °C, respectively. The growth conditions are summarized in Table 9.

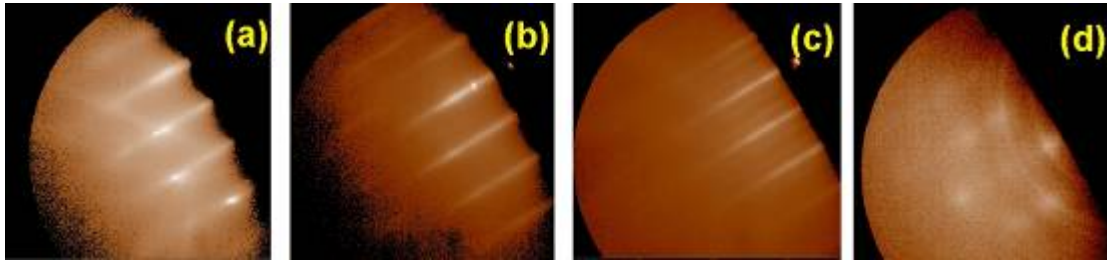


Figure 72: RHEED patterns of N2534 sample for (a) Mg metal deposition for 18 hours at 100 °C (b) the Mg on LN substrates at 600 °C (c) GaN epitaxial layers on the Mg/LN showing 3× patterns (d) Mg metal deposition for higher flux at 300 °C (N2538).

Even though MgO peaks were not found in the x-ray diffraction study, Mg-evaporated layers on the LN substrate had streaky RHEED patterns, resulting in unknown epitaxial layers as shown in Figure 72(a). The unknown Mg-evaporated layers have streaky RHEED pattern at 600 °C and are used as buffer layers to grow GaN films, resulting in the 3× RHEED patterns in the N2534 sample, as shown in Figure 72(b) and (c). Note that the GaN films with the Mg layers grown on LN substrates have reasonable

crystal quality with 1051" FWHM on 0002 ω scan, but are highly conductive with $1.4 \times 10^{+3} \Omega/\square$. This is because the Mg-evaporated layers are structurally matched to LN substrates and conductive layers. Additional Mg-evaporated layers were grown with higher Mg flux in the aperture size of 200 mils at the same temperature, resulting in amorphous RHEED patterns as shown in Figure 72(d).

The second MBE machine has an oxygen plasma source with an Mg metal source. MgO films 140 nm thick were grown at 300 °C on LN substrates and annealed at 800 °C for 30 minutes in an oxygen environment for making better crystal quality. The structural relationship between the MgO films and LN substrates is MgO (111) || LN (006), confirmed by x-ray study as shown in Figure 73. However, the MgO films have amorphous RHEED patterns because of the higher growth rate.

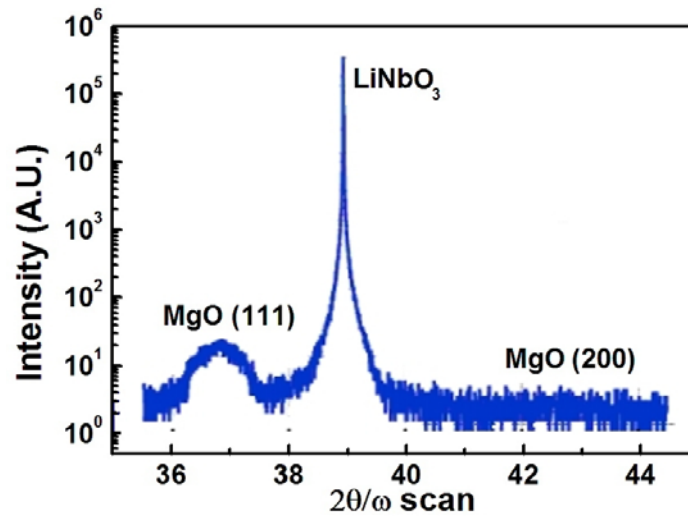


Figure 73: The crystal structural relationships of MgO films grown on LN are MgO(111) || LN (006) on $2\theta/\omega$ scan.

Another 15 nm thick MgO films was grown at a slower growth rate at 300 °C in a 4×10^{-6} Torr of an oxygen environment, resulting in the crystallized streaky RHEED

patterns shown in Figure 74(a). Then, GaN films were grown on the thin MgO films in the N2553 sample, resulting in the 3× RHEED patterns shown in Figure 74(b). This pattern is known to be a result of N-polar domains and so these domains were etched in HCl for 5 minutes. Then, thicker GaN films were grown on the etched GaN films after inserting AlN films, resulting in elimination of the 3× RHEED patterns, as shown in Figure 74(c) and (d). This implies that the AlN buffer layers could control the polarity of GaN films. The structural relationship between GaN and MgO is MgO(111) || GaN (0001), and the lattice mismatch between the two materials is about 6.5% [167]. The GaN films have rough surface morphology observed by AFM images as shown in Figure 75. The GaN films have reasonable crystal quality with 1821" FWHM on 0002 ω scan and high resistance GaN films with the resistivity of $1.5 \times 10^{+7} \Omega/\square$.

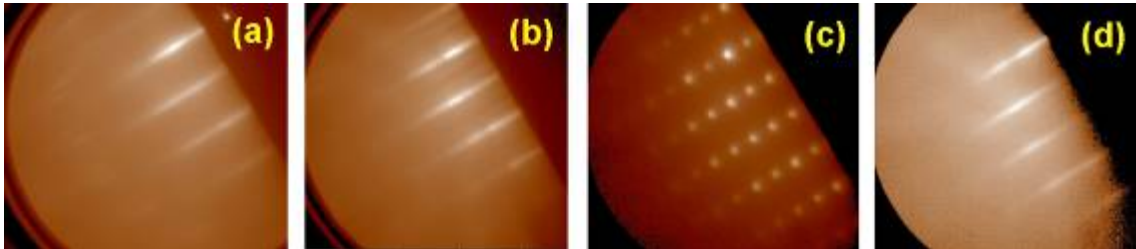


Figure 74: RHEED patterns of N2553 sample for (a) epitaxially grown MgO films on LN substrates at 550 °C (b) Pre-grown GaN films on the MgO/LN with 3× patterns (c) etched pre-grown GaN films (d) post-grown GaN films without 3× patterns.

In conclusion, epitaxial Mg-evaporated layers can be grown on LN substrates as confirmed by RHEED patterns. GaN films grown on Mg-evaporated layers have reasonable crystal quality but are highly conductive. MgO films were epitaxially grown on LN substrates with GaN films grown on the MgO films showing 3 × RHEED patterns. The GaN films were etched and re-grown after inserting AlN films resulting in no more

the $3 \times$ RHEED patterns. GaN films with MgO buffer layers have reasonable crystal quality and high resistivity.

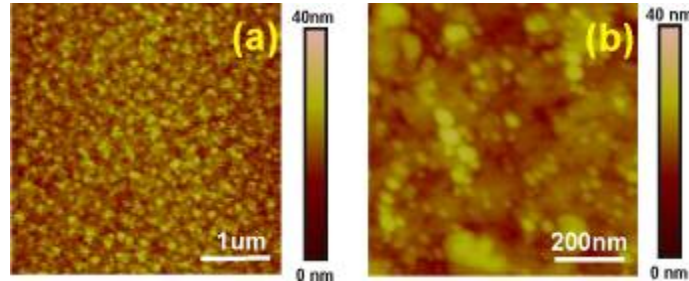


Figure 75: AFM surface morphology of N2553 sample of GaN/AlN/MgO/CLN structure in (a) $5\mu\text{m} \times 5\mu\text{m}$ scale with the rms roughness of 3.25nm (b) $1\mu\text{m} \times 1\mu\text{m}$ scale with the rms roughness of 2.09nm.

Y₂O₃-stabilized ZrO₂ buffer layers

The previous work [165] showed that MgO films and LN substrates had mutual inter-diffusion, which deteriorated the interface between the two materials. That work introduced the use of Y₂O₃-stabilized ZrO₂ (YSZ) layers as buffer layers to minimize the mutual diffusions. The unit cell of the YSZ layers is almost six times larger than that of LN substrates, expecting a successful epitaxial growth. Another study [168] reported that double CeO₂/YSZ buffer layers provided a single in-plane orientation and superior superconducting properties. Reference 169 showed that YSZ bulk crystals were used as a substrate to grow GaN films. The YSZ crystals have very small c-plane lattice mismatch (0.6%) between GaN ($c = 0.5185\text{nm}$) and YSZ ($c = 0.515\text{nm}$). This research work also showed that GaN films on YSZ substrates were grown at low temperatures, resulting in suppression of the out-diffusion from substrates.

Table 10: Y₂O₃-stabilized ZrO₂ (YSZ) buffer and/or CeO₂ buffer layers on lithium niobate substrates with various growth conditions.

| Sample | Buffers (nm) | Growth temp. (°C) | Roughness (nm) | Secondary phases |
|--------|-----------------------------|-------------------|----------------|------------------|
| YSZ1 | YSZ 200 | 650 | 0.975 | Yes |
| YSZ2 | CeO ₂ 250 | 650 | 1.74 | Yes |
| YSZ3 | YSZ 200/CeO ₂ 20 | 650 | 0.360 | Yes |
| YSZ4 | YSZ 200 | 300/650 | 0.105 | Yes |
| YSZ5 | YSZ 200 | 400 | 0.199 | A little bit |
| YSZ6 | YSZ 200 | 350 | 0.197 | No |
| YSZ7 | YSZ 200 | 300 | 0.206 | No |
| YSZ8 | YSZ 200 | 350 | 0.348 | No |

The YSZ buffer layers and/or CeO₂ buffer layers were grown on LN substrates by rf-sputtering with an oxygen pressure of 0.1 mTorr and 150 mTorr, respectively at a collaborator, Chang Beom Oem at the University of Wisconsin-Madison. A summary of the growth conditions is shown in Table 10. The first three samples were grown to investigate the effects of YSZ and CeO₂ on the surface roughness and crystal quality. YSZ buffer layers grown at 650 °C in the YSZ1 sample have a rough surface as shown in Figure 76(a) and have undesirable secondary phases in x-ray diffraction on the 2θ/ω scan in Figure 77(a). The CeO₂ buffer layers have the worst surface roughness as shown in Figure 76(b). However, the CeO₂ buffer layers have fewer secondary phases in x-ray diffraction on 2θ/ω scan, as shown in Figure 77(b), implying less inter-diffusion. The rough surface becomes smoother when using doubled YSZ/CeO₂ buffer layers. The doubled buffer layers also show fewer secondary phases in x-ray diffraction on the 2θ/ω

scan as shown in Figure 77 (c). As a result, a single YSZ buffer layer has the best crystal quality and doubled YSZ/CeO₂ buffer layers have the best surface smoothness.

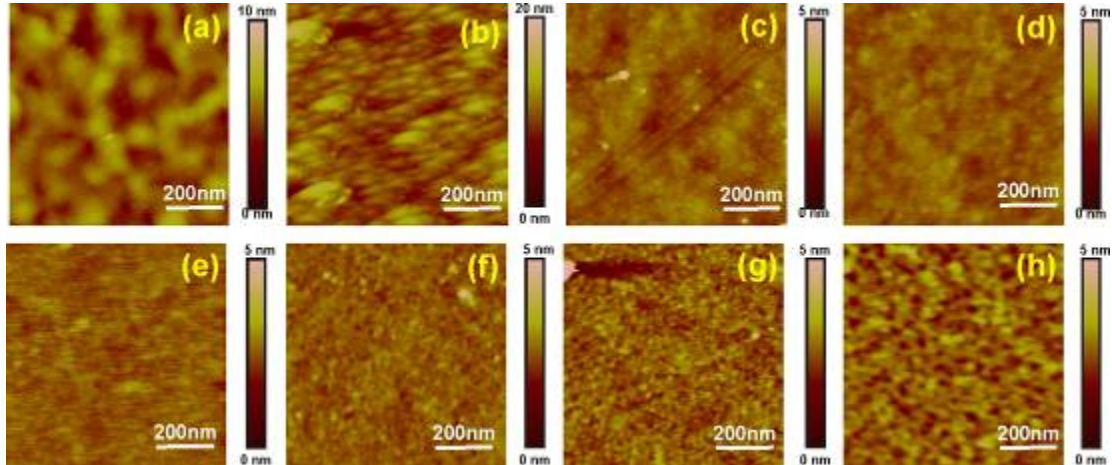


Figure 76: AFM surface morphology of (a) YSZ1 sample with the roughness of 0.975nm (b) YSZ2 sample with the roughness of 1.74nm (c) YSZ3 sample with the roughness of 0.360nm (d) YSZ4 sample with the roughness of 0.105nm (e) YSZ5 sample with the roughness of 0.199nm (f) YSZ6 sample with the roughness of 0.197nm (g) YSZ7 sample with the roughness of 0.206nm (h) YSZ8 sample with the roughness of 0.348nm.

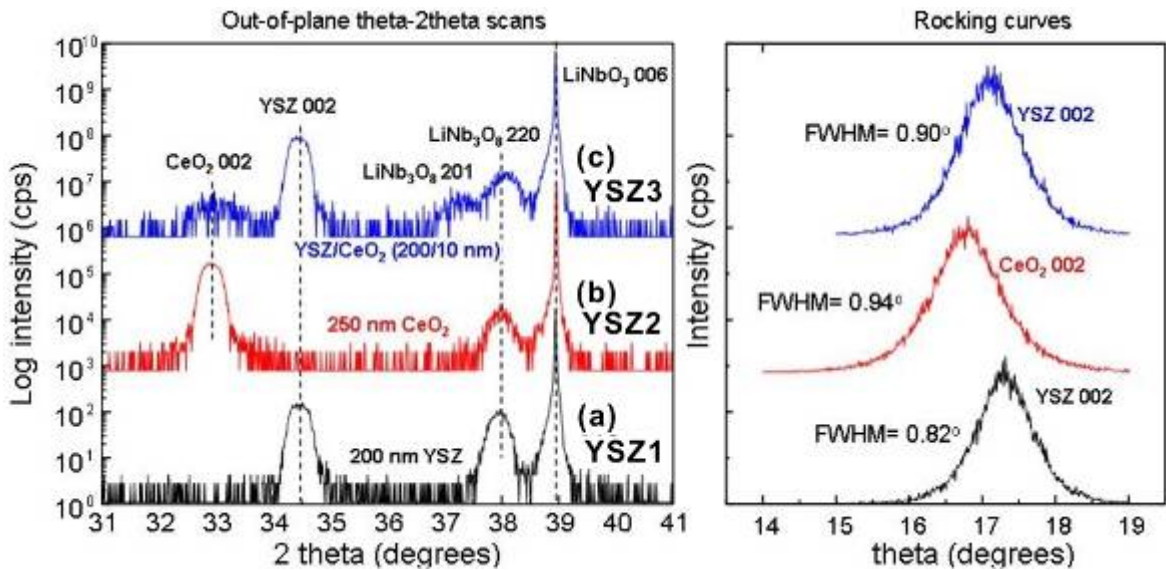


Figure 77: Left figure: X-ray diffraction on 2θ - ω scan for (a) YSZ1 sample (bottom black color), (b) YSZ2 sample (middle red color), and (c) YSZ3 sample (top blue color). Right figure: x-ray diffraction rocking curve, ω spectrum, for these three samples.

The single YSZ buffer layers were grown at various growth temperatures to optimize crystal quality and surface roughness. At lower growth temperatures, the samples have rougher surfaces and fewer secondary phases as shown in Table 10. The YSZ4 sample was grown at two different growth temperatures, 300 °C and 650 °C, resulting in the smoothest surface. As mentioned in a previous section, low-temperature growth shows the smallest mutual diffusion between films and substrates.

Among these samples, GaN films were grown on the YSZ4 and YSZ8 samples. The YSZ buffer layers on the YSZ4 sample show streaky RHEED images at 200 °C, as shown in Figure 78(a). However, the sample shows two distinguishable reconstruction RHEED patterns at 650 °C as shown in Figure 78(b), implying film delamination. Then, SL layers and GaN layers were sequentially grown on the YSZ buffer layers at 650°C and 600°C, respectively, showing slightly amorphous RHEED patterns (Figure 78(c) and (d)). After finishing the growth, all GaN films were peeled off.

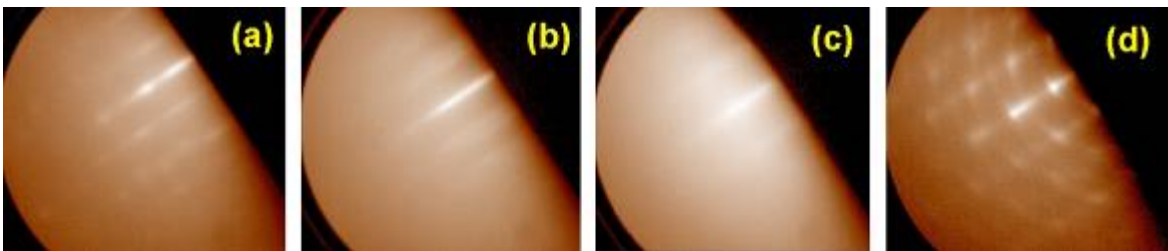


Figure 78: RHEED images of the YSZ4 sample (a) YSZ buffer layers on LN substrates at 200 °C (b) two distinguishable reconstruction RHEED patterns at 650 °C (c) during AlN layer grown on SL/YSZ/LN at 650 °C for 6min (d) amorphous RHEED patterns of GaN at 600 °C for 34min.

The YSZ buffer layers in the YSZ8 sample were grown at 350 °C and had a rough surface and no secondary phase. GaN films were grown on the YSZ8 sample using a low-temperature buffer growth scheme to minimize the film-delamination problem. The film-

delamination problem seems to be solved when the low-temperature GaN films were grown at 500 °C, as shown in Figure 79 (a) and (b). However, GaN films have amorphous RHEED patterns at a higher growth temperature of 600 °C, as shown in Figure 79 (c). Further GaN film growth shows an unusual reconstruction RHEED patterns, indicating a crystal structural change. After finishing the growth, the GaN films were again peeled off.

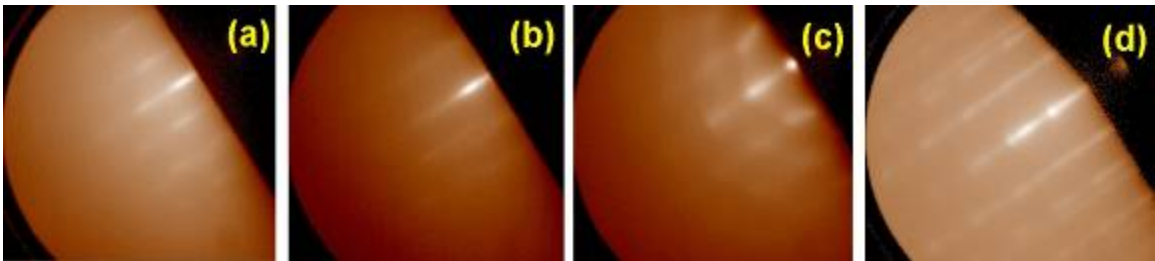


Figure 79: RHEED images of the YSZ8 sample (a) YSZ buffer layers on LN substrates at 470 °C (b) after growing low-temperature GaN layers at 500 °C for 2min (c) amorphous RHEED patterns of GaN at 600 °C for 6min (d) after growing GaN layers at 600 °C for 1hour growth, showing the two distinguishable reconstruction RHEED patterns.

In conclusion, the YSZ buffer layers on LN substrates need to be grown at low-temperatures because of the out-diffusion problems between the YSZ layers and substrates. Grown at lower temperatures, the crystal quality and roughness of the samples became worse. Doubled YSZ/CeO₂ buffer layers show improved surface roughness. However, single YSZ buffer layers at two different growth temperatures have the smoothest surface. Finally, GaN films were grown on the buffer layer, but have unusual RHEED patterns, resulting from film delamination.

8.7 GaN growth on lithium tantalate with low-temperature buffers

500 °C furnace-annealed lithium tantalate (LT) samples

In this section, GaN films were grown on lithium tantalate (LT) substrates with low-temperature buffer layers. As low-temperature buffer layers, the GaN/AlN alternating layers in the sample N2488 in section 8.2 were used since the sample showed the highest resistivity, but poor crystal quality. Therefore, the buffer layers were grown in various temperatures range in an attempt to improve the crystal quality. A summary of the experiment is provided in Table 11. The first three samples (N2536, N2539, and N2541) used the GaN/AlN alternating layers as the buffer layers with different growth temperatures (300 °C, 400 °C, and 500 °C). The alternating layers were grown at low temperatures and consisted of periodical GaN and AlN layers as the same way in the sample N2488. Then GaN bulk layers were grown at 600 °C on the alternating layers. The crystal quality of the GaN bulk layers was the worst at the lowest growth temperature and had unmeasurably high resistivity. However, the GaN bulk layers became conductive after growing alternating layers at 500 °C. The resistivity and crystal quality are shown in Figure 80 as a function of the alternating layer growth temperatures. The buffer layers efficiently block the mutual diffusion below a growth temperature of 500 °C. However, all of the cases show very poor crystal quality because of the low-temperature growth. To improve the GaN crystal quality, the samples were annealed at 800 °C for 1 minute or 10 minutes (N2545 and N2547), resulting in no improvement of GaN crystal quality. However, the resistivity of GaN films was decreased because of the out-diffusion from the substrates. Note that this anneal proves that the GaN resistivity in these samples is mainly affected by the out-diffusion from the substrates.

Table 11: GaN films growth on lithium tantalate substrates with low-temperature buffer layers: FA: furnace anneals, SL: super-lattice, VA: vacuum anneals, AL: the GaN/AlN alternating layers, R: resistivity, and FWHM: full width of half maximum of GaN x-ray diffraction on Ω -scan.

| Sample | FA/VA (°C) | Buffer (°C) | Anneals or Buffer (°C)/min | AlN (°C) | GaN (°C) | R(Ω/\square) | FWHM |
|--------|------------|-------------|----------------------------|------------|----------|-----------------------|------|
| N2536 | 500/200 | AL 300 | None | 600 | 600 | 9.0E+10 | 4553 |
| N2539 | 500/200 | AL 400 | None | 600 | 600 | 3.6E+10 | 3711 |
| N2541 | 500/200 | AL 500 | None | 600 | 600 | 2.0E+4 | 3182 |
| N2545 | 500/200 | AL 400 | 800/10min | 600 | 600 | 1.4E+4 | 3491 |
| N2547 | 500/200 | AL 400 | 800/1min | 600 | 600 | 1.3E+5 | 3594 |
| N2548 | 500/200 | GaN 500 | None | 650 | None | 8.1E+4 | N/A |
| N2550 | 500/200 | AlN 550 | GaN 550 | 600 | 600 | 5.9E+4 | 1858 |
| N2554 | 500/200 | GaN 600 | None | 650 | 600 | HEMT | 1658 |
| N2551 | 500/200 | SL 475 | GaN 475 | AlGaIn 475 | 550 | 1.2E+6 | 2890 |

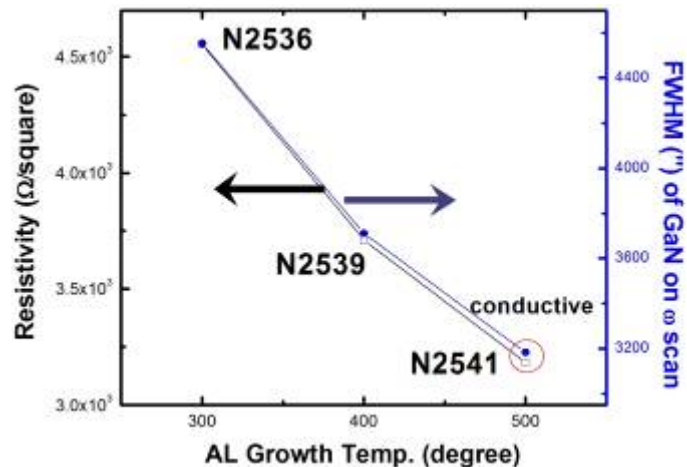


Figure 80: The resistivity and crystal quality of GaN films as the function of the GaN/AlN alternating layer (AL) growth temperatures.

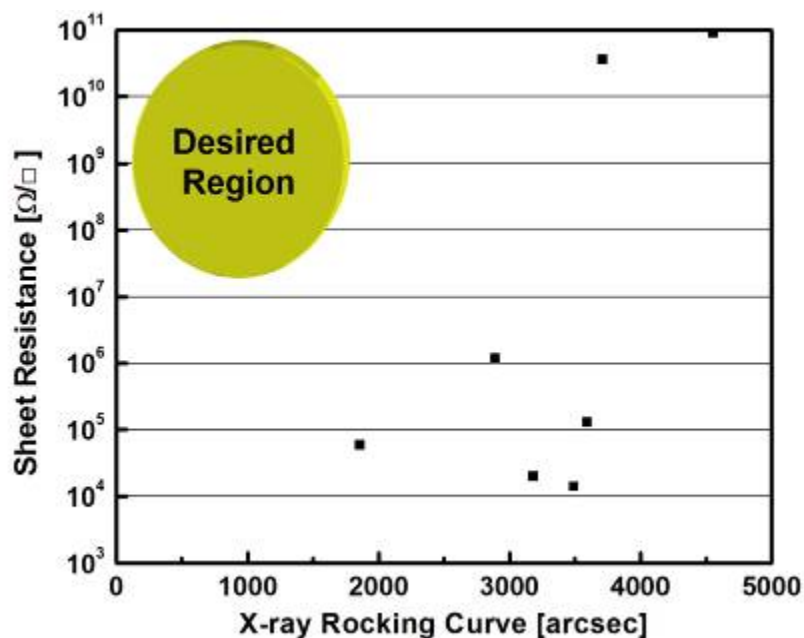


Figure 81: Summary of the data in Table 11 for LT samples.

In sample N2548, GaN buffer layers were grown at 500 °C on LT substrates, and then AlN films were grown on top of the buffer layers, but, again this resulted in highly conductive AlN films. The high conductivity of AlN films is caused by the out-diffusion, implying inefficient impurity blocking of the GaN buffer layers. GaN bulk layers grown on AlN buffer layers are still highly conductive in the N2550 sample. Finally, a HEMT structure with GaN buffer layers was grown on LT substrates in the N2554 sample, resulting in reasonable crystal quality but no measurable mobility. This is because GaN buffer layers were grown at a high temperature, which increased out-diffusion, resulting in the sheet charge of $-4.8E+13 \text{ cm}^{-2}$, which is four times higher than normal. The previous growth conditions of N2453, whose films were grown on LN substrates, were repeated on LT substrates in the N2551 sample, resulting in relatively highly resistive GaN films, but poor GaN crystal quality.

1000 °C furnace-annealed lithium tantalate (LT) samples

The surface of GaN films grown on 500 °C annealed LT substrates had scratches caused by the manufacturer polish scratches of the LT substrates. The scratch problem could be solved using 1000 °C furnace annealing, which provided atomically smooth surface morphology. The effect of furnace annealing was investigated in two samples: N2557 and N2559, which were annealed at 500 °C and 1000 °C, respectively. As a result, there was remarkable improvement of GaN crystal quality with the 1000 °C annealed LT samples in the N2559 sample. However, the two samples show highly conductive properties and even 3× RHEED patterns in N2559 indicative of N-polar GaN. The growth conditions are summarized in Table 12.

Table 12: GaN films growth on lithium tantalate substrates with low-temperature buffer layers: FA: furnace anneals, VA: vacuum anneals, S: super-lattice & AlN, R: resistivity (Ω/\square), μ : Hall mobility (cm^2/Vs), ρ : sheet charge (cm^{-2}), H: HEMT, 3x: 3× RHEED patterns, and FWHM(?): full width of half maximum of GaN x-ray diffraction on Ω -scan.

| Sample | FA/VA (°C) | 2 nd VA °C/min | buffer (°C) | Anneal °C/min | AlN (°C) | GaN (°C) | R or μ | $\rho(\text{cm}^{-2})$ | FWHM (") |
|--------|------------|---------------------------|-------------|---------------|----------|----------|------------|------------------------|----------|
| N2557 | 500/200 | 700/7 | GaN500 | 700/13 | None | 600 | 1.2E+3 | -1.5E+15 | 2545 |
| N2559 | 1000/200 | 700/7 | GaN500 | 700/13 | None | 600 | 3x)8.4E+3 | -2.5E+14 | 1503 |
| N2571 | 1000/200 | 700/5 | GaN600 | 750/13 | S 650 | 600 | 3x) H 20 | -1.5E+13 | 1380 |
| N2566 | 1000/200 | 700/7 | AlN650 | 750/20 | None | None | 2.8E+6 | -2.6E+11 | N/A |
| N2560 | 1000/200 | 700/7 | AlN650 | 750/13 | 650 | 600 | 3x)3.6E+4 | 1.1E+13 | 1854 |
| N2567 | 1000/200 | 700/7 | AlN650 | 750/13 | S 650 | 600 | H 230 | -1.8E+13 | 1450 |
| N2564 | 1000/200 | 700/7 | AlN650 | 750/13 | S 650 | 600 | H 285 | -2.0E+13 | 1762 |
| N2640 | 1000/200 | 800/5 | AlN650 | 750/30 | S 650 | 600 | H 260 | -3.3E+13 | 1339 |
| N2561 | 1000/200 | 700/7 | AlN650 | 850/13 | 700 | 600 | 3x)1.9E+4 | -6.8E+14 | 1701 |
| N2562 | 1000/200 | 700/7 | AlN650 | 850/13 | 700 | 600 | 3x)5.2E+3 | -8.8E+13 | 1616 |

In this section, the conductivity of GaN films was controlled by suppressing the out-diffusion from LT substrates. According to experiments in the previous sections, the vacuum annealing at higher temperatures enhanced the resistivity, but long-time annealing made a porous-shaped surface of the LN substrates as shown in Figure 58 (b), resulting in degraded crystal quality and surface roughness. Therefore, a new high-temperature annealing method is proposed as follows: First, outgas the sample at high temperatures (≤ 800 °C) for 5 or 7 minutes. Second, grow very thin GaN or AlN layers to prevent the surface from becoming porous. Finally, anneal the samples at high temperatures (≤ 850 °C) for 13 or 30 minutes.

The first outgassing step makes the sample surface clean and well-crystallized, confirmed by RHEED image changes, which have bright streak RHEED patterns after outgassing as shown in Figure 82 (a) and (b). The second step provides very thin (< 10 nm) GaN or AlN capping layers (Figure 82 (c) and (d)), showing that AlN capping layers have a smoother surface than that of the GaN capping layers. The GaN and AlN capping layers have unknown-alloyed clusters, as shown in Figure 83 (a) and (c). The unknown-alloyed clusters were formed after long-time annealing (13 ~ 30 minutes) resulting from a possible alloy of lithium and aluminum or gallium. The clusters with GaN capping layers were 90 nm high and partially etched by HCl in 5 minutes, as shown in Figure 83 (b). The clusters with AlN capping layers were shorter and completely etched by HCl in 5 minutes, as shown in Figure 83 (d).

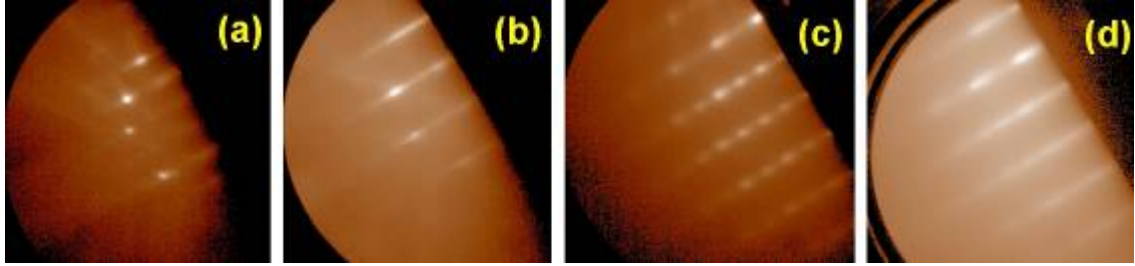


Figure 82: RHEED patterns of LT substrates (a) before outgassing at 200 °C and (b) after outgassing at 700 °C; and RHEED patterns of (c) GaN cap-layer grown at 500 °C in N2557 sample and (d) AlN cap-layer grown at 650 °C in N2560 sample.

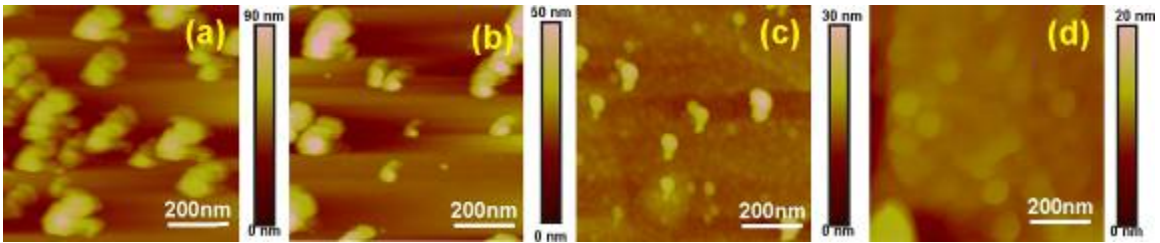


Figure 83: AFM image of (a) the annealed GaN capping layers with the rms roughness of 8.47nm and near 90nm heights, (b) after HCl etching, the rms roughness of 4.31nm with 50nm heights, (c) the annealed AlN capping layers with the rms of 2.81nm with 30nm heights, and (d) after HCl etching, the rms roughness of 0.32nm with 20nm heights.

The new strategy was applied with various growth parameters to find an optimized condition. From two samples, N2557 and N2559, it is concluded that the 1000 °C annealed LT sample provided not only higher crystal quality, but also lower conductivity and electron concentration. However, the N2559 sample (1000 °C annealed sample) had $3 \times$ RHEED patterns after cooling as shown in Figure 84 (a), indicating N-polar GaN films. Similar conditions were applied to a HEMT structure in the N2571 sample with additional SL and AlN layers, resulting in the unsuccessfully removal of the $3 \times$ RHEED patterns and no mobility.

The electrical properties of AlN capping layers in the N2566 sample are shown with relatively low resistivity and high sheet charges. Since the AlN capping layers had

better surface morphologies than that of GaN capping layers, the AlN capping layers were chosen for further experiments. The N2560 sample had lower conductivity and sheet charges, but worse GaN crystal quality and the existence of $3 \times$ RHEED patterns compared to that of N2559. A HEMT structure in the N2567 sample was grown with SL and AlN buffer layers after using AlN capping layers, resulting in a mobility of 230 cm^2/Vs and the successfully removal of the $3 \times$ RHEED patterns. The sample also showed higher crystal quality because of the improved surface smoothness of the AlN capping layers after etching. However, this approach showed that the annealed AlN capping layers had scratches on the surface, which affected the surface roughness of the GaN bulk layers as well. The scratched AlN layers were shown in Figure 83 (c) and (d). Even with a Ga-droplet growth condition, GaN films on the scratched layers had the same patterns of scratches shown in Figure 84 (b) and (c).

The scratch problem is originally from poor polished LT substrates and is resolved by 1000 °C furnace annealing, resulting in an atomically smooth surface. However, the AlN-capping-layer annealing pulled out lithium molecules from the LT substrate. Therefore, well-polished LT substrates are required for future improvements.

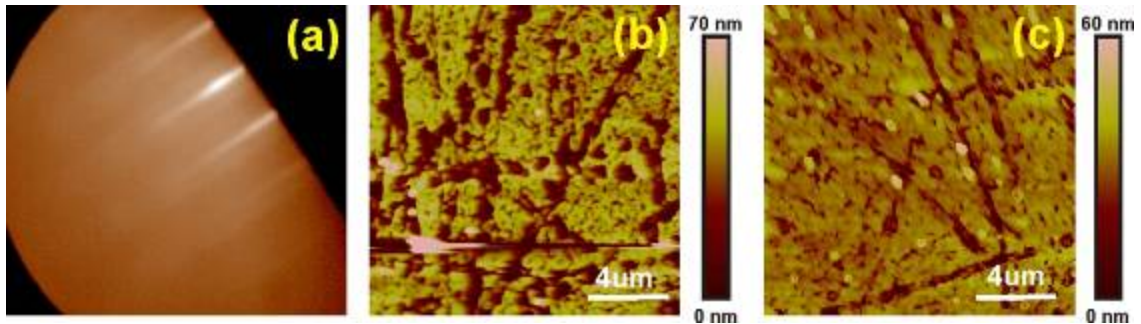


Figure 84: (a) $3 \times$ RHEED patterns of N2559 sample, AFM surface morphology of (b) N2567 with the rms roughness of 9.03nm (c) N2564 with the rms roughness of 5.89nm.

Note: the surface of N2567 and N2564 samples had droplets but very rough surface.

To investigate the etching effect of the annealed AlN capping layers, the same growth condition used in N2567 was repeated in the N2564 sample without etching the capping layers. The etched capping layers gave the better GaN crystal quality by producing a smoother surface. However, the non-etched sample showed better mobility. After increasing the outgassing temperature and annealing time in the N2640 sample, the sample had improved crystal quality and increased sheet charge, resulting in degraded mobility. The AFM surface morphologies of these samples are shown in Figure 85. Among these samples, the N2640 sample shows the smoothest surface and highest crystal quality, but also the highest sheet charges. This result implies that annealing at 800 °C and for a long time could increase the chance of out-diffusion from the substrates, resulting in increased sheet charge and degraded mobility.

The polarization directions of the substrates could affect the electrical properties. To investigate the polarization directions, two samples (N2561 and N2562) were grown on the +z axis and -z axis of LT substrates, respectively. GaN films grown on the +z axis of the LT substrate had higher resistivity but higher sheet charge with worse crystal quality than those of GaN films on the -z axis. The GaN films grown on both +z and -z axis LT samples showed $3 \times$ RHEED patterns.

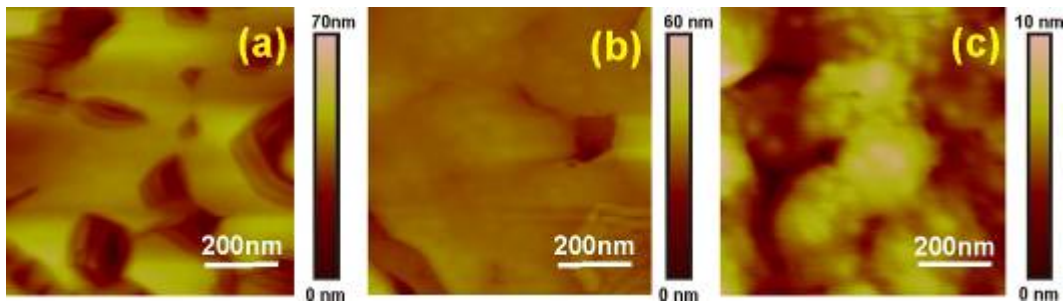


Figure 85: AFM surface morphologies in size of $1 \mu\text{m} \times 1 \mu\text{m}$ (a) N2567 with the roughness of 2.61nm (70nm height) (b) N2564 with the roughness of 1.77nm (60nm height) (c) N2640 with the roughness of 1.04nm (10nm height)

In conclusion, a new high-temperature annealing method is introduced in LT substrates and shows effective reduction of resistivity. The scheme has GaN or AlN capping layers after being outgassed at high temperatures for 5 or 7 minutes. GaN bulk layers on the GaN capping layers have the $3\times$ RHEED patterns even with SL and AlN buffer layers. The AlN capping layers have better surface morphology than that of GaN capping layers. LT substrates annealed at 500 °C have numerous scratches that degrade crystal quality. However, after annealing at 1000 °C, the LT substrates have an atomically flat surface, resulting in improved crystal quality. GaN films grown on non-etched AlN capping layers have better mobility than that of etched cases. GaN films grown on the +z axis of the LT substrate show higher resistivity but higher sheet charge, with worse crystal quality than those of GaN films on the -z axis. The GaN films grown on both the +z and -z axis LT samples showed the $3\times$ RHEED patterns.

Table 13: GaN films growth on lithium tantalate substrates with low-temperature buffer layers: FA: furnace anneals, VA: vacuum anneals, S: super-lattice & AlN, E: etched sample by HCl, μ : Hall mobility (cm^2/Vs), N_{SHEET} : sheet charge (cm^{-2}), and FWHM: full width of half maximum of GaN x-ray diffraction on Ω -scan.

| Sample | FA/VA (°C) | 2 nd VA °C/min | buffer (°C) | Anneal °C/min | AlN (°C) | GaN (°C) | μ (cm^2/Vs) | N_{SHEET} (cm^{-2}) | FWHM |
|--------|---------------|------------------------------|----------------|------------------|-------------|-------------|--------------------------------------|--|------|
| N2642 | non/200 | 700/7 | AlN650 | 700/13 | S 650 | 600 | 120 | -1.6E+13 | 1639 |
| N2644 | non/200 | 700/7 | AlN650 | 700/13 | E 650 | 600 | 1.2 | -1.0E+14 | 1559 |
| N2646 | non/200 | 700/7 | AlN650 | 750/13 | 650 | 600 | 37 | -7.7E+13 | 1522 |
| N2656 | non/200 | 700/7 | AlN650 | 750/13 | S 660 | 600 | 0.73 | -8.9E+13 | 1403 |

8.8 GaN growth on stoichiometric lithium niobate

In the previous section, the GaN films on the annealed AlN capping layers had high resistivity. However, they had scratches because the annealing of AlN capping layer disclosed the scratching problem on lithium tantalate (LT) substrates. Instead of using the LT substrates, the annealed AlN capping layer procedure was applied to non-annealed stoichiometric lithium niobate (SLN) substrates. The growth conditions are summarized in Table 13.

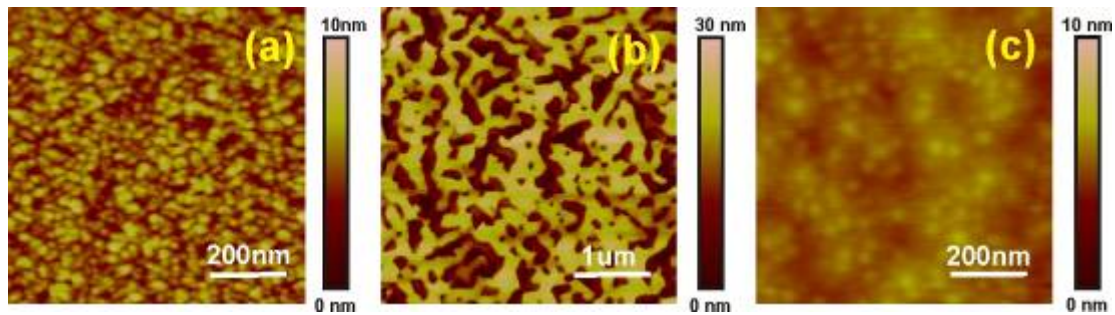


Figure 86: AFM surface morphologies of (a) annealed AlN-capping layer on SLN with the rms roughness of 1.1nm in N2642 sample (b) HEMT structure with the rms roughness of 7.87nm in the same N2642 sample (c) HEMT structure with different growth condition with the rms roughness of 0.273nm in N2644.

Figure 86 shows the surface morphologies of (a) the annealed AlN-capping layers and (b) the HEMT structure of the N2642 sample. The annealed AlN capping layers on SLN show no scratching problem with smooth surfaces. Details of the growth conditions are provided in Table 13. However, the HEMT structure on the annealed AlN capping layers shows rough surface morphology, resulting from a gallium-deficient condition. The GaN films were grown with a shutter modulation technique, which periodically opens and closes each metal source shutter. The shuttering timing was 10 seconds open and 5 seconds closed, resulting in a 1 μm/hr growth rate. However, to achieve the

gallium-enhanced condition, gallium flux was increased by a factor of two and the shutter timing was changed to 10 seconds open and 16 seconds closed with a 0.6 $\mu\text{m/hr}$ growth rate. The HEMT structure grown with the new shutter modulation technique in N2644 has a very smooth surface, as shown in Figure 86(c) with no measurable Hall mobility. The N2646 and N2656 samples were grown using the same growth condition, with the SL layers, resulting in no measurable Hall mobility. All of the HEMT structures grown with the new scheme showed no measurable mobility. This result may be because the slow growth rate of GaN films provided a greater opportunity for impurity in-diffusion into GaN bulk layers, resulting in very conductive GaN bulk layers. Therefore, future research work needs to investigate the faster growth rate of GaN films with a smooth surface and the use of SL buffers to block inter-diffusion.

8.9 GaN growth using ammonia as the source of reactive nitrogen

GaN films were grown on lithium niobate (LN) substrates with ammonia as the source of reactive nitrogen instead of using nitrogen gas supplied from an rf-plasma source. The reactive nitrogen source is provided by the thermal disassociation of ammonia on the substrate surface [170]. After a 1 hour nitridation of the LN substrates at 700 °C with the ammonia source, GaN films were grown at 700 °C after growing AlN buffer layers.

The effects of nitridation on LN substrates were investigated in the N2181 and N2182 samples with ammonia for 1 hour at 700 °C and 800 °C, respectively. After the 1 hour nitridation at 700 °C, the surface of the samples had porous shapes with average roughness of 1.74nm as shown in Figure 87 (d). The RHEED images of the LN substrates

are shown in Figure 87 (a) before nitridation, after nitridation at (b) 700 °C and (c) 800 °C for 1 hour. The LN sample with 700 °C nitridation has bright spots in the middle of streaky RHEED lines, indicating a faceted surface. The sample with 800 °C nitridation has dimmer streaky RHEED patterns, indicating a rougher surface during nitridation at higher temperatures. The growth conditions are summarized in Table 14.

Table 14: GaN films growth on lithium tantalate substrates with low-temperature buffer layers: FA: furnace anneals, VA: vacuum anneals, and FWHM: full width of half maximum of GaN x-ray diffraction on Ω -scan.

| Sample | FA/VA (°C) | Nitridation (°C)/min | AlN (°C) | GaN (°C) | FWHM |
|--------|------------|----------------------|-----------|----------|------|
| N2181 | 500/200 | 700/60 | None | None | N/A |
| N2182 | 500/200 | 800/60 | None | None | N/A |
| N2175 | 500/200 | 700/30 | None | 700 | N/A |
| N2187 | 500/200 | 700/30 | 700 | 700 | 2480 |
| N2183 | 500/200 | 800/30 | 750/20min | 700 | 2376 |

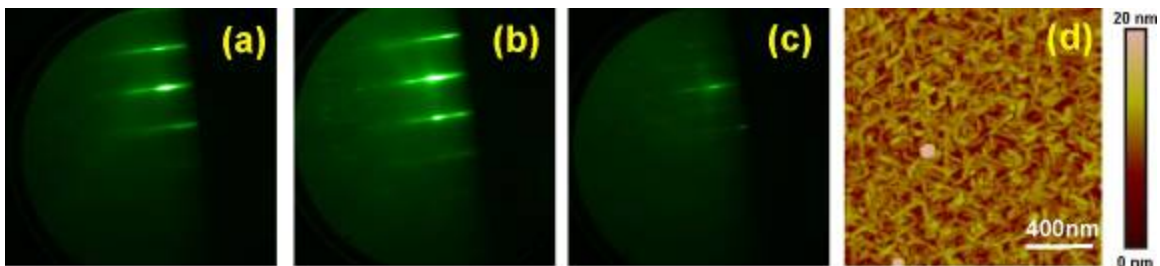
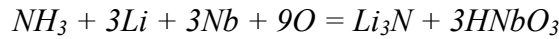


Figure 87: (a) before nitridation and after nitridation for 1 hour at (b) 700 °C (c) 800 °C of substrate temperature in the sample N2181 and N2182. and (d) surface morphologies by AFM with the area of 2 μ m x 2 μ m RMS roughness of 1.74nm after nitridation at 700 °C.

Figure 88 (a) shows the x-ray diffraction of the LN sample with nitridation at 700 °C. This diffraction has an unknown peak at 38.0218 ° with an FWHM of 346 on the

$2\theta/\omega$ scan. The sample with nitridation at 800 °C shows a wider peak and complete phase-separation between the LiNbO_3 peak and the unknown peak, as shown in Figure 88 (b). The additional unknown peak was investigated using thermodynamic equations provided by HSC Chemistry software [171]. The following equation is thermodynamically favorable to form after nitridation on LN substrates.



A previous study in reference 172 reported the nitridation effects on LN substrates. After nitridation, the LN substrates could react with ammonia and produce several bi-products including cubic oxynitride phase ($\text{Li}_a\text{NbO}_b\text{N}_c$) as described in a following equation, confirmed by x-ray diffraction as shown in Figure 89.

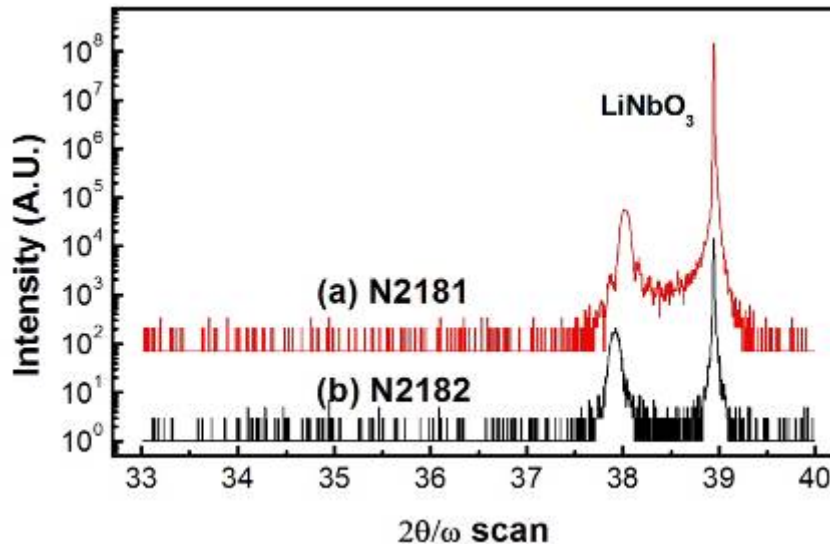
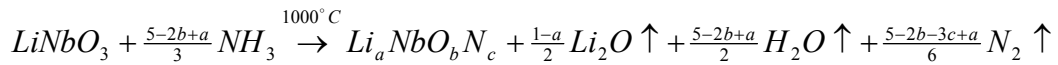


Figure 88: X-ray scan on $2\theta/\omega$ of (a) N2181 sample with FWHM of $31.86''$ at 38.94° $2\theta/\omega$ and FWHM of $346.35''$ at 38.02° (b) N2182 sample with FWHM of $31.71''$ at 38.94° and FWHM of $335.98''$ at 37.92° .

After nitridation on LN substrates for 30 minutes, GaN films with an ammonia source were grown on the LN substrate in the N2175 sample. The RHEED patterns of the GaN films show $2 \times$ spotty patterns indicating a rough surface with Ga-polar GaN films, as shown in Figure 90(a) and (b). After growing the GaN films, the surface morphologies of the GaN films on LN have a very rough surface in a Ga-rich growth condition as predicted with RHEED patterns as shown in Figure 90(c).

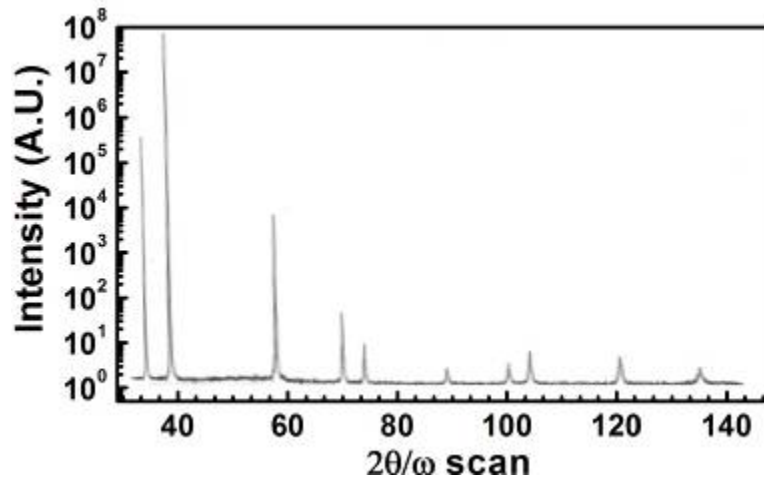


Figure 89: $\text{LiNbO}_3 + \text{NH}_3$ x-ray powder pattern of $\text{Li}_{1.92}\text{Nb}_{2.08}\text{O}_{1.21}\text{N}_{2.79}$ oxynitride composition [172].

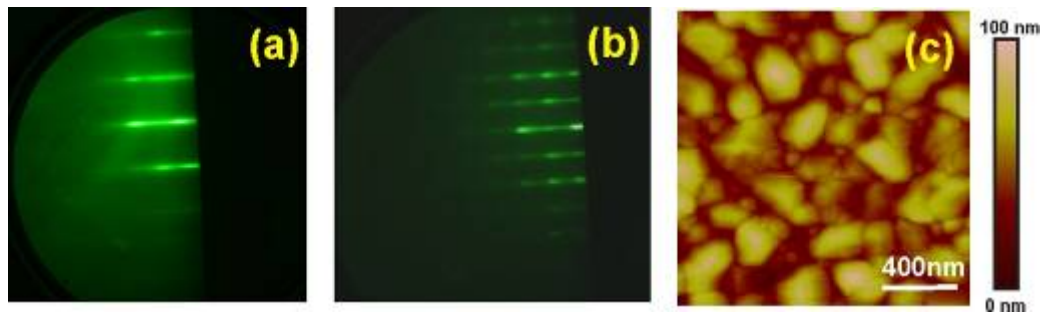


Figure 90: (a) during the nitridation on LN substrate at 700°C , (b) GaN growth after the nitridation on LN substrate at 700°C , and the surface morphology of the GaN films (c) in the area of $2\mu\text{m} \times 2\mu\text{m}$ with RMS roughness of 12nm of N2175 sample

After attempting to grow GaN films with an ammonia source on LN, the x-ray showed unknown peaks at 37.34620° and 39.2503° as shown in Figure 91. Based on the PCPDF x-ray database [173], the unknown peak (a) may be related to the mixture of lithium, gallium, and oxygen, which may make α -LiGaO₂ (lithium gallium oxide) with a peak at 37.344° on the (006) direction. The unknown peak (b) is estimated as a mixture of several possible compositions of α -NbN at 39.347° on (420), LiGa₅O₈ at 39.583° on (320), Li₅GaO₄ at 39.253° on (400), and/or Li₃GaN at 39.839° on (411).

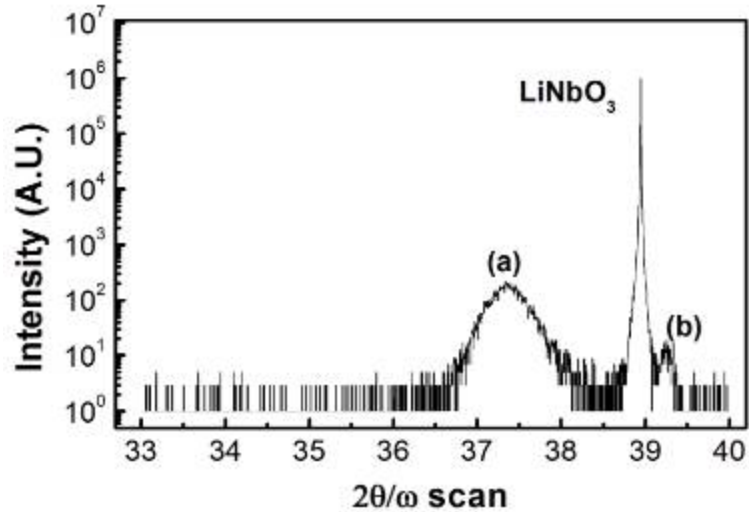


Figure 91: Epitaxial films with an ammonia source grown on the LN substrate in N2175 sample with unknown peaks at (a) 37.4620° and (b) 39.2503° on $2\theta/\omega$ scan.

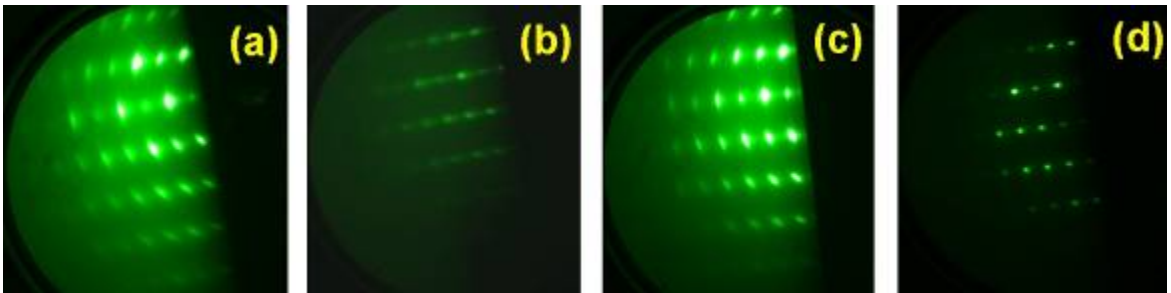


Figure 92: RHEED pattern images of (a) after nitridation at 700°C , AlN buffer growth at 700°C , (b) GaN growth at 700°C with 2 sccm ammonia in the sample of N2187, (c)

after nitridation at 800 °C, AlN buffer growth at 750 °C, (d) GaN films growth at 700 °C in the sample of N2183.

To investigate the effect of AlN buffer layers, the buffer layers were grown at 750 °C after nitridation at 700 °C and 800 °C for 30 minutes in N2187 and N2183, respectively. Then, GaN films were grown on the AlN buffer layers at 700 °C with a 2 sccm ammonia flow. Figure 92 shows the bright and spotty RHEED patterns of the AlN and GaN films, indicating a rough surface. Figure 93 shows the x-ray diffractions of the N2187 and N2183 samples. GaN films with AlN buffer layers have distinguishable GaN peaks compared to the case of N2175, which had no AlN buffer layers, indicating the advantage of using AlN buffer layers. However, the samples have the unknown peaks at 38.1246° with FWHM of 1500'' for N2187 and 37.7577° with FWHM of 1501'' for N2183. The unknown peaks could be a mixture of lithium, aluminum, oxygen, and nitrogen. The GaN films have the FWHM of 2480'' and 2376'' on (0002) ω scan for N2187 and N2183 samples, respectively.

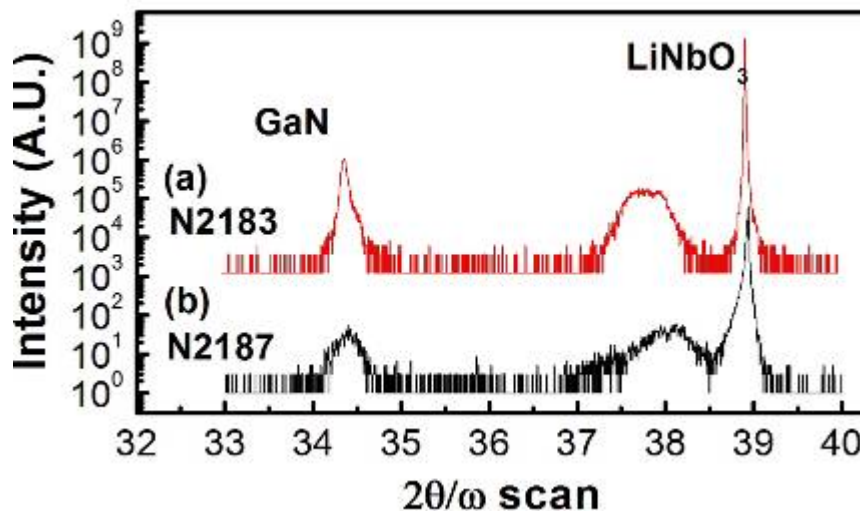


Figure 93: X-ray scan on $2\theta/\omega$ of (a) N2183 sample: GaN at 34.39° with FWHM of 205.4'' and an unknown peak at 37.75° with FWHM of 1500.7''; and (b) N2187 sample: GaN films at 34.36° with FWHM of 319.5'' and an unknown peak at 38.12° with FWHM of 1500''.

In summary, GaN films and AlN films were grown with ammonia as the source of reactive nitrogen. After 1 hour nitridation at 700 °C, the surface of the samples had porous shapes with average roughness of 1.74nm. It is concluded that high temperature nitridation is not an appropriate procedure for LN substrates. III-nitride growth with ammonia at high temperatures has unknown compositions, confirmed by x-ray diffraction. The unknown diffraction peaks are from the interaction of ammonia and LN substrates that produces bi-products, including cubic oxynitride phase ($\text{Li}_a\text{NbO}_b\text{N}_c$). However, after a shorter nitridation time (30 minutes), GaN on the LN substrates show a spotty $2\times$ RHEED patterns indicating a Ga-polar property with a rough surface. The growth has unknown compositions that may be related to the mixture of lithium, gallium, and oxygen, including $\alpha\text{-LiGaO}_2$, $\alpha\text{-NbN}$, LiGa_5O_8 , Li_5GaO_4 , and Li_3GaN . Finally, AlN buffer layers are helpful for making distinguishable GaN peaks in x-ray diffraction study but in general, ammonia based growth was less successful than nitrogen plasma based growth.

CHAPTER 9: HEMT FABRICATION

9.1 Fabrication of High Electron Mobility Transistor (HEMT)

The successful fabrication of AlGaN/GaN heterostructure devices on ferroelectric materials enables the development of multifunctional electrical and optical applications. A robust fabrication process for AlGaN/GaN HEMTs on LN (LT) would allow the monolithic integration of the III-nitride power devices with Ti-diffused optical waveguides. Importantly, stable, source/drain ohmic contact created with lower temperature anneals have been demonstrated, and methods to further decrease contact resistance have been identified [174].

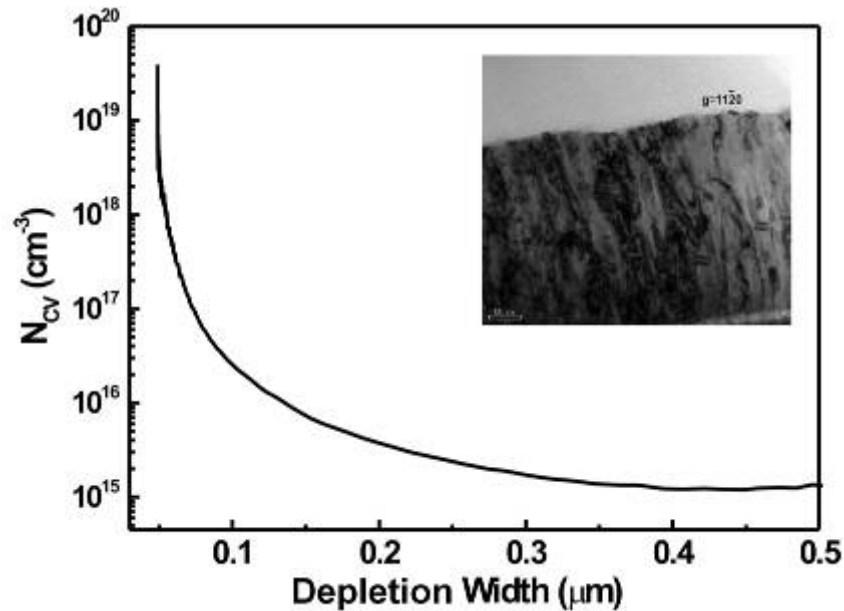


Figure 94: C-V measurement of AlGaN/GaN grown on LN. A TEM image in inset of figure indicates high dislocation density and rough surface of AlGaN/GaN, primarily the cause of the low mobility although some minimal residual bulk conductivity, comparable to other results [175] does exist in the C-V data.

Metals for the source/drain contact Ti (250 Å)/Al (1000 Å)/Ti (450 Å)/Au (1500 Å) were deposited using an e-beam evaporator. In the future work, Si(10 Å)/ Ti (250 Å)/Al (1000 Å)/Ti (450 Å)/Au (1500 Å) should be used to have a better contact. Using similar systems, low contact resistances are routinely achieved for n-GaN yielding a specific contact resistance are near 25 Ω -mm and 2.0×10^{-6} Ω -cm² [176]. However, reproducing this contact resistance for the AlGaN/GaN heterostructure on LN (LT) is difficult due to the significant thermal expansion coefficient mismatch of GaN films and LN (LT) substrates and strong pyroelectric effects in LN (LT). Indeed, rapid thermal annealing has proven to be impractical due to the common occurrence of LN (LT) substrate cracks and III-nitride layer peeling when using a rapid thermal anneal up to 800 °C. Therefore, a lower temperature 600 °C anneal was performed at a slow ramp rate of ~30 degrees per minute. Furthermore, the slow ramp rates and decreased temperatures have eliminated the problem of cracking LN substrates and peeling epitaxial layers. Clearly low resistance ohmic contacts are desired and vital to the successful performance of the monolithically integrated system.

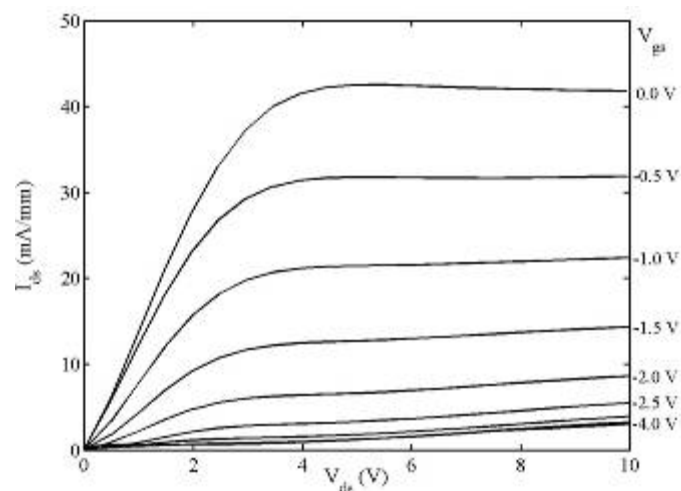


Figure 95: DC characterization of AlGaN/GaN HEMTs on the lithium niobate.

The typical DC current-voltage (I-V) device characteristics of AlGaIn/GaN heterostructures on LN substrates are presented in Figure 95 for a dual gate device with 200 μm gate width and 2.0 μm gate lengths. One may note that the device does not pinch off as expected from some residual conductivity in the substrate as measured in our C-V data (see Figure 94 for example). We have evaluated the performance of devices with gate widths ranging between 150 μm and 340 μm with a gate length of 1 μm as shown in Figure 96. The maximum drain current exceeds 350mA/mm and the maximum DC transconductance is ~ 25 mS/mm while it was measured ~ 7 mS/mm without ohmic contact anneals [3]. Although modest, this transconductance is larger than that achievable using the conventional high temperature ohmic-contact anneals. This improvement can be attributed to the 600 $^{\circ}\text{C}$ anneals. It had been observed that the breakdown voltage consistently exceeds 35 V, which is sufficient to drive the optical modulators.

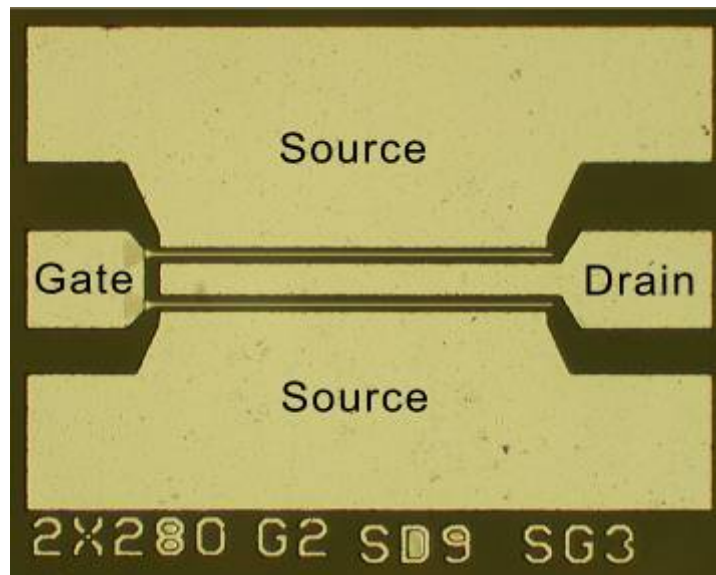


Figure 96: First generation of AlGaIn/GaN HEMTs on congruent LN with a gate length of 1 μm and width of 150 μm .

9.2 Fabrication steps and characterization of device properties

The fabrication sequence for III-Nitride HEMTS has already been demonstrated and functional HEMTs on LiNbO_3 have been characterized. The first process step was to deposit alignment marks (1500 Å of Al) using an E-beam evaporator, which was used to align the next mask sets. The second step was to make MESA isolation patterns using Cl_2/Ar plasma in an inductively-coupled-plasma reactive ion etch (ICP-RIE) system. Typically, AlGaIn/GaN HEMT had much lower rf power than expected from DC characteristics due to a significant frequency slump or collapse in drain current. This behavior was likely because high drain-gate fields accelerate electrons that tunnel from the gate into and along the surface states and into the dislocations. The tunneled electrons charged the surface and dislocations up acting as an effective elongated gate, resulting in reduced 2DEG density. A SiN_x passivation layer deposited by plasma-enhanced chemical vapor deposition (PECVD) has been effectively used to reduce the effects of the surface states and charging of dislocations [177,178]. Therefore, the third step was to deposit a SiN_x passivation layer need to be deposited on top of the AlGaIn layer. In the fourth step, source and drain definition regions were etched through the SiN_x to open up ohmic contact windows. The Ti (250 Å)/Al (1000 Å)/Ti (450 Å)/Au (1500 Å) metal contacts were deposited using an e-beam evaporator. In the future work, Si (10 Å)/ Ti (250 Å)/Al (1000 Å)/Ti (450 Å)/Au (1500 Å) should be used to have a better contact. Rapid thermal processing for 30 seconds at 600° C was performed to make the metal layers ohmic contacts. Schottky contacts on the gate were formed by depositing Ni (400 Å)/Au (2600 Å) metal layers by e-beam evaporator, followed by a liftoff process. Finally, contact pads

were deposited with Ti (500 Å)/Au (2000 Å) metal layers and finished by a liftoff process. All processes are illustrated in Figure 97.

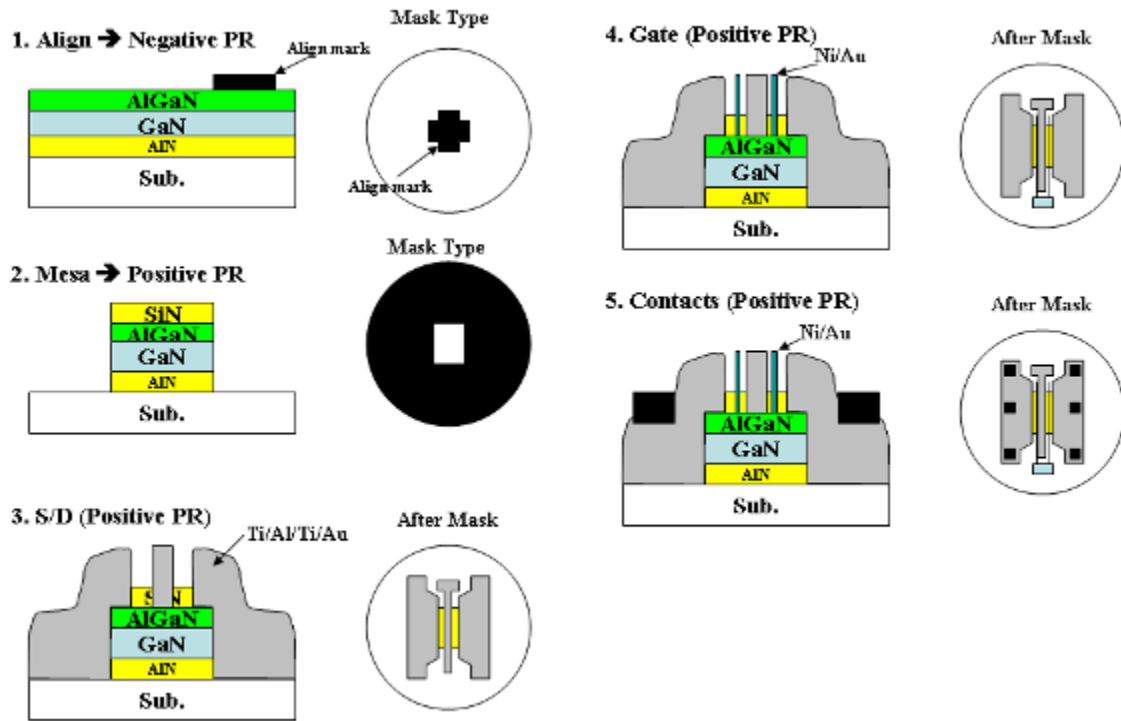


Figure 97: Overall process steps of state-of-art HEMT device fabrication with five masks and photo-resist types.

CHAPTER 10: CONCLUSION

This work investigated the material properties of lithium niobate (LN) as a new substrate to grow III-nitrides for high electron mobility transistor (HEMT) devices for use in mixed optoelectronic/electronic and acoustic applications. An earlier obstacle of developing III-nitrides grown on congruent lithium niobate (CLN) was very low yields of successfully grown III-nitrides because of the sample cracking resultant from the abnormally high thermal expansion and subsequent delamination of epilayers grown thicker than 0.5 μm . This work resolved the obstacle using a special sample holder and high-temperature substrate anneals. Even with a benefit of having an atomically flat surface, the high-temperature anneals developed repolarization domains on CLN, which induced inversion domains in subsequent III-nitrides. On the other hand, stoichiometric lithium niobate (SLN) and lithium tantalate (LT) provided better surface repolarization and stability during the high-temperature annealing but at the cost of less surface smoothing. Furthermore, the non-treated SLN and LT had better uniformity of polarity, resulted in better electron mobility on III-nitrides.

Another critical problem was chemical interactions at the film/substrate interface forming an alloy between III-nitrides and the substrates. This resulted in degradation of the crystal quality of subsequent III-nitrides. The degraded quality could be improved by a shutter modulation technique [104] but in this work, not improved enough for practical devices. Furthermore, impurities diffused both directions at the interface and made conductive III-nitrides which acted as current leakage paths in devices. So far, all our

attempts at HEMT devices have suffered from this current leakage path problem. Therefore, it is required to investigate the source current leakage path problem.

XRD, XPS, AES analysis confirmed that there was inter-diffusion between GaN films and LN when no buffer layers were presented. The inter-diffusion caused a deleterious effect on the resistivity of GaN films on LN. Future work should investigate the relationship between the inter-diffusion and the resistivity of GaN films. Thus, direct GaN film growth on ferroelectric materials is not recommended because of the inter-diffusion problem. To suppress the diffusion, non-conductive buffer layers need to be grown between the GaN films and ferroelectric materials.

Several buffer layers were investigated to resolve the diffusion problem. A low-temperature growth method provided high resistive GaN films, but poor crystal quality. GaN films on lithium alloyed aluminum buffer (LAAB) layers showed high resistive, but poor crystal quality as well. Lithium alloyed gallium buffer (LGAB) layers were not efficient in blocking the impurity diffusion. SiN_x and SiO_2 buffer layers caused amorphous GaN films because of large lattice mismatch. *n*-doped ZnO buffer layers made conductive GaN films. As a result, *p*-type or high-resistive ZnO (Li doped) films need to be investigated in the future. GaN films on Y_2O_3 -stabilized ZrO_2 (YSZ) buffer layers showed delamination problems. A high-temperature annealing method was introduced in LT substrates and proved somewhat effective in the improvement of the GaN resistivity. This method showed better surface morphology with AlN capping layers than with GaN capping layers.

Unfortunately, the suggested methods in this work couldn't perfectly resolve the last obstacle of the current leakage path problem. However, the suggested methods in this

work give future research directions. One of the directions will be the use of the low-temperature growth method with a shutter modulation technique after annealing AlN capping layers at high-temperatures. In this case, the shutter modulation would improve the poor crystal quality, which was from the low-temperature growth and/or AlN capping layers. Additionally, it is recommended to use lithium-doped ZnO buffer layers because they are highly resistive layers and would not likely leach out oxygen or lithium from the substrate. As another direction, instead of HEMT device, bipolar junction transistor (BJT) devices will be recommended because the device performance is independent on the current leakage paths. However, BJT needs to have *p*-type GaN films, which need high enough hole concentration to compensate the donor-like carriers. After successful development of the *p*-type GaN films, LEDs and photo-detectors will be the next generation of the integration.

In summary, in this work, we have demonstrated the growth by plasma-assisted MBE, fabrication and dc operation of AlGaIn/GaN HEMT electrical devices directly integrated on LN and LT. The characteristics of GaN on both LN and LT, such as crystalline orientation, structural quality, and polarity, are found to be very similar but slightly better for LT substrates. Although device characteristics are limited by several factors, including surface modification of LN, low hall mobility, inter-diffused alloy problems, and high ohmic contact resistance, we have demonstrated transistor devices on ferroelectric materials and show the DC device performance. Further developed material growth of III-nitrides on ferroelectric materials will allow the development of multi-functional electrical and optical applications in the future.

PUBLICATION LIST

Referred Journals

1. **K.-K. Lee**, Z. Cai, K. Ziemer, and W. A. Doolittle "The origin of the residual conductivity of GaN films on ferroelectric materials," to be submitted, 2009.
2. G. Namkoong, E. Trybus, **K.-K. Lee**, M. Moseley, D. C. Look, W. A. Doolittle "Metal modulation epitaxy growth for extremely high hole concentrations above 10^{19} cm⁻³ in GaN," Applied Physics Letter, Submitted, Aug. 2008.
3. **K.-K. Lee**, G. Namkoong, S. M. Madison, S. E. Ralph, W. A. Doolittle, M. Losurdo, G. Bruno, and H. K. Choi, "III-nitride growth and AlGaIn/GaN heterostructures on ferroelectric materials," Material Science Engineering B, vol. 140, pp.203, June 2007.
4. **K.-K. Lee**, G. Namkoong, W. A. Doolittle, M. Losurdo, G. Bruno, and D. Jundit, "III-nitride growth and characteristics on ferroelectric materials using plasma-assisted MBE," Journal of Vacuum Science Technology B, vol. 24, no. 4, pp. 2093, July 2006.
5. S. D. Burnham, G. Namkoong, **K.-K. Lee**, and W. A. Doolittle, "Reproducible RHEED signatures for improvement of AlN using *in situ* growth regime characterization," Journal of Vacuum Science and Technology B, vol. 25, no. 3, pp. 1009, May/June 2007.
6. G. Namkoong, **K.-K. Lee**, S. M. Madison, W. Henderson, S. E. Ralph, and W. A. Doolittle, "III-nitride integration on ferroelectric materials of lithium niobate by molecular beam epitaxy," Applied Physics Letter, vol. 87, no. 17, pp. 171107, Oct. 2005.
7. G. Namkoong, S. D. Burnham, **K.-K. Lee**, E. Trybus, W. A. Doolittle, M. Losurdo, P. Capezzuto, G. Bruno, B. Nemeth, and J. Nause, "III-nitrides on oxygen- and zinc-face ZnO substrates," Applied Physics Letter, vol. 87, pp. 184104-3, 2005.

Conference presentations

1. **K.-K. Lee**, G. Namkoong, W. A. Doolittle, M. Losurdo, G. Bruno, and H. K. Choi, "Interface Property Study of III-Nitrides on Lithium-Niobate to Improve the Device Performance of Optoelectronic-Acoustic-Electronic Applications" posted at 7th International Conference of Nitride Semiconductor, Las Vegas, NV, 2007.

2. **K.-K. Lee**, G. Namkoong, W. A. Doolittle, M. Losurdo, and G. Bruno, "III-nitride growth and characteristics on ferroelectric materials using plasma-assisted MBE, presented at 33rd Conference on the Physics and Chemistry of Semiconductor Interfaces, Cocoa Beach, FL, 2006.
3. S. D. Burnham, G. Namkoong, **K.-K. Lee**, and W. A. Doolittle, "Reproducible RHEED signatures for *in situ* growth regime characterization of AlN," presented at 24th North American Conference on Molecular Beam Epitaxy, Durham, NC, 2006.
4. D. Billingsley, D. Pritchett, W. Henderson, E. Trybus, **K.-K. Lee**, and W. A. Doolittle, "Influence of surface Nitridation on Gallium Nitride Growth via Ammonia Based Metal Organic Molecular Beam Epitaxy," posted at 24th North American Conference on Molecular Beam Epitaxy, Durham, NC, 2006.
5. E. Trybus, W. A. Doolittle, W. Henderson, G. Namkoong, S. D. Burnham, **K.-K. Lee**, I. Ferguson, and C. Honsberg, "InN: Revolutionary photovoltaic material or just a revolting material," presented at Workshop on Compound Semiconductor Materials and Devices, Miami, FL, 2005.
6. **Invited:** W. A. Doolittle, E. Trybus, W. Henderson, G. Namkoong, S. D. Burnham, **K.-K. Lee**, I. Ferguson, and C. Honsberg, "InN: A material with photovoltaic promise and challenges," AFOSR Indium Nitride Workshop 2, Kailua-Kona, Hawaii, Jan. 9-13, 2005.
7. **K.-K. Lee**, G. Namkoong, W. Henderson, and W. A. Doolittle, "III-nitrides on ferroelectric lithium niobate: Impact of the electrostatic boundary condition," presented at American Physical Society March Meeting, Los Angeles, CA, March. 21-25, 2005.
8. G. Namkoong, **K.-K. Lee**, S. M. Madison, S. E. Ralph, W. A. Doolittle, M. Losurdo, G. Bruno, and D. Jundit, "Crystalline stability of congruent and Li-rich lithium niobate for III-nitride optoelectronic-acoustic-electronic applications," presented at 23rd North American Conference on Molecular Beam Epitaxy, Santa Barbara, CA, Sept. 11th-14th, 2005.
9. S. M. Madison, **K.-K. Lee**, G. Namkoong, W. Henderson, S. E. Ralph, and W. A. Doolittle, "III-nitride-based high electron mobility transistor on lithium niobate," presented at Workshop on Compound Semiconductor Materials and Devices, Miami, FL, 2005.
10. **Invited:** W.A. Doolittle, A. Carver, W. Henderson, G. Namkoong, S. Madison, **K.-K. Lee**, and S.E. Ralph, "MBE of Complex Metal-Oxides: What is in the toolbox and how can we use these tools to construct devices?", April 11-14, 2005, Palm Springs, CA.

11. S. M. Madison, W. Henderson, G. Namkoong, **K.-K. Lee**, S. E. Ralph, and W. A. Doolittle, "Monolithic integration of electronic and electro-optical devices exploiting the AlGaIn/GaN-LiNbO₃ material system," presented at Conference on Lasers and Electro-Optics (CLEO), pt. 3, vol. 3. pp. 1605-7, 2005.
12. **K.-K. Lee**, G. Namkoong, S. M. Madison, W. Henderson, S. E. Ralph, and W. A. Doolittle, "Prospects for, problems with and practical implementation strategies for heteroepitaxy integrated electronics-optoelectronics utilizing the III-nitride /lithium niobate material system," presented at IEEE Lester Eastman Conference on High-Performance Devices, Troy, NY, Aug. 4-6, 2004.

REFERENCES

- [1] W. A. Doolittle, G. Namkoong, A. Carver, W. Henderson, and A. Brown, "III-Nitride Growth on Lithium Niobate: A new substrate material for Polarity Engineering in III-Nitride Heteroepitaxy," Proceedings of Materials Research Society Fall meeting, Boston MA, vol. 743, L1.4, Dec. 2002.
- [2] S. E. Ralph, M. King, G. Namkoong, W. A. Doolittle, "Monolithic integration of GaN electronic amplifiers with LiNbO₃ optical modulators," IEEE LEOS Annual Meeting Conference Proceedings, vol. 2, pp. 652, 2003.
- [3] S. M. Madison, W. Henderson, G. Namkoong, K. M. Patel, W. A. Doolittle, and S. E. Ralph, "Monolithic Integration of AlGaIn/GaN-LiNbO₃ Optical-Electronic Structures," IEEE Lasers and Electro-Optic Soc. (LEOS), vol. 1, pp. 232, 2004.
- [4] G. Namkoong, K.-K. Lee, S. M. Madison, W. Henderson, W. Alan Doolittle, and Stephen E. Ralph, "III-Nitride Integration on Ferroelectric Materials of Lithium Niobates by Molecular Beam Epitaxy," Applied Physics Letter, vol. 87, pp. 171107, 2005.
- [5] K.-K. Lee, G. Namkoong, S. M. Madison, S. E. Ralph, W. A. Doolittle, M. Losurdo, G. Bruno, H. K. Choi, "III-Nitrides growth and AlGaIn/GaN heterostructures on ferroelectric materials," Material Science Engineering B, vol. 140, pp.203, 2007.
- [6] G. Bu, D. Ciplys, M. S. Shur, G. Namkoong, W. A. Doolittle, and W. D. Hunt, "Leaky surface acoustic waves in Z-LiNbO₃ substrates with epitaxial AlN overlays," Applied Physics Letter, vol. 85, pp. 3313, 2004.
- [7] H. Tampo, H. Asahi, M. Hiroki, K. Asami, and S. Gonda, "Strong photoluminescence emission from GaN on SrTiO₃," Physica Status Solidi B, vol. 216, pp. 113, 1999.
- [8] K.-S. Kao, C.-C. Cheng, and Y.-C. Chen, "Synthesis and surface acoustic wave properties of AlN films deposited on LiNbO₃ substrates," IEEE Transactions on Ultrasonics, Ferroelectrics and Frequency Control, vol. 49, no. 3, pp. 345, 2002.
- [9] O. Ambacher, "Growth and applications of Group III-nitrides" Journal of Physics D: Applied Physics, vol. 31, pp. 2653, 1998.
- [10] O. Ambacher, J. Smart, J. R. Shealy, N. G. Weimann, K. Chu, M. Murphy, W. J. Schaff, and L. F. Eastman, R. Dimitrov, L. Wittmer, and M. Stutzmann, W. Rieger, and J. Hilsenbeck, "Two-dimensional electron gases induced by

- spontaneous and piezoelectric polarization charges in N- and Ga-face AlGa_N/Ga_N heterostructures,” *Journal of Applied Physics*, vol. 85, no. 6, pp. 3222, 1999.
- [11] B. Gelmont, K. Kim, and M. Shur, “Monte Carlo simulation of electron transport in gallium nitride,” *Journal of Applied Physics*, vol. 74, pp. 1818, 1993.
- [12] M. S. Shur, A. Kahn, B. Gelmont, R. J. Trew, and M. W. Shin, “Ga_N/AlGa_N Field Effect Transistors for High Temperature Applications,” *Proc. of the 21st International Symposium on Compound Semiconductors*, 419, 1995. (IOP Publishing, Bristol, UK; San Diego, CA, USA)
- [13] Q. Chen, J. W. Yang, M. A. Khan, A. Ping, and I. Adesida, “High transconductance AlGa_N/Ga_N heterostructure field effect transistors on SiC substrates,” *Electrons Letters*, vol. 33, pp. 1413, 1997.
- [14] M. Micovic, N. X. Nguyen, P. Janke, W.-S. Wong, P. Hashimoto, L.-M. McCray, and C. Nguyen, “Ga_N/AlGa_N high electron mobility transistors with fT of 110 GHz,” *Electronics Letters*, vol. 36, pp. 358, 2000.
- [15] N. X. Nguyen, M. Micovic, W.-S. Wong, P. Hashimoto, L.-M. McCray, P. Janke, and C. Nguyen, “High performance microwave power Ga_N/AlGa_N MODFETs grown by RF-assisted MBE,” *Electronics Letters*, 36, 468, 2000.
- [16] W. C. Johnson, J. B. Parsons, and M. C. Crew, “Nitrogen Compounds of Gallium. III,” *Journal of Physical Chemistry*, vol. 36, pp. 2651-2654, 1932.
- [17] S. Strite and H. Morkoc, “Ga_N, Al_N, and In_N: a review,” *Journal of Vacuum Science & Technology B (Microelectronics and Nanometer Structures)*, vol. 10, pp. 1237-1266, 1992.
- [18] H.P. Maruska and J. J. Tietjen, “The preparation and properties of vapour-deposited single- crystal-line Ga_N,” *Applied Physics Letter*, vol. 15, p. 327, 1969.
- [19] W. M. Yim, E. J. Stofko, P. J. Zanzucchi, J. I. Pankove, M. Ettenberg, and S. L. Gilbert, “Epitaxially grown Al_N and its optical band gap,” *Journal of applied Physics*, vol. 44, pp. 292, 1973.
- [20] S. Yoshida, S. Misawa, and S. Gonda, “Epitaxial growth of Ga_N/Al_N heterostructures,” *Journal of Vacuum Science Technology B*, vol. 1, pp. 250, 1983.
- [21] S. Strite, J. Ruan, Z. Li, N. Manning, A. Salvador, H. Chen, David J. Smith, W. J. Choyke, and H. Morkoc, “An investigation of the properties of cubic Ga_N grown on GaAs by plasma-assisted molecular-beam epitaxy,” *Journal of Vacuum Science Technology B*, vol. 9, pp. 1924, 1991.

- [22] M. Henini, "Molecular beam epitaxy: from research to manufacturing," *Thin Solid Films*, vol. 306 pp. 331, 1997.
- [23] M. A. Herman, and H. Sitter, *Molecular Beam Epitaxy, Springer Series in Materials Science* edited by M B Panish (New York: Springer), 1989.
- [24] B. T. Matthias and J. P. Remeika, "Ferroelectricity in the ilmenite structure," *Physics Review*, vol. 76, pp. 1886, 1949.
- [25] J. A. Giordmaine and R. C. Miller, "Tunable coherent parametric oscillation in LiNbO_3 at optical frequencies," *Physics Review Letter*, vol. 14, pp. 973, 1965.
- [26] S.C. Abrahams, P. Marsh, "Defect Structure Dependence on Composition in Lithium Niobate", *Acta Crystallographica B*, vol. 42, pp. 61, 1986.
- [27] A. M. Prokhorov and Yu. S. Kuz'minov, *Physics and chemistry of crystalline lithium niobate*, Adam Hilger/IOP Publishing Ltd., New York, 1990.
- [28] A. A. Ballman, "Growth of Piezoelectric and Ferroelectric Materials by the Czochralski Technique", *Journal of the American Ceramic Society*, vol. 48, no. 2, pp. 112, 1964.
- [29] <http://www.crystaltechnology.com>, Nov., 2008.
- [30] <http://www.redoptronics.com/litao3-crystals.html>, Nov., 2008.
- [31] D. Xue, S. Wu, R. Jayavel, K. Terabe, S. Kurimura, K. Kitamura, "Temperature dependant domain structures of lithium niobate single crystals," *IEEE International Symposium on Applications of Ferroelectrics*, vol. 37, 2002.
- [32] P. W. Haycock and P. D. Townsend, "A method of poling LiNbO_3 and LiTaO_3 below T_c " *Applied Physics Letter*, vol. 48, pp. 698, 1986.
- [33] D. Xue, K. Kitamura, "Compositional dependence of cationic displacements in lithium niobate and lithium tantalate crystals", *Journal of Physics and Chemistry of Solids*, vol. 66, pp. 585, 2005.
- [34] D. Xue, N. Iyi, and K. Kitamura, "Predicting temperature dependence of the refractive index and nonlinear optical coefficients in lithium niobate", *Journal of Applied Crystal*, vol. 92, pp. 4638, 2002.
- [35] A. A. Ballman, "Growth of Piezoelectric and Ferroelectric Materials by the Czochralski Technique", *Journal of the American Ceramic Society*, vol. 48, no. 2, pp. 112, 1964.

- [36] P. F. Bordui, R. G. Notwood, D. H. Jundt, and M. M. Fejer, "Preparation and characterization of off-congruent lithium niobate crystals," *Journal of Applied Physics*, vol. 71, no. 2, pp. 875, 1992.
- [37] J. R. Carruthers, G. E. Peterson, M. Grasso, and P. M. Bridenbaugh, "Nonstoichiometry and crystal growth of lithium niobate," *Journal of Applied Physics*, vol. 42, pp. 1846, 1971.
- [38] M. B. Roitberg, Z. I. Shapiro, and A. Z. Rabinovich, "Pyroelectric effect and spontaneous polarization in LiTaO_3 ," *Fizika Tverdogo Tela*, vol. 9, no. 12, pp. 3613, 1967.
- [39] H. J. Levinstein, A. A. Ballman, and C. D. Capio, "Domain Structure and Curie Temperature of Single-Crystal Lithium Tantalate," *Journal of Applied Physics*, vol. 37, no. 12, pp. 4585, 1966.
- [40] A. M. Glass, "Dielectric, thermal and pyroelectric properties of ferroelectric LiTaO_3 ," *Physical Review*, vol. 172, no. 2, pp. 564, 1968.
- [41] S. Miyazawa and H. Iwasaki, "Congruent Melting Composition of Lithium Metatantalate," *Journal of Crystal Growth*, vol. 10, pp. 276, 1971.
- [42] R. L. Barns, and J. R. Carruthers, "Lithium Tantalate Single Crystal Stoichiometry," *Journal of Applied Crystal*, vol. 3, pp. 395, 1970.
- [43] P. F. Bordui, F. G. Notwood, C. D. Bird, and J. T. Carella, "Stoichiometry issues in single-crystal lithium tantalate," *Journal of Applied Physics*, vol. 78, no. 7, pp. 4647, 1995.
- [44] S. C. Abrahams, S. K. Kurtz, P. B. Jamieson, "Atomic Displacement Relationship to Curie Temperature and Spontaneous Polarization in Displacive Ferroelectrics," *Physical Review*, vol. 172, pp. 551, 1968.
- [45] D. Xue, N. Iyi, and K. Kitamura, "Predicting temperature dependence of the refractive index and nonlinear optical coefficients in lithium niobate," *Journal of Applied Crystal*, vol. 92, pp. 4638, 2002.
- [46] J. Michael Golio, "Microwave MESFETs and HEMTs," Artech House, Inc. 1991
- [47] Chin, V.W.L, T.L. Tansley, T. Osotchan, "Electron mobilities in gallium, indium, and aluminum nitrides," *Journal of Applied Physics*, vol. 75, no. 11, pp. 7365, 1994.
- [48] C.-H. Ko, S.-J. Chang, Y.-K. SU, W.-H. Lan, J.F. Chen, T.-M. Kuan, Y.-C. Huang, C.-I. Chiang, J. Webb, and W.-J. Lin, "On the Carrier Concentration and Hall

- Mobility in GaN Epilayers,” Japanese Journal of Applied Physics, vol. 42, pp. L226, 2002.
- [49] J. Kolnik, I.H. Oguzman, K.F. Brennan, R. Wang, P.P. Ruden, and Y. Wang, “Electronic transport studies of bulk zinc-blende and wurtzite phases of GaN based on an ensemble Monte Carlo calculation including a full zone band structure,” Journal of Applied Physics, vol. 78, no. 2, pp. 1033, 1995.
- [50] R. Gaska, J.W. Yang, A. Osinsky, Q. Chen, M.A. Khan, A.O. Orlov, G.L. Snider, M.S. Shur, “Electron transport in AlGa_N-Ga_N heterostructures grown on 6H-SiC substrates,” Applied Physics Letter, vol. 72, no. 6, pp. 707, 1998.
- [51] K.K. Ng, “A Survey of Semiconductor,” IEEE Transactions of Electron Devices, vol. 43, no. 10, pp. 1760, 1996.
- [52] Rashmi, A. Kranti, S. Haldar, R.S. Gupta, “An accurate charge control model for spontaneous and piezoelectric polarization dependent two-dimensional electron gas sheet charge density of lattice-mismatched AlGa_N/Ga_N HEMTs,” Solid-State Electronics, vol. 46, pp. 621–630, 2002.
- [53] I. P. Smorchkova, C. R. Elsass, J. P. Ibbetson, R. Vetury, B. Heying, P. Fini, E. Haus, S. P. DenBaars, J. S. Speck, U. K. Mishra, “Polarization-induced charge and electron mobility in AlGa_N/Ga_N heterostructures grown by plasma-assisted molecular-beam epitaxy,” Journal of Applied Physics, vol. 86, no. 8, pp. 4520, 1999.
- [54] JMichael Golio, “Microwave MESFETs and HEMTs,” Artech House, Inc. 1991
- [55] S.M. Sze, *Semiconductor Devices: physics and technology 2nd Edition*, John Wiley & Sons, Inc., 2002.
- [56] R. Dingle, H. L. Stormer, A. C. Gossard, and W. Wiegmann, “Electron mobilities in modulation-doped semiconductor heterojunction superlattices,” Applied Physics Letter, vol. 33, no. 7, pp. 665, 1978.
- [57] J.P. Ibbetson, P.T. Fini, K.D. Ness, S.P. DenBaars, J.S. Speck, and U.K. Mishra, “Polarization effects, surface states, and the source of electrons in AlGa_N/Ga_N heterostructure field effect transistors,” Applied Physics Letters, vol. 77, no. 2, pp.250, 2000.
- [58] P. M. Asbeck, E. T. Yu, S. S. Lau, G. J. Sullivan, J. Van Hove, and J. M. Redwing, “Piezoelectric charge densities in AlGa_N/Ga_N HFETs,” Electronics Letters, vol. 33, pp. 1230, 1997.

- [59] A. Bhouiri, A. B. Fredj, J. L. Lazzari, M. Said, "Band offset calculations applied to III-V nitride quantum well device engineering," *Superlattices and Microstructures*, vol. 36, pp. 799, 2004.
- [60] F. Bernardini, V. Fiorentini and D. Vanderbilt, "Spontaneous polarization and piezoelectric constants of III-V nitrides," *Physics Review*, vol. B 56, pp. R10024, 1997.
- [61] Landolt-Bornstein: Numerical Data and Functional Relationships in Science and Technology, edited by O. Madelung Springer, New York, 1982.
- [62] A. Bykhovski, B. Gelmont, and M. Shur, "Influence of the strain-induced electric field on the charge distribution in GaN-AlN-GaN structure," *Journal of Applied Physics*, vol. 74, pp. 6734, 1993.
- [63] E. T. Yu, G. J. Sullivan, P. M. Asbeck, C. D. Wang, D. Qiao, and S. S. Lau, "Measurement of piezoelectrically induced charge in GaN/AlGaN heterostructure field-effect transistors," *Applied Physics Letter*, vol. 71, no. 19, pp. 2794, 1997.
- [64] S.J. Pearton, J.C. Zolper, R.J. Shul, and F. Ren, "Applied physics review: GaN: Processing, defects, and devices," *Journal of Applied Physics*, vol. 86, no. 1, pp. 1, 1999.
- [65] M. Shur, B. Gelmont, and M. A. Khan, "Electron mobility in two-dimensional electron gas in AlGaIn/GaN heterostructures and in bulk GaN," *Journal of Electron Material*, vol. 25, no. 5, pp. 777, 1996.
- [66] N. Weimann, L. F. Eastman, D. Doppalapudi, H. M. Ng, and T. D. Moustakas, "Scattering of electrons at threading dislocations in GaN," *Journal of Applied Physics*, vol. 83, pp. 3656, 1998.
- [67] Y. Zhang and J. Singh, "Charge control and mobility studies for an AlGaIn/GaN high electron mobility transistor," *Journal of Applied Physics*, vol. 85, no 1, pp. 587, 1999.
- [68] T. D. Moustakas, "Epitaxial growth of GaN films produced by ECR-assisted MBE," *Materials Research Society Symposium – Proceedings*, vol. 395, pp. 111, 1996.
- [69] Y. Tsuchiya, A. Kobayashi, J. Ohta, H. Fujioka, and M. Oshima, "GaN heteroepitaxial growth on LiNbO₃ (0001) step substrates with AlN buffer layers," *Physica Status Solidity A*, vol. 202, no. 13, pp. R145, 2005.
- [70] Y. Tsuchiya, A. Kobayashi, J. Ohta, H. Fujioka, M. Oshima, "Heteroepitaxial growth of GaN on atomically flat LiTaO₃ (0 0 0 1) using low-temperature AlN buffer layers," *Journal of Crystal Growth*, vol. 293, pp.22, 2006.

- [71] K.-K. Lee, G. Namkoong, W. Henderson, and W. A. Doolittle, "III-nitrides on ferroelectric lithium niobate: Impact of the electrostatic boundary condition," presented at American Physical Society March Meeting, Los Angeles, CA, March, 2005.
- [72] Gregory David Millar, *Periodically poled lithium niobate: Modeling, fabrication, and nonlinear-optical performance*, Doctoral Dissertation, Stanford University, 1998.
- [73] G.E. Jellison, C.O. Griffiths, D.E. Holcomb, "Electric-field-induced birefringence in LiNbO₃ measured by generalized transmission ellipsometry," *Applied Physics Letters* vol. 81, pp. 1222, 2002.
- [74] J.R. Herrington, B. Dischler, A. Rauber, J. Schneider, "An optical study of the stretching absorption band near 3 microns from OH- defects in LiNbO₃," *Solid State Communications*, vol. 12, pp.351, 1973.
- [75] R.M.A. Azzam, N.M. Bashara, *Ellipsometry and Polarized light*, north Holland, Amsterdam, 1977.
- [76] A. Y. Lushkin, V.B. Nazarenko, K.N. Piipchak, V.F. Shnyukov, A.G. Naumovets, "The impact of annealing and evaporation of LiNbO₃ crystals on their surface composition," *Journal of Physics D: Applied Physics*, vol. 32, pp. 9, 1999.
- [77] H. Jhans, J. M. Honing, C. N. R. Rao, "Optical properties of reduced LiNbO₃," *Journal of Physics C: Solid State physics*, vol. 19, pp. 3649, 1986.
- [78] T. Suzuki, "Oxygen partial pressure dependence of optical absorption in lithium niobate," *Journal of Crystal Growth*, vol. 163, pp. 403, 1996.
- [79] J.R. Carruthers, I.P. Kaminow, L.W. Stulz, "Diffusion kinetics and optical wave guiding properties of outdiffused layers in lithium niobate and lithium tantalate," *Applied Optics*, vol. 13, pp. 2333, 1974.
- [80] R. T. Smith and F. S. Welsh, "Temperature Dependence of the Elastic, Piezoelectric and Dielectric Constants of Lithium Tantalate and Lithium Niobate", *Journal of Applied Physics*, vol. 42, no. 6, pp. 2219, 1971.
- [81] Y. Zheng, E. Shi, S. Wang, Z. Lu, S. Cui, L. Wang, and W. Zhong, "Domain structures and etching morphologies of lithium niobate crystals with different Li contents grown by TSSG and double crucible Czochralski method," *Crystal Research and Technology*, vol. 39, pp. 387, 2004.

- [82] J. Webjorn, F. Laurell, and G. Arvidsson, "Blue light generated by frequency doubling of laser diode light in a lithium niobate channel waveguide," *IEEE Photonics Technology Letters*, vol. 1, no. 10, pp. 316, 1989.
- [83] K. Nakamura, H. Ando, and H. Shimizu, "Ferroelectric domain inversion caused in LiNbO₃ plates by heat treatment," *Applied Physics Letters*, vol. 50, pp. 1413, 1987.
- [84] H. Nagata, K. Shima, and J. Ichikawa, "Effect of hydroxyl content on thermally induced change in surface morphology of lithium niobate (0001⁻) substrates," *Journal of the American Ceramic Society*, vol. 80, pp. 1203, 1997.
- [85] M.E. Lines, A.M. Glass, *Principles and Applications of Ferroelectrics and Related Phenomena*, University Press, Oxford, 1978.
- [86] S. Kim, V. Gopalan, and A. Gruverman, "Coercive fields in ferroelectrics: A case study in lithium niobate and lithium tantalate," *Applied Physics Letters*, vol. 80, pp. 2740, 2002.
- [87] V. Y. Shur, E. L. Romyantsev, E. V. Nikolaeva, E. I. Shishkin, R. G. Batchko, M. M. Fejer, R. L. Byer, I. Mnushkina, "Domain kinetics in congruent and stoichiometric lithium niobate," *Ferroelectrics*, vol. 269, pp. 189, 2002.
- [88] C. C. Battle, S. Kim, V. Gopalan, K. Barkocy, M. C. Gupta, Q. X. Jia, and T. E. Mitchell, "Ferroelectric domain reversal in congruent LiTaO₃ crystals at elevated temperatures," *Applied Physics Letter*, vol. 76, pp. 2436, 2000.
- [89] M. Houe and P. D. Townsend, "Thermal polarization reversal of lithium niobate," *Applied Physics Letter*, vol. 66, no. 20, pp. 2667, 1995.
- [90] M. Yoshimoto, T. Maeda, T. Ohnishi, and H. Koinuma, "Atomic-scale formation of ultrasmooth surfaces on sapphire substrates for high-quality thin-film fabrication," *Applied Physics Letter*, vol. 67, no. 18, pp. 2613, 1995.
- [91] A. Saito, H. Matsumoto, S. Ohnisi, M. M. Akai-kasaya, Y. Kuwahara, and M. Aonom, "Structure of atomically smoothed LiNbO₃ (0001) surface," *Japanese Journal of Applied Physics*, vol. 43, pp. 2057, 2004.
- [92] M.H. Grabow and G.H. Gilmer, "Thin film growth modes, wetting and cluster nucleation," *Surface Science*, vol. 194, pp. 333, 1988.
- [93] S. E Ralph, M. King, G. Namkoong, W. A. Doolittle, "Monolithic integration of GaN electronic amplifiers with LiNbO₃ optical modulators," *IEEE LEOS Annual Meeting Conference Proceedings*, vol. 2, pp. 652, 2003.

- [94] S. M. Madison, W. Henderson, G. Namkoong, K. M. Patel, W. A. Doolittle, and S. E. Ralph, "Monolithic Integration of AlGaIn/GaN-LiNbO₃ Optical-Electronic Structures," *IEEE Lasers and Electro-Optic Soc. (LEOS)*, vol. 1, pp. 232, 2004.
- [95] G. Namkoong, K.-K. Lee, S. M. Madison, W. Henderson, W. Alan Doolittle, and Stephen E. Ralph, "III-Nitride Integration on Ferroelectric Materials of Lithium Niobates by Molecular Beam Epitaxy," *Applied Physics Letter*, vol. 87, pp. 171107, 2005.
- [96] G. Bu, D. Ciplys, M. S. Shur, G. Namkoong, W. A. Doolittle, and W. D. Hunt, "Leaky surface acoustic waves in Z-LiNbO₃ substrates with epitaxial AlN overlays," *Applied Physics Letter*, vol. 85, pp. 3313, 2004.
- [97] H. Tambo, H. Asahi, M. Hiroki, K. Asami, and S. Gonda, "Strong photoluminescence emission from GaN on SrTiO₃," *Physica Status Solidi B*, vol. 216, pp. 113, 1999.
- [98] K.-S. Kao, C.-C. Cheng, and Y.-C. Chen, "Synthesis and surface acoustic wave properties of AlN films deposited on LiNbO₃ substrates," *IEEE Transactions on Ultrasonics, Ferroelectrics and Frequency Control*, vol. 49, no. 3, pp. 345, 2002.
- [99] K.-K. Lee, G. Namkoong, W. A. Doolittle, M. Losurdo, G. Bruno, and D. Jundit, "III-nitride growth and characteristics on ferroelectric materials using plasma-assisted MBE," *Journal of Vacuum Science Technology B*, vol. 24, no. 4, pp. 2093, July 2006.
- [100] K.-K. Lee, G. Namkoong, S. M. Madison, S. E. Ralph, W. A. Doolittle, M. Losurdo, G. Bruno, H. K. Choi, "III-Nitrides growth and AlGaIn/GaN heterostructures on ferroelectric materials," *Material Science Engineering B*, vol. 140, pp.203, 2007.
- [101] K.-K. Lee, G. Namkoong, W. A. Doolittle, M. Losurdo, G. Bruno, and H. K. Choi, "Interface Property Study of III-Nitrides on Lithium-Niobate to Improve the Device Performance of Optoelectronic-Acoustic-Electronic Applications," posted at 7th International Conference of Nitride Semiconductor, Las Vegas, NV, 2007.
- [102] B. Heying, R. Averbeck, L. F. Chen and E. Haus, "Control of GaN surface morphologies using plasma assisted MBE," *Journal of Applied Physics*, vol. 88(4) pp. 1855, 2000.
- [103] S. D. Burnham, G. Namkoong, K.-K. Lee, and W. A. Doolittle, "Reproducible RHEED signatures for improvement of AlN using in situ growth regime characterization," *Journal of Vacuum Science and Technology B*, vol. 25, no. 3, pp. 1009, May/June 2007.

- [104] S. D. Burnham, G. Namkoong, D. C. Look, B. Clafin, and W. A. Doolittle, "Reproducible increased Mg incorporation and large hole concentration in GaN using metal modulated epitaxy," *Journal of Applied Physics*, vol. 104, pp. 024902, 2008.
- [105] K.-K. Lee, G. Namkoong, S. M. Madison, S. E. Ralph, and W. A. Doolittle (unpublished).
- [106] G. Namkoong, W. A. Doolittle, A. S. Brown, M. Losurdo, P. Capezzuto, and G. Bruno, "Role of sapphire nitridation temperature on GaN growth by plasma assisted molecular beam epitaxy: Part I. Impact of the nitridation chemistry on material characteristics," *Journal of Applied Physics*, vol. 91, pp. 2499, 2002.
- [107] T.L. Goodrich, J. Parisi, Z. Cai, and K.S. Ziemer, "Low temperature growth of crystalline magnesium oxide on hexagonal silicon carbide (0001) by molecular beam epitaxy," *Applied Physics Letters*, vol. 90, pp. 042910, 2007.
- [108] A. Sidorenko, H. Peisert, H. Neumann, and T. Chasse, "GaN nucleation on (0 0 0 1)-sapphire via ion-induced nitridation of gallium," *Applied Surface Science* vol. 252, pp. 7671, 2006.
- [109] R. Carin, J.P. Deville, J. Werckmann, "An XPS study of GaN thin films on GaAs," *Surface and Interface Analysis*, vol. 16, pp. 65, 1990.
- [110] S. D. Wolter, B. P. Luther, D. L. Waltemyer, C. Onneby, S. E. Mohneya, and R. J. Molnar, "X-ray photoelectron spectroscopy and x-ray diffraction study of the thermal oxide on gallium nitride," *Applied Physics Letters*, vol.70, pp. 2156, 1997.
- [111] N. Obinata, K. Sugimoto, K. Ijima, M. Ishibiki, S. Egawa, T. Honda, and H. Kawanishi, "Relationship between excess Ga and residual oxides in amorphous GaN films deposited by compound source molecular beam epitaxy," *Japanese Journal of Applied Physics*, vol. 44, no. 12, pp. 8432, 2005.
- [112] L.K. Li, L.S. Tan, and E.F. Chor, "Effects of surface plasma treatment on n-GaN ohmic contact formation," *Journal of Crystal Growth*, vol. 268 pp. 499 2004.
- [113] H.-D. Xiao, H.-L. Ma, Z.-J. Lin, J. Ma, F.-J. Zong, X.-J. Zhang, "Thermal stability of GaN powders in the flowing stream of N₂ gas," *Materials Chemistry and Physics*, vol. 106, pp. 5, 2007.
- [114] B.P.Gila, B.Luo, J.Kim, R.Mehandru, J.R.LaRoche, A.H.Onstine, E. Lambers, K. Siebein, C.R. Avernathy, F. Ren, S.J. Pearton, " The oxide/nitride interface: a study for gate dielectrics and field passivation," *Materials research society symposium proceedings*, vol.786, E8.5.1, 2004

- [115] National Institute of Standards and Technology (NIST) Standard Reference Database (<http://srdata.nist.gov/xps/>)
- [116] S.D. Wolter, J.M. DeLuca, S.E. Mohny, U. R.S. Kern, and C.P. Kuo, "An investigation into the early stages of oxide growth on gallium nitride," *Thin Solid Films*, vol. 371, pp. 153, 2000.
- [117] M.-Y. Kong, J.-P. Zhang, X.-L. Wang, and D.-Z. Sun, "Hydrogen behavior in GaN epilayers grown by NH₃-MBE," *Journal of Crystal Growth*, vol. 227-228, pp. 371, 2001.
- [118] J. Hedman and N. Martnsson, "Gallium nitride studied by electron spectroscopy," *Physica Scripta*, vol. 22, pp. 176, 1980.
- [119] T.S. Lay, Y.Y. Liao, W.H. Hung, M. Hong, J. Kwo, and J.P. Mannaerts, "Depth-profile study of the electronic structures at Ga₂O₃(Gd₂O₃) and Gd₂O₃-GaN interfaces by X-ray photoelectron spectroscopy," *Journal of Crystal Growth*, vol. 278, pp. 624, 2005.
- [120] A. M. Prokhorov and Yu. S. Kuz'minov, *Physics and chemistry of crystalline lithium niobate*, Adam Hilger/IOP Publishing Ltd., New York, 1990.
- [121] H. Amano, N. Sawaki, I. Akasaki, Y. Toyota, "Metalorganic vapor phase epitaxial growth of a high quality GaN film using an AlN buffer layer," *Applied Physics Letters*, vol. 48, pp. 353, 1986.
- [122] I. Akasaki, H. Amano, Y. Koide, K. Hiramatsu, and, N. Sawaki, "Effects of AlN buffer layer on crystallographic structure and on electrical and optical properties of GaN and Ga_{1-x}Al_xN (0 < x < 0.4) films grown on sapphire substrate by MOVPE," *Journal of Crystal Growth*, vol. 98, pp. 209, 1989.
- [123] E. J. Tarsa, B. Heying, X. H. Wu, P. Fini, S. P. DenBaars, and J. S. Speck, "Homoepitaxial growth of GaN under Ga-stable and N-stable conditions by plasma-assisted molecular beam epitaxy," *Journal of Applied Physics*, vol. 82, pp. 5472, 1997.
- [124] E. S. Hellman, "The polarity of GaN: A critical review," *MRS Internet Journal of Nitride Semiconductor Research*, vol. 3, pp. 11, 1998.
- [125] M. Murphy, K. Chu, H. Wu, W. Yeo, W. J. Schaff, O. Ambacher, J. Smart, J. R. Shealy, L. F. Eastman, and T. J. Eustis, "Molecular beam epitaxial growth of normal and inverted two-dimensional electron gases in AlGa_N/GaN based heterostructures," *Journal of Vacuum Science and Technology B*, vol. 17, pp. 1252, 1999.

- [126] R. Gaska, J. W. Yang, A. Osinsky, Q. Chen, M. Khan, A. Orlov, G. Snider, and M. S. Shur, "Electron transport in AlGa_N-Ga_N heterostructures grown on 6H-SiC substrates," *Applied Physics Letters*, vol. 72, pp. 707, 1998.
- [127] G. Namkoong, W.A. Doolittle, A. S. Brown, M. Losurdo, M. M. Giangregorio, G. Bruno, "Effect of buffer design on AlGa_N/AlN/GaN heterostructures by MBE," *Materials Research Society Symposium Proceedings*, vol.798, pp. 359-64, 2004.
- [128] Z. Y. Fan, J. Li, J. Y. Lin, and H. X. Jiang, "Delta-doped AlGa_N/Ga_N metal-oxide-semiconductor heterostructure field-effect transistors with high breakdown voltages," *Applied Physics Letters*, vol. 81, pp. 4649, 2001.
- [129] G. Namkoong, W. A. Doolittle, A. S. Brown, M. Losurdo, P. Capezzuto, and G. Bruno, "The impact of substrate nitridation temperature and buffer design and synthesis on the polarity of Ga_N epitaxial films," *Journal of Crystal Growth*, vol. 252, pp. 159, 2003.
- [130] A. R. Smith, R. M. Feenstra, D. W. Greve, M.-S. Shin, M. Skowronski, J. Neugebauer, and J. E. Northrup, "Determination of wurtzite Ga_N lattice polarity based on surface reconstruction," *Applied Physics Letters*, vol. 72, pp.2114, 1998
- [131] S. D. Burnham, G. Namkoong, K.-K. Lee, and W. A. Doolittle, "Reproducible RHEED signatures for improvement of AlN using in situ growth regime characterization," *Journal of Vacuum Science and Technology B*, vol. 25, no. 3, pp. 1009, 2007.
- [132] L.O. Svaasand, M. Eriksrud, G. Nakken and A.P. Grande, "Solid-solution range of LiNbO₃," *Journal of Crystal Growth*, vol. 22, pp. 230, 1974.
- [133] G. Namkoong, W. A. Doolittle, A. S. Brown, M. Losurdo, P. Capezzuto, and G. Bruno, "Role of sapphire nitridation temperature on Ga_N growth by plasma assisted molecular beam epitaxy: Part I. Impact of the nitridation chemistry on material characteristics," *Journal of Applied Physics*, vol. 91, pp. 2499, 2002.
- [134] G. Namkoong, S. Burnham, K.-K. Lee, E. Trybus, W. A. Doolittle, M. Losurdo, P. Capezzuto, G. Bruno, B. Nemeth, and J. Nause, "III-nitrides on oxygen- and zinc-face ZnO substrates," *Applied Physics Letters*, vol. 87, pp.184104, 2005.
- [135] A. V. Kuznetsov, E. V. Rakova, S. S. Lee, P. J. Chong, "Influence of moisture and oxygen on the formation of cubic phase Ga_N in halide vapor phase epitaxial growth," *Journal of Crystal Growth*, vol. 167, pp. 458, 1996.
- [136] T. Onitsuka, T. Maruyama, K. Akimoto, Y. Bando, "Interface structure of Ga_N on sapphire (0001) studied by transmission electron microscope," *Journal of Crystal Growth*, vol. 189-190, pp. 295, 1998.

- [137] C.-Y. Yeh, Z.W. Lu, S. Froyen, A. Zunger, "Zinc-blend-wurtzite polytypism in semiconductors," *Physical Review B (Condensed Matter)*, vol. 46, pp. 10087, 1992.
- [138] H. K. Cho and J. Y. Lee, K.S. Kim, G. M. Yang, J. H. Song and P. W. Yu, "Effect of buffer layers and stacking faults on the reduction of threading dislocation density in GaN overlayers grown by metalorganic chemical vapor deposition," *Journal of Applied Physics*, vol. 89, pp. 2617, 2001.
- [139] X. Xu, T-C. Chong, S. Solanki, X. Liang, S. Yuan, "Anisotropic thermal expansion of stoichiometric lithium niobate crystals grown along the normal direction of facets," *Optical Materials*, vol. 26, pp. 489, 2004.
- [140] M. Leszczynski, T. Suski, H. Teisseyre, P. Perlin, I. Grzegory, J. Jun, S. Porowski and T. D. Moustakas, "Thermal expansion of gallium nitride," *Journal of Applied Physics*, vol. 76, pp. 4909, 1994.
- [141] M. J. Manfra, N. G. Weimann, J. W. P. Hsu, L. N. Pfeiffer, and K. W. West, and S. N. G. Chu, "Dislocation and morphology control during molecular-beam epitaxy of AlGaIn/GaN heterostructures directly on sapphire substrates," *Applied Physics Letters*, vol. 81, pp. 1456, 2002.
- [142] J. Burm, W. Schaff, L. Eastman, H. Amano, and I. Akasaki, "75 Å GaN channel modulation doped field effect transistors," *Applied Physics Letters*, vol. 68, pp. 2849, 1996.
- [143] S. Heikman, S. Keller, T. Mates, S. P. Den Baars, and U.K. Mishra, "Growth and characteristics of Fe-doped GaN," *Journal of Crystal Growth*, vol. 248, pp. 513, 2003.
- [144] A.P. Grzegorzczuk, L. Macht, P.R. Hageman, M. Rudzinski, and P.K. Larsen, "Resistivity control of unintentionally doped GaN films," *Physica Status Solidi C*, vol. 2, no. 7, pp. 2113, 2005.
- [145] A.E. Wickenden, D.D. Koleske, R.L. Henry, M.E. Twigg, and M. Fatemi, "Resistivity control in unintentionally doped GaN films grown by MOCVD," *Journal of Crystal Growth*, vol. 260, pp. 54, 2004.
- [146] E. G. Brazel, M. A. Chin, and V. Narayanamurti, "Direct observation of localized high current densities in GaN films," *Applied Physics Letter*, vol. 74, no. 16, pp. 2367, 1999
- [147] T. Tanaka, Y. Koji, T. Meguro, and Y. Otoki, "Improvement of Substrate Related Uniformity of AlGaIn/GaN HEMP Epi Wafers on $\phi 3$," *Sapphire and SiC*

Substrates Grown by Multi-charged Large MOVPE Reactor,” The International Conference on Compound Semiconductor Manufacturing Technology, 11B-3, 2004.

- [148] X. L. Sun, S. T. Bradley, and G. H. Jessen, D. C. Look, R. J. Molnar, and L. J. Brillson, “Micro-Auger electron spectroscopy studies of chemical and electronic effects at GaN-sapphire interfaces,” *Journal of Vacuum Science and Technology*, vol. A 22, no. 6, pp. 2284, 2004.
- [149] A. Kobayashi, “Polarity control of GaN grown on ZnO,” *Applied Physics Letter*, vol. 88, pp. 181907, 2006.
- [150] L. G. Parratt, " surface studies of solids by total reflection of X-rays," *Physical Review*, vol. 95, pp. 359, 1954.
- [151] de Boer D K G, “Glancing-incidence x-ray fluorescence of layered materials,” *Physical Review B*, vol. 44, pp. 498, 1991.
- [152] A. J. G. Leenaers, D. K. G. de Boer, *WinGIXA manual*, Philips Analytical X-Ray B. V., Almelo, the Netherlands.
- [153] S. Seo, K. K. Lee, S. Kang, S. Huang, W.A. Doolittle, N. M. Jokerst, A. S. Brown, and M. A. Brooke, “The heterogenous integration of GaN thin-film metal–semiconductor– metal photodetectors onto silicon,” *IEEE photonics technology letters*, vol. 14, no. 2, pp. 185, 2002.
- [154] J. H. Hines, D. C. Malocha, K. B. Sundaram, K. J. Casey, and K. R. Lee, “Deposition parameter studies and surface acoustic wave characterization of PECVD silicon nitride films on lithium niobate,” *IEEE Transactions on ultrasonics, ferroelectrics, and frequency control*, vol. 42, no. 3, pp.397, 1995.
- [155] J. Huang, Z. Ye, L. Wang, J. Yuan, B. Zhao, and H. Lu, “Comparison of GaN epitaxial films on silicon nitride buffer and Si(111),” *Solid-State Electronics*, vol. 46, pp. 1231, 2002.
- [156] A. Sagar, R. M. Feenstra, C. K. Inoki, T. S. Kuan, Y. Fu, Y. T. Moon, F. Yun, and H. Morkoç, “Dislocation density reduction in GaN using porous SiN interlayers,” *Physica Status Solidi A*, 202, no. 5, pp. 722, 2005.
- [157] H. Nagata, M. Shiroishi, T. Kitanobou, and K. Ogura, “DC drift reduction in LiNbO₃ optical modulators by decreasing the water content of vacuum evaporation deposited SiO₂ buffer layers,” *Optical Engineering*, vol. 37, no. 10, pp. 2855, 1998.

- [158] V.Bhatt and S.Chandra, "Silicon dioxide films by RF sputtering for microelectronic and MEMS applications," *Journal of micromechanics and micro-engineering*, vol. 17, pp. 1066, 2007.
- [159] H.-B. Kang, K. Yoshida, and K. Nakamura, "Growth of ZnO thin films on LiNbO₃ substrates by electron cyclotron resonance-assisted Molecular Beam Epitaxy," *Japanese Journal of Applied Physics*, vol. 37, pp. 5220, 1998.
- [160] J.-R. Duclèrea, M. Novotny, A. Meaney, R. O'Haire, E. McGlynn, M.O. Henry, J.-P.Mosnier, "Properties of Li-, P- and N-doped ZnO thin films prepared by pulsed laser deposition," *Superlattices and Microstructures*, vol. 38, pp. 397, 2005.
- [161] K. Matsubara, P. Fons, A. Yamada, M.Watanabe, and S. Niki, "Epitaxial growth of ZnO thin films on LiNbO₃ substrates," *Thin Solid Films*, vol. 347, pp. 238, 1999.
- [162] A. Kobayashi, S. Kawano, Y. Kawaguchi, J. Ohta, and H. Fujioka, "Room temperature epitaxial growth of m-plane GaN on lattice-matched ZnO substrates," *Applied Physics Letters*, vol. 90, pp. 041908, 2007.
- [163] K. Imada, K. Yoshiara, I. Kawamata, F. Uchikawa, S. Utsunomiya, T. Mizuochi, T. Kilayama, and Y Isoda, "YBCO superconducting films on LiNbO₃ with buffer layers for optical modulators," *Superconductor Science and Technology*, vol. 4, pp. 473, 1991.
- [164] R-H Kima, H-H Park, and G-T Joo, "The growth of LiNbO₃ (0 0 6) on MgO (0 0 1) and LiTaO₃ (0 1 2) substrates by sol-gel procedure," *Applied Surface Science*, 160, pp.564, 2001.
- [165] S. Hashiguchi, E. Min, K. Skuta, and T. Kobayashi, "YBaCuO thin-film growth on electrooptic LiNbO₃ substrate with buffer layer," *Japanese Journal of Applied Physics*, vol. 31, pp. 780, 1992.
- [166] D. Caceres, I. Colera, I. Vergara, R. Gonzalez, E. Roman, "Characterization of MgO thin films grown by rf-sputtering," *Vacuum*, vol. 67, pp. 577, 2002.
- [167] J.-J. Chen, B. P. Gila, M. Hlad, A. Gerger, F. Ren, C. R. Abernathy and S. J. Pearton "Determination of MgO/GaN heterojunction band offsets by x-ray photoelectron spectroscopy," *Applied Physics Letters*, 88, pp. 042113, 2006.
- [168] L. Fabrega, R. Rubi, J. Fontcuberta, F. Sanchez, C. Ferrater, M. V. Garcia-Cuenca, M. Varela, C. Collado, J. Mateu, O. Menendez, and J. M. O'Callaghan, "Reduced microwave losses of YBa₂Cu₃O_{7-δ} thin films on electro-optic LiNbO₃ crystals," *Journal of Applied Physics*, vol. 92, no. 10, pp. 6346, 2002.

- [169] R. Paszkiewicz, B. paszkiewicz, R. Korbutowicz, J. Kozlowskj, M. Tlaczala, L. Bryja, R. Kudrawiec, and J. Misiewicz, "MOVPE GaN Grown on Alternative Substrates," *Crystal Research Technology*, vol. 36, pp. 971, 2001.
- [170] S.Y. Karpov, R.A. Talalaev, Y.N. Makarov, N. Grandjean, J. Massies, and B. Damilano, "Growth kinetics of GaN in ammonia atmosphere," *Physica Status Solidi A*, 176, pp. 333, 1999.
- [171] HSC Chemistry software, <http://www.outotec.com>, Nov., 2008.
- [172] R. Assabaa-boultif, R. Marchand, and Y. Laurent, "Mixed-valence vanadium, niobium and tantalum in new series of NaCl-type lithium/VB element oxynitrides," *European Journal of Solid State and Inorganic Chemistry*, vol. 32, no. 11, pp. 1101, 1995.
- [173] PCPDF x-ray database 72-2112.
- [174] A. T. Ping, Q. Chen, J. W. Yang, M. Asif Khan, and I. Adesida, "The effects of reactive ion etching-induced damage on the characteristics of ohmic contacts to n-type GaN," *Journal of Electronic Materials*, vol. 27, pp. 261, 1998.
- [175] K. M. Jones, P. Visconti, F. Yun, A. A. Baski, and H. Morkoc, "Characterization of free-standing hydride vapor phase epitaxy GaN," *Applied Physics Letters*, vol. 78, pp. 2497, 2001.
- [176] V. Kumar and I. Adesida, "AlGaIn/GaN HEMTs on sapphire," *Proceedings of the Fourth IEEE International Caracas Conference on Devices, Circuits and Systems (Cat. No. 02TH8611)*, pp. D048-1, 2002.
- [177] B. M. Green, K. K. Chu, E. M. Chumbes, J. A. Smart, J. R. Shealy, and L. F. Eastman, "The effect of surface passivation on the microwave characteristics of undoped AlGaIn/GaN HEMTs," *IEEE Electron Device Letters*, vol. 21, pp. 268, 2000.
- [178] L. F. Eastman, V. Tilak, J. Smart, B. M. Green, E. M. Chumbes, R. Dimitrov, H. Kim, O. S. Ambacher, N. Weimann, T. Prunty, M. Murphy, W. J. Schaff, and J. R. Shealy, "Undoped AlGaIn/GaN HEMTs for microwave power amplification," *IEEE Transactions on Electron Devices*, vol. 48, pp.479, 2001.